



**UNIVERSIDADE FEDERAL DE MINAS GERAIS**

**PROGRAMA DE PÓS-GRADUAÇÃO EM  
ENGENHARIA MECÂNICA**

**EXPERIMENTAL STUDY OF A CO<sub>2</sub> DIRECT-EXPANSION  
SOLAR-ASSISTED HEAT PUMP OPERATING WITH AN  
ADIABATIC COILED CAPILLARY TUBE**

**THIAGO TORRES MARTINS ROCHA**

**Belo Horizonte, March 13<sup>th</sup>, 2020**

Thiago Torres Martins Rocha

**EXPERIMENTAL STUDY OF A CO<sub>2</sub> DIRECT-EXPANSION  
SOLAR-ASSISTED HEAT PUMP OPERATING WITH AN  
ADIABATIC COILED CAPILLARY TUBE**

Final Version

Dissertation submitted to the Graduated Program in Mechanical Engineering of Federal University of Minas Gerais, as a partial requirement for obtaining the Master degree in Mechanical Engineering.

Concentration area: Energy and Sustainability

Advisor: Prof. Raphael Nunes de Oliveira

Co-advisor: Prof. Tiago de Freitas Paulino

Belo Horizonte

Engineering School of UFMG

2020

R672e

Rocha, Thiago Torres Martins.

Experimental study of a CO<sub>2</sub> direct-expansion solar-assisted heat pump operating with an adiabatic coiled capillary tube [recurso eletrônico] / Thiago Torres Martins Rocha. - 2020.

1 recurso online (104 f. : il., color.) : pdf.

Orientador: Raphael Nunes de Oliveira.

Coorientador: Tiago de Freitas Paulino.

Dissertação (mestrado) - Universidade Federal de Minas Gerais, Escola de Engenharia.

Apêndices: f.97-104.

Bibliografia: f. 88-96.

Exigências do sistema: Adobe Acrobat Reader.

1. Engenharia mecânica - Teses. 2. Bombas de calor - Teses.  
3. Controle de custo - Teses. I. Oliveira, Raphael Nunes de. II. Paulino, Tiago de Freitas. III. Universidade Federal de Minas Gerais. Escola de Engenharia. IV. Título.

CDU: 621 (043)



**UNIVERSIDADE FEDERAL DE MINAS GERAIS**  
**PROGRAMA DE PÓS-GRADUAÇÃO EM**  
**ENGENHARIA MECÂNICA**

Av. Antônio Carlos, 6627 - Campus Universitário

31270-901 - Belo Horizonte - MG

Tel.: +55 31 3409.5145

E-mail: [cpgmec@demec.ufmg.br](mailto:cpgmec@demec.ufmg.br)

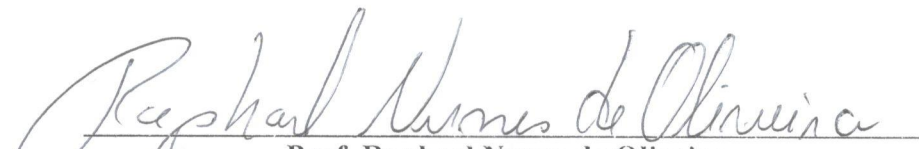
**"EXPERIMENTAL STUDY OF A CO<sub>2</sub> DIRECT-EXPANSION SOLAR-  
ASSISTED HEAT PUMP OPERATING WITH AN ADIABATIC  
COILED CAPILLARY TUBE"**


**THIAGO TORRES MARTINS ROCHA**

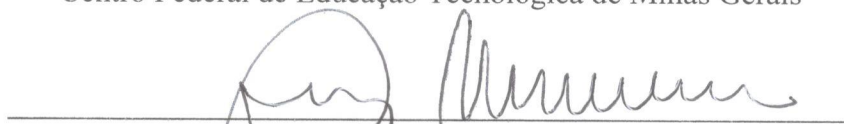
Dissertação submetida à Banca Examinadora designada pelo Colegiado do Programa de Pós-Graduação em Engenharia Mecânica da Universidade Federal de Minas Gerais, como parte dos requisitos necessários à obtenção do título de "**Mestre em Engenharia Mecânica**", na área de concentração de "**Energia e Sustentabilidade**".

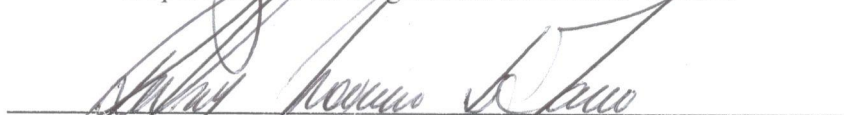
Dissertação aprovada no dia 13 de março de 2020.

Por:

  
**Prof. Raphael Nunes de Oliveira**  
Orientador - Departamento de Engenharia Mecânica/ UFMG

  
**Prof. Tiago de Freitas Paulino**  
Centro Federal de Educação Tecnológica de Minas Gerais

  
**Prof. Luiz Machado**  
Departamento de Engenharia Mecânica/ UFMG

  
**Prof. Ralney Nogueira de Faria**  
Centro Federal de Educação Tecnológica de Minas Gerais

**Prof. Juan José Garcia Pabón**  
Universidade Federal de Itajubá/ UNIFEI

## ACKNOWLEDGMENTS

Firstly, I thank to God for his constant presence in my life, and for one more achievement granted by Him.

To my parents, who always encouraged and supported me through this journey. To my wife, for his understanding, partnership, and for taking care of our needs during this period. To my daughter, for being a blessing and a motivation in my life. To my sister and all my relatives and friends for their love to me.

To my friend and professor Fernando Antônio Rodrigues Filho, for encouraging me to apply in the Masters admission process and to start an academic path. To my advisor, Raphael Nunes de Oliveira, and my co-advisor, Tiago de Freitas Paulino, who assumed this work as their work, always assisting me.

To my colleagues from GREA who always helped me to solve the difficulties, specially to put the workbench in operation. To the professors Pedro Bastos Costa, Alexandre Mendes Abrão, and to the colleagues Vinicius Melo Cangussu, and Diogo Azevedo de Oliveira, who offered their laboratories, expertise and time to help me with the preparation of samples, extremely necessary to my work. To LCPNano-UFGM and to Rafael Silva Gonçalves for welcoming me with open doors to use their facilities. To professor Luiz Machado, who provided the resources to adapt the workbench.

To Mr. Edson, from control and automation Laboratory, to Marina, Secretary of the Postgraduate Program in Mechanical Engineering, and to all who have contributed with this work, my heartfelt thanks.

## ABSTRACT

Heat pumps are equipment used to promote space heating, to supply hot water or used for other heating purposes. The number of these systems should raise 16 times by 2050, as a contribution to meet the Paris agreement objectives. Despite presenting a relatively high efficiency, e.g. compared to electric resistance heaters, heat pumps still need to be developed. Direct-expansion solar-assisted heat pumps (DX-SAHP) are one alternative to improve the performance of air source heat pumps (ASHP). In this work, the behavior of a CO<sub>2</sub> DX-SAHP is investigated under different operational conditions. However, the adjustable area expansion device (e.g. electronic expansion valve – EEV), generally used, was replaced by a capillary tube as an alternative to reduce the manufacturing costs. Initially, an algebraic solution to design an adiabatic coiled capillary tube operating in transcritical CO<sub>2</sub> cycle was developed. Three different friction factors and three different k factors, related to the specific volume, were analyzed, creating a total of 9 possible combinations. After designing and assembling the tubes onto the workbench, tests were performed following a factorial design, with 2 different capillary tubes and 3 different operating conditions, namely: high solar radiation (HSR), low solar radiation (LSR), and low solar radiation with fan (LSR+fan). The results indicated an average augment of 57.9% on the heating capacity, 42.3% on COP, and 35% on the refrigerant mass flow rate, when changing from LSR (6 W/m<sup>2</sup>) to HSR (969 W/m<sup>2</sup>). The superheat degree went from 4.4 to 30.6°C and the evaporating pressure changed from 40.0 to 51.2 bar. However, the gas cooler pressure also showed a significant increase, from 83.5 to 87.9 bar. To limit the raise of the superheat degree and to keep the compressor integrity, minor modifications are recommended. Altering from LSR to LSR+fan, an improvement of 17.2% on heating capacity was found, with no penalty to COP, showing that the addition of the fan is advantageous in low solar radiation conditions. Apart from the factorial design, additional runs were carried out to increase the number of experimental points to validate the capillary tube algebraic solution. Overall, the C-M&N friction factor demonstrated to be the best for the proposed solution. The percentual of mass flow rate points predicted within 10% and 15% error bands were 95% and 100%, respectively, for the best combination.

Keywords: Heat pump. Cost reduction. Capillary tube. CO<sub>2</sub>. DX-SAHP. Algebraic solution.

## RESUMO

Bombas de calor são equipamentos usados para o aquecimento de ambientes, para o fornecimento de água quente ou para outros fins de aquecimento. O número desses sistemas deve crescer 16 vezes até 2050, para contribuir com os objetivos do acordo de Paris. Apesar de possuírem uma eficiência relativamente alta, elas ainda precisam de desenvolvimento. Bombas de calor assistidas por energia solar (DX-SAHP) são uma alternativa para melhorar o desempenho de bombas de calor à ar (ASHP). Neste trabalho, o comportamento de uma bomba de calor à CO<sub>2</sub>, DX-SAHP, é investigado sob diferentes condições operacionais. No entanto, o dispositivo de expansão ajustável (por exemplo, válvula eletrônica - EEV), geralmente utilizado, foi substituído por um tubo capilar como uma alternativa para a redução dos custos de fabricação. Inicialmente, uma solução algébrica para dimensionar um tubo capilar adiabático helicoidal, operando em ciclo de CO<sub>2</sub> transcrito, foi desenvolvida. Três diferentes fatores de atrito e três diferentes fatores k, relacionados ao volume específico, foram analisados, criando um total de 9 possíveis combinações. Depois de dimensionar e montar os tubos capilares na bancada, testes foram realizados de acordo com o planejamento fatorial, com dois diferentes tubos capilares e 3 diferentes condições operacionais, a saber: alta radiação solar (HSR), baixa radiação solar (LSR) e baixa radiação solar com ventilador (LSR+fan). Os resultados indicaram um aumento médio de 57.9% na capacidade de aquecimento, 42.3% no COP e 35% na vazão mássica de refrigerante, quando se muda de LSR (6 W/m<sup>2</sup>) para HSR (969 W/m<sup>2</sup>). O grau de superaquecimento passou de 4.4 para 30.6°C, e a pressão de evaporação mudou de 40.0 para 51.2 bar. Mas a pressão no resfriador de gás também mostrou um aumento significativo, de 83.5 para 87.9 bar. Para limitar o aumento do superaquecimento e manter a integridade do compressor, pequenas modificações são recomendadas. Alterando-se de LSR para LSR+fan, ocorreu uma melhoria de 17.2% na capacidade de aquecimento sem penalização para o COP, mostrando que a adição do ventilador é vantajosa em baixas radiações solares. À parte do planejamento fatorial, testes adicionais foram realizados para aumentar o número de pontos experimentais para validar a solução algébrica do tubo capilar. Em geral, o fator de atrito C-M&N demonstrou ser o melhor para a solução proposta. Os percentuais de pontos de vazão mássica previstos dentro de faixas de erro de 10% e 15% foram 95% e 100%, respectivamente, para a melhor combinação.

Palavras-chave: bomba de calor. Redução de custo. Tubo Capilar. CO<sub>2</sub>. DX-SAHP. Solução Algébrica.

## LIST OF FIGURES

Figure 2.1: Share of water heating energy consumption to the total building energy consumption in 2010 .....	19
Figure 2.2: Schematic ph diagram: a) Transcritical cycle; b) subcritical cycle .....	21
Figure 2.3: Example of SAHP's: a) parallel concept; b) serial concept.....	26
Figure 2.4: Arrangement examples of: a) DX-SAHP; b) indirect-serial SAHP; c) indirect-parallel SAHP .....	27
Figure 2.5: Schematic representation of the refrigerant flow through a capillary tube: a) ph diagram; b) regions over the capillary length.....	33
Figure 3.1: ph diagram with the integrating limits: a) left of the critical point; b) right of the critical point.....	49
Figure 3.2: Cross section area after the cut test: a) with thin saw blade; b) with EDM machine. ....	53
Figure 3.3: EDM machine used to cut the capillary tubes.....	54
Figure 3.4: Microscope used for the inner diameter measurements.....	55
Figure 3.5: Sample 1D1 amplified 30 times.....	55
Figure 3.6: Stylus profilometer.....	56
Figure 3.7: Optical profilometer.....	57
Figure 3.8: Sequence of the capillary tube assembling. ....	59
Figure 3.9: Overview of the CO2 DX-SAHP.....	61
Figure 3.10: Top view of the workbench: a) before modifications; b) after modifications. ....	62
Figure 3.11: Compressor. ....	62
Figure 3.12: Oil separator.....	63
Figure 3.13: Gas cooler: Picture of the coil heat exchanger; b) schematic representation.....	63
Figure 3.14: Needle valve.....	64
Figure 3.15: Dryer filter.....	64
Figure 3.16: Evaporator/collector.....	65
Figure 3.17: Liquid separator. ....	65
Figure 3.18: Water pump.....	66
Figure 3.19: Pressure meters. ....	66
Figure 3.20: Pyranometer. ....	67
Figure 3.21: Wattmeter.....	68
Figure 3.22: Schematic representation of the workbench. ....	70



Figure 3.23: Experiments location and meteorological station location. ....	72
Figure 4.1: Variation of evaporating and gas cooler pressures with solar radiation, for two different experiments. ....	78
Figure 4.2: Ph diagram of experiments A1, B1, and C1. ....	78
Figure 4.3: Main effects plots for: a) evaporating pressure; b) gas cooler pressure; c) refrigerant mass flow rate; d) heating capacity; e) superheat degree; f) COP.....	79
Figure 4.4: Comparison between capillary tubes levels: a) refrigerant mass flow rate; b) evaporating pressure; c) gas cooler pressure. ....	80
Figure 4.5: Comparison between operational conditions levels: a) superheat degree; b) COP; c) gas cooler pressure. ....	81
Figure 4.6: Deviations from predicted and measured mass flow rates for combination: a) 1; b) 2; c) 4; d) 5; e) 7; f) 8.....	84
Figure 4.7: Deviations from predicted and measured mass flow for rate combination 1: a) capillary tube 1; b) capillary tube 4. ....	85

## LIST OF TABLES

Table 2.1: Characteristics of some refrigerant fluids .....	20
Table 2.2: Safety groups of refrigerant fluids.....	21
Table 2.3: Correlations for optimal pressure in transcritical CO <sub>2</sub> systems.....	22
Table 2.4: Correlations for mass flow rate prediction in adiabatic straight capillary tubes. ....	38
Table 2.5: Correlations for mass flow rate prediction in adiabatic coiled capillary tubes. ....	38
Table 2.6: Dimensionless Pi groups used in the correlations.....	39
Table 3.1: Optimal pressures presented by different correlations. ....	52
Table 3.2: Capillary tube dimensions and corresponding operational conditions.....	52
Table 3.3: Roughness values for the new $\varepsilon Fp$ definition.....	57
Table 3.4: Final dimensions of the capillary tubes with the respective uncertainties. ....	59
Table 3.5: Factors and levels. ....	61
Table 3.6: Main parameters of the gas cooler .....	64
Table 3.7: Main parameters of the evaporator/collector.....	65
Table 3.8: Pressure meters main specifications.....	66
Table 3.9: Main pyranometer specifications. ....	67
Table 3.10: Main wattmeter specifications.....	68
Table 3.11 Measured variables.....	70
Table 3.12 Calculated variables. ....	70
Table 4.1 Results of the factorial design. ....	76
Table 4.2 Uncertainties of the measured variables.....	76
Table 4.3 Experimental results for refrigerant mass flow rates.....	81
Table 4.4 Combinations of k and friction factors.....	83
Table 4.5 AD, ADD and RMS of the proposed algebraic solution, expressed in percent. ....	83
Table 4.6 Percentual of data points within error bands of 10%, 12%, and 15%.....	85

## ABBREVIATIONS

AAD	Absolute average deviation
AD	Average deviation
ANN	Artificial neural networks
ANOVA	Analysis of variance
ASHP	Air source heat pump
CFC	Chlorofluorocarbons
CO <sub>2</sub>	Carbon dioxide
COP	Coefficient of performance
DHW	Domestic hot water
DX-SAHP	Direct-expansion solar-assisted heat pump
EDM	Electrical discharge machining
EEV	Electronic expansion valve
GHG	Greenhouse gases
GREA	UFMG Cooling and Heating Group
GWP	Global warming potential
HCFC	Hydro-chlorofluorocarbons
HEM	Homogeneous equilibrium model
HFC	Hydro-fluorocarbons
HFO	Hydrofluoro-olefins
HSR	High solar radiation
IEA	International Energy Agency
LPG	Liquefied petroleum gas
LSR	Low solar radiation
LSR+fan	Low solar radiation with fan
M&N	Mori and Nakayama (1967)
ODP	Ozone depletion potential
RMS	Root mean square
SAHP	Solar-assisted heat pump
SH	Space heating
TES	Thermal energy storage
TEV	Thermostatic expansion valve

## NOMENCLATURE

A	defined by Eq. 3.20b
a'	expected interval for the indications occurrence
a	parameter defined in Eq. 3.8
B	defined by Eq. 3.20c
b	parameter defined in Eq. 3.9
$c_p$	specific heat at constant pressure [kJ/kg.K]
D	capillary tube coil diameter [mm]
d	capillary tube inner diameter [mm]
e	internal energy [kJ/kg]
f	friction factor
FdRa	roughness parameter used in Eq. 2.23 [ $\mu\text{m}$ ]
g	gravity [ $\text{m/s}^2$ ]
G	mass flux [ $\text{kg/s.m}^2$ ]
h	enthalpy [kJ/kg]
$I_i$	i-th indication
j	defined by Eq. 3.11b
k	factor related to the specific volume
$k_{95}$	coverage factor
L	length [mm, m]
m	coefficient of Blasius' correlation, Eq. 3.27a
$\dot{m}$	refrigerant mass flow rate [kg/h]
$\dot{m}_w$	water mass flow rate [kg/h]
MI	average of indications
n	number of sample data
n'	number of turns in capillary tube coils
N	number of variables
p	pressure [Pa, bar]
$Q_h$	heating capacity [W]
$R_a$	arithmetic average roughness [ $\mu\text{m}$ ]
Rad	solar radiation [ $\text{W/m}^2$ ]
$Re$	Reynolds number, Eq. 3.21
$R_p$	maximum peak value of roughness [ $\mu\text{m}$ ]

$R_q$	root mean square roughness [ $\mu\text{m}$ ]
$R_z$	mean peak-to-valley roughness [ $\mu\text{m}$ ]
$S$	capillary tube coil pitch [mm]
$t$	defined by Eq. 3.13
$T$	temperature [ $^{\circ}\text{C}$ ]
$T_d$	bias
$T_{d_c}$	combined bias
$T_{d_i}$	i-th bias
$U$	expanded uncertainty
$u$	defined by Eq. 3.14
$u'$	standard uncertainty
$u'_c$	combined uncertainty
$u'_i$	i-th standard uncertainty
$v$	specific volume [ $\text{m}^3/\text{kg}$ ]
$V$	water volumetric flow rate [ $\text{m}^3/\text{h}$ ]
$\vec{V}$	velocity vector [m/s]
VVC	true value
$\dot{W}$	electrical power [W]
$x$	quality
$x'$	defined by Eq. 3.24b
$\alpha$	coefficient of Blasius' correlation, Eq. 3.27a
$\Delta T$	superheat degree [K]
$\Delta T'$	subcooling degree [K]

### **Greek letters**

$\varepsilon$	capillary tube surface roughness [ $\mu\text{m}$ ]
$\varepsilon_{Fp}$	roughness parameter defined by Eq. 2.23 [ $\mu\text{m}$ ]
$\theta$	defined by Eq. 3.25b
$\lambda$	the thermal conductivity [W/m.K]
$\mu$	dynamic viscosity [Pa.s]
$\nu$	degrees of freedom
$\nu_{ef}$	effective degrees of freedom
$\nu_i$	i-th degree of freedom
$\rho$	density [ $\text{kg}/\text{m}^3$ ]

$\sigma$	surface tension [N/m]
$\tau_{ij}$	viscous-stress tensor [Pa]
$\phi$	viscous-dissipation function
$\Phi$	parameter in Eq. 2.11
$\psi$	defined By Eq. 3.26c

### Subscripts

1	compressor inlet
1'	evaporator/collector outlet
2	gas cooler inlet
3	gas cooler outlet
4	expansion device outlet
A	ambient
c	coiled capillary tube
cond	condensing
crit	critical
evap	evaporating
f	saturated liquid
g	saturated vapor
in	capillary tube inlet
opt	optimal
out	capillary tube outlet
r	reference/flash point
s	straight capillary tube
sp	single-phase
tp	two-phase
w1	water at the inlet of the gas cooler
w2	water at the outlet of the gas cooler

## TABLE OF CONTENTS

1	INTRODUCTION .....	17
1.1	Objectives .....	18
2	REVIEW.....	19
2.1	Carbon dioxide .....	20
2.2	Transcritical CO <sub>2</sub> heat pump.....	21
2.2.1	Optimal pressure.....	22
2.2.2	Studies on transcritical CO <sub>2</sub> systems .....	23
2.3	SAHP.....	25
2.3.1	Reviews on DX-SAHP .....	27
2.4	Capillary tube .....	31
2.4.1	Numerical models.....	33
2.4.2	Algebraic solutions .....	35
2.4.3	Dimensionless correlations.....	36
2.4.4	Experimental studies .....	40
2.5	Surface roughness and pressure drop .....	42
2.6	Concluding remarks from review .....	44
3	METHODOLOGY .....	46
3.1	Capillary tube algebraic solution.....	46
3.2	Capillary tube sizing and assembling .....	52
3.2.1	Geometric characterization.....	53
3.2.1.1	Inner diameter measurements.....	54
3.2.1.2	Internal surface roughness measurements.....	55
3.2.1.3	Length and coil diameter measurements.....	58
3.2.2	Final dimensions and assembling.....	59
3.3	Experimental characterization .....	60
3.3.1	Design of experiments .....	60

3.3.2	Workbench description.....	61
3.3.2.1	Compressor.....	62
3.3.2.2	Oil separator .....	63
3.3.2.3	Gas cooler.....	63
3.3.2.4	Expansion devices .....	64
3.3.2.5	Dryer filter.....	64
3.3.2.6	Evaporator/collector .....	64
3.3.2.7	Liquid separator.....	65
3.3.2.8	Water pump .....	65
3.3.2.9	Measurement and data acquisition system.....	66
3.4	Experimental procedure.....	69
3.5	Uncertainty analysis .....	72
3.5.1	Direct measurements .....	72
3.5.2	Indirect measurements .....	73
3.6	Validation of the capillary tube algebraic solution.....	74
4	RESULTS AND DISCUSSIONS .....	76
4.1	Experimental results and heat pump behavior.....	76
4.2	Results of the capillary tube algebraic solution validation.....	81
5	Conclusions .....	86
6	REFERENCES .....	88
	APPENDIX A – GEOMETRIC CHARACTERIZATION OF THE CAPILLARY TUBES..	97
	APPENDIX B – VERIFICATION OF THE MEASUREMENT INSTRUMENTS .....	102



## 1 INTRODUCTION

Heat pumps are systems used to promote space heating, supply hot water or used for other heating purposes. Their application is well established in the residential sector, mainly in countries of the northern hemisphere. In tropical countries, especially in Brazil, they have been used for swimming pool heating. However, large-scale heat pumps in the industrial sector are also employed (EHPA, 2019a; 2019b).

In the residential sector, great part of the energy consumption is due to the hot water production, especially for bath. Different sources of energy are commonly used for this purpose, such electricity, solar radiation and natural gas. Solar collectors and heat pumps represent a more efficient way to supply domestic hot water (DHW) compared to electric showers. The first can have null or almost null operating costs compared to a heat pump, but in rainy, cloudy and unstable solar radiation days, the hot water production could be compromised. On the other hand, heat pumps can supply DWH regardless the weather conditions.

Despite the higher efficiency, 3 to 5 times (JOHRA ET AL., 2019), compared to electric showers, and higher reliability than solar collectors, heat pumps still need improvements, such the efficiency raise to further reduce its energy consumption. In this sense, one alternative is to integrate a solar collector onto the heat pump evaporator. This combination, called direct-expansion solar assisted heat pump (DX-SAHP), has the reliability of traditional air source heat pumps (ASHP) and higher efficiency when solar radiation is available. Another possibility to improve heat pumps is to reduce its manufacturing costs. This can be achieved by using lower cost components, but without losing efficiency. One possibility is the use of capillary tubes instead of electronic or needle valves as the expansion device.

Recently, many numerical and experimental studies about DX-SAHP are being performed. Some fields of interest are the systems performance under different weather conditions, different applications, components optimization, and the selection of refrigerant fluids more environmentally friendly. Among these refrigerants, it can be mentioned the hydrofluoro-olefins (HFO), hydrocarbons and carbon dioxide (CO<sub>2</sub>).

In this work, the technical viability of adopting a capillary tube in a DX-SAHP used for DHW production, operating in transcritical CO<sub>2</sub> cycle, is investigated. An algebraic solution to design an adiabatic coiled capillary tube for transcritical CO<sub>2</sub> cycle is proposed. Subsequently, two

different capillary tubes are manufactured and assembled onto the DX-SAHP. Experimental tests are carried out to analyze the coefficient of performance (COP), superheat degree and heating capacity under different operating conditions. Finally, the capillary tube algebraic solution is compared with the experimental data for validation.

### **1.1 Objectives**

The general objective of this work is to analyze the performance of a CO<sub>2</sub> DX-SAHP operating with an adiabatic coiled capillary tube.

Specific objectives of this work are:

- To propose an algebraic solution for an adiabatic coiled capillary tube operating in a transcritical CO<sub>2</sub> cycle;
- To size and to assemble the coiled capillary tube in the DX-SAHP;
- To validate the capillary tube algebraic solution with the experimental data.

## 2 REVIEW

The discussions about energy and sustainability are always current and relevant. Along the years, several international agreements to limit environment damages were proposed. In 1987, the International treaty called to Montreal Protocol was established, in consequence of the Vienne convention in 1985, to limit progressively the use of substances with ozone depletion potential (ODP). Later, in 1997, the Kyoto Protocol proposed to reduce the emissions of gases with high global warming potential (GWP), called greenhouse gases (GHG). Subsequently, at the 21<sup>st</sup> session of the Conference of the Parties - 2015, the Paris Agreement was firmied with the purpose to further reduce the GHG emissions to limit the rise in average global temperature in the present century around 2°C, and ideally, below 1.5°C.

To reach the Paris agreement objectives, among other actions, it is necessary to strongly raise the end-use electrification of heat, using renewable sources (IRENA, 2019). For instance, water heating for domestic purposes, either for bath or space heating, is a major energy consumer in many countries. Figure 2.1 illustrates the ratio of energy consumption due to water heating to the total building energy consumption, in residential and service sectors, at different world regions.

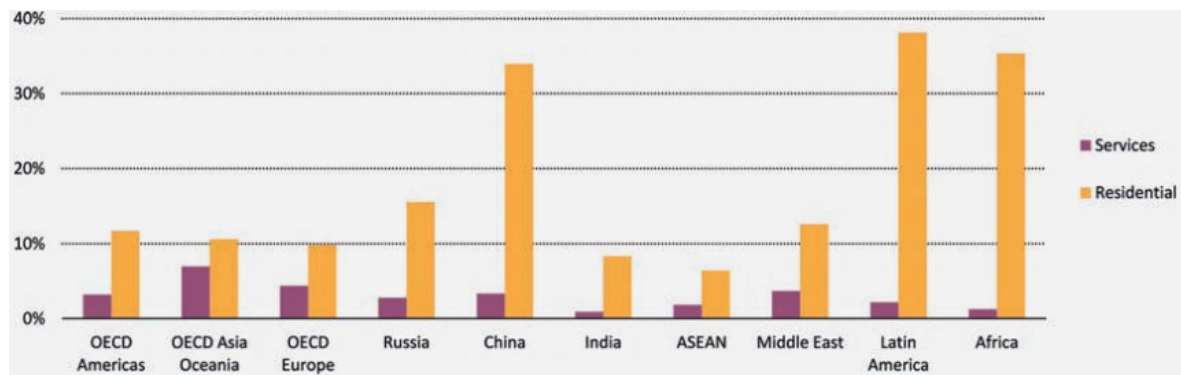


Figure 2.1: Share of water heating energy consumption to the total building energy consumption in 2010  
Source: IEA, 2013.

In Middle East, between 2000 and 2010, nearly 90% of the energy used for water heating came from oil and natural gas technologies, while in China, Africa, and Latin America traditional biomass remains a common form to heat water (IEA, 2013). According to IRENA (2019), the number of installed heat pumps in 2017/2018 should raise 16 times, to reach 334 million units by 2050, as the contribution of the heat sector to meet the Paris agreement objectives. In this

sense, the development of more efficient heat pumps and the selection of refrigerant fluids more environmentally friendly are essential.

## 2.1 Carbon dioxide

With the restrictions of chlorofluorocarbons (CFCs) and hydro-chlorofluorocarbons (HCFCs) and the crescent reduction of hydro-fluorocarbons (HFCs), other types of refrigerants have gained attention, such the HFOs (e.g. R1234yf, R1234ze) and the called “natural refrigerants” (e.g. hydrocarbons, ammonia, CO<sub>2</sub>, etc).

In particular, carbon dioxide (R744) was commonly employed as a refrigerant fluid from the late 19<sup>th</sup> century, but phased-out after the advent of CFCs due to the loss of capacity at high ambient temperatures. However, in the 1990’s, CO<sub>2</sub> was revived as a good alternative, due to its non-toxicity, non-flammability, complete harmlessness and good thermophysical properties. Different applications such as in car air-conditioners, heat pumps and commercial refrigeration have demonstrated to be suitable for R744 usage (LORENTZEN, 1994). The main difference in today’s and earliest carbon dioxide systems is the operation in transcritical cycle, necessary to adapt to higher ambient temperatures, leading to high operating pressures and demanding more robust components. CO<sub>2</sub> also present null ODP and low GWP, seen in comparison with common refrigerant fluids in Table 2.1, together with some other properties. The legend for the safety group can be seen in Table 2.2.

Table 2.1: Characteristics of some refrigerant fluids

Refrigerant type	Refrigerant Number	ODP	GWP (100 years)	Critical pressure [MPa]	Critical temperature [°C]	Atmospheric lifetime [years]	Safety group
CFC	12	1	10900	4.136	111.97	100	A1
HCFC	22	0.055	1790	4.990	96.145	11.9	A1
HFC	134a	0	1300	4.059	101.06	13.4	A1
HFO	1234yf	0	<4,4	3.382	94.7	0.029	A2L
"natural"	290	0	20	4.251	96.74	0.041	A3
"natural"	600a	0	20	3.629	134.66	0.016	A3
"natural"	744	0	1	7.377	30.978	>50	A1

Source: ASHRAE, 2013.

Table 2.2: Safety groups of refrigerant fluids

<b>Toxicity</b>	<b>A</b>	Refrigerants that have occupational exposure limit $\geq 400$ ppm
	<b>B</b>	Refrigerants that have occupational exposure limit $< 400$ ppm
<b>Flammability</b>	<b>1</b>	No flame propagation in air at 60°C and 101.3 kPa
	<b>2</b>	Exhibits flame propagation in air at 60°C and 101.3 kPa; lower flammability limit $> 0.10$ kg/m <sup>3</sup> at 23°C and 101.3 kPa; heat of combustion $< 19000$ kJ/kg
	<b>2L</b>	class 2 refrigerants that exhibit maximum burning velocity $< 100$ mm/s at 23°C and 101.3 kPa
	<b>3</b>	Exhibits flame propagation in air at 60°C and 101.3 kPa; lower flammability limit $\leq 0.10$ kg/m <sup>3</sup> at 23°C and 101.3 kPa; heat of combustion $\geq 19000$ kJ/kg

Source: ASHRAE, 2013.

## 2.2 Transcritical CO<sub>2</sub> heat pump

Compared to other common refrigerants used in heat pumps and refrigeration systems, CO<sub>2</sub> (R744) has a low critical temperature, 31 °C. This means that condensation process occurs only below this value. However, in many cases, this temperature level is much lower than the necessary for rejecting heat to a secondary fluid (e.g. water, ambient air). In such situations, the heat rejection will occur at the supercritical fluid region, without condensation, while other parts of the cycle take place at subcritical regions. Under these operating conditions, the system is called transcritical cycle. Once the refrigerant at the high side pressure is in supercritical thermodynamic state, often referred to as gas condition, the term condenser is replaced by gas cooler (DANFOSS, 2008). Figure 2.2 illustrates the pressure versus enthalpy diagram for subcritical and transcritical systems.

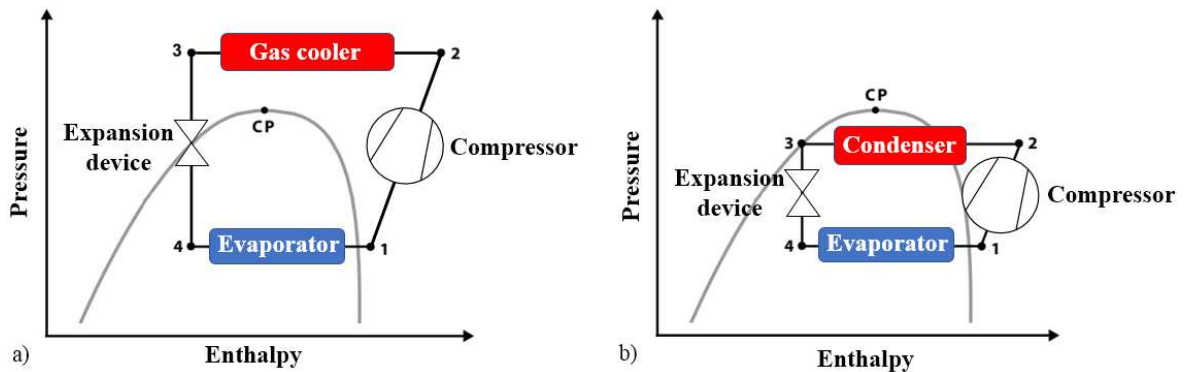


Figure 2.2: Schematic ph diagram: a) Transcritical cycle; b) subcritical cycle

For subcritical cycles, the condensing temperature (and subcooling degree, if necessary) is enough to specify the high side condition. However, for transcritical cycles, there is no condensation process. The fluid temperature and pressure are independent parameters and both must be specified. According to Madsen et al. (2005), in transcritical CO<sub>2</sub> systems, the refrigerant temperature at the gas cooler outlet is often governed by the room temperature and,

therefore, the pressure is the only parameter that could be controlled. For a fixed temperature at the gas cooler outlet, the system performance alters as the pressure varies, existing a specific pressure for the given temperature in which the COP of the system is the best.

### 2.2.1 Optimal pressure

Many theoretical and experimental researches have been made to determine the optimal high pressure, i.e. the high pressure that yields to the best COP, with other parameters kept constant. Some correlations for the optimal pressure are listed in Table 2.3.

Table 2.3: Correlations for optimal pressure in transcritical CO<sub>2</sub> systems.

Authors	Equation for optimal pressure	Theoretical / Empirical	Application range	Eq. number
Kauf (1999)	$2.6T_3 + 7.54$	Theoretical with no experimental validation	$35^\circ\text{C} \leq T_A \leq 50^\circ\text{C}$	(2.1)
Liao et al. (2000)	$(2.778 - 0.0157T_{\text{evap}})T_3 + (0.381T_{\text{evap}} - 9.34)$	Theoretical with no experimental validation	-	(2.2)
Chen and Gu (2005)	$2.68T_3 - 6.797$	Theoretical with experimental validation	$-10^\circ\text{C} \leq T_{\text{evap}} \leq 10^\circ\text{C}$ $35^\circ\text{C} \leq T_3 \leq 50^\circ\text{C}$ $80 \text{ bar} \leq p_3 \leq 135 \text{ bar}$ $x = 1$	(2.3)
Cecchinato and Corradi (2011)	$0.00689T_3^2 + 1.5483T_3 + 35.676$	Empirical	-	(2.4)
Qi et al. (2013)	$132.3 - 8.4T_3 + 0.3T_3^2 - 0.00277T_3^3$	Empirical	$-15^\circ\text{C} \leq T_A \leq 30^\circ\text{C}$ $25^\circ\text{C} \leq T_3 \leq 45^\circ\text{C}$	(2.5)
Yang et al. (2015)	$2.918T_3 + 0.471T_{\text{evap}} - 0.018T_{\text{evap}}T_3 - 13.955$	Theoretical with no experimental validation	$-10^\circ\text{C} \leq T_e \leq 20^\circ\text{C}$ $30^\circ\text{C} \leq T_3 \leq 60^\circ\text{C}$ Superheat of $5^\circ\text{C}$	(2.6)
Song et al. (2017)	$16.5571 + 1.4329T_3 + 0.0157T_3^2$	Empirical	$30^\circ\text{C} \leq T_3 \leq 50^\circ\text{C}$	(2.7)

Besides the works listed in Table 2.3, Cecchinato et al. (2010) numerically evaluated the optimal pressure, comparing the results with existing correlations. Considering a coaxial gas cooler, the optimal pressures predicted by the proposed model were higher than the ones given by Liao's correlation. Later, Cecchinato and Corradi (2011) found the same trend in an experimental investigation of a small cooling systems, operating with a capillary tube as the expansion device. As the ambient temperature gets lower, the experimental optimal pressure moves from Liao's correlation prediction to the proposed correlation prediction. Besides, one

of the author's conclusion is that the capillary tube is able to adjust the high pressure close to the optimal value, in order to match the mass flow rate variation imposed by the compressor.

According to Yang et al. (2015), the major COP degradation occurs for gas cooler outlet temperature close to the critical temperature. Besides, as closer to the critical temperature is the gas cooler outlet temperature, as high is the COP variation around the optimal high pressure. In all cases, this effect is more sensitive for under pressure than for overpressure.

### **2.2.2 Studies on transcritical CO<sub>2</sub> systems**

Agrawal and Bhattacharyya (2011) experimentally analyzed adiabatic capillary tubes in a transcritical CO<sub>2</sub> heat pump for simultaneous heating and cooling. The test facility used comprises a reciprocating compressor with capacity of 2.5 kW at 2900 rpm, a gas cooler, a water evaporator and two expansion devices in parallel: a straight capillary tube, with internal diameter of 1.42 mm and length of 1 m, and a needle valve. They argue that the refrigerant charge is an important parameter that affects the performance of the refrigeration system, when operating with a capillary tube. Besides, CO<sub>2</sub> systems tend to be more sensitive to the refrigerant inventory compared to conventional systems. During the experiments, the operational conditions ranged from: 25 to 40°C for the water temperature at the gas cooler inlet, 1.0 to 1.5 kg/min for the water mass flow rate at the gas cooler, 1.0 to 3.5 kg/min for the water mass flow rate at the evaporator and 0.5 to 0.95 kg for the refrigerant charge. The authors related a marginal variation in the evaporator pressure for the entire set of tests. However, the gas cooler pressure varied significantly with the water inlet temperature and modestly with the water mass flow rate. Regarding the refrigerant charge, there is an optimum condition at which the system yields to the best COP. The performance decrease showed to be more severe at undercharged conditions than at overcharged conditions.

Song et al. (2017) numerically and experimentally investigated the adaptivity of a transcritical CO<sub>2</sub> refrigeration system operating with a capillary tube in different conditions. They compared the performance of the capillary tube-based system with the electronic expansion valve (EEV) based system, under various gas cooler outlet temperatures. To develop the model for the capillary tube, mass and energy conservation equations, and momentum equation were used, considering metastable and one-dimensional flow. In the experimental setup, the main components are: a semi-hermetic reciprocating compressor, a gas cooler, an evaporator, an EEV and a capillary tube installed in parallel. In order to identify the optimum high pressure, the

system branch with the EEV was used, and an experimental correlation was proposed. Then, three capillary tubes were designed to operate at optimum high pressures, with evaporating pressure of 3.7 MPa, 10°C of superheat and gas cooler outlet temperature of 30°C, 35°C and 40°C, respectively. During the tests, the gas cooler outlet temperature ranged from 30°C to 50°C. Although some experimental results did not show good agreement with the simulated parameters, the authors concluded that the difference between the high pressure of the capillary tube and EEV systems can be small and, therefore, the adaptability of the capillary tube can be assumed. With the gas cooler outlet temperature 10°C higher than the design value, the relative COP of the capillary system, compared to the optimum conditions, was 82%, 88% and 98%, respectively, corresponding to 30°C, 35°C and 40°C for the design values of the gas cooler outlet temperatures.

Wang et al. (2018) numerically and experimentally studied the optimal combination of a capillary tube geometry and the refrigerant charge in a small CO<sub>2</sub> water-to-water heat pump. According to the authors, these two parameters are coupled, rather than independent, in a small system. They proposed a steady-state thermodynamic model, comprising two sub-models: an energy thermodynamic model and a homogeneous equilibrium model for the capillary tube. To design the system, the following conditions were established: gas cooler outlet temperature of 34°C, evaporating temperature of 3°C, optimal high pressure of 8.465 MPa and refrigerant charge of 0.255 kg or 0.262 kg. At those conditions, the predicted length of the capillary tube was 4.24 m with an inner diameter of 1 mm. In order to verify the model optimal combination, a set of experiments was carried out. Four capillary lengths were chosen: 4.1 m, 4.0 m, 3.9 m and 3.8 m. The refrigerant charge varied from 230 g to 300 g, every 10 g. The main components of the experimental facility are: a hermetic reciprocating compressor, a gas cooler, a capillary tube, an evaporator and an internal heat exchanger. The experimental results indicated that the best combination (highest COP) was the refrigerant charge of 270 g and capillary tube length of 3.9 m. It was also noted that the heating performance is very sensitive to the refrigerant charge, especially at undercharged conditions. This effect was more significant for longer capillary tubes, although the authors have not highlighted this point.

Wang et al. (2020a) experimentally analyzed a transcritical CO<sub>2</sub> ASHP operating with a thermal energy storage (TES) system. They studied the effect of water inlet temperature at the gas cooler, the ambient temperature, and other aspects on throttle loss and on ASHP COP. A theoretical analysis showed that the higher the CO<sub>2</sub> temperature at the gas cooler outlet, the



higher the throttle loss and the lower the COP. They argue that an effective option to reduce the CO<sub>2</sub> temperature is to integrate a TES system. Regarding the experimental apparatus, the system consists in two cycles: the heat pump unit, and the water loop. The first is comprised by: a compressor, a gas cooler, an internal heat exchange, an EEV and an evaporator. The second is composed by two TES tanks, with different phase change materials, a water pump, and a radiator (space heater). The results showed that the throttle loss is higher with lower ambient temperatures. Besides, the authors found a 17% increase in COP when using the TES system together with the ASHP, for the same thermal load.

### **2.3 SAHP**

Different alternatives are being investigated to raise the energetic efficiency of heat pumps. One of such technologies is the solar assisted heat pump (SAHP), which is a system that combines the use of solar radiation and the thermal energy available in the air to promote space heating (SH), to supply domestic hot water (DHW) or to be used for other purposes. This combination can promote a COP increase from about 1 to almost 3.75, when compared with traditional air source heat pumps (ASHP) (WANG ET AL., 2020b). Due to the wide range of component types and possible arrangements, SAHP can be classified in different ways. The International Energy Agency (IEA) through the Solar Heating and Cooling Programme, Task 44, recommends to classify SAHP in four groups: parallel, serial, regenerative and complex (HADORN, 2012). In the parallel concept, collector and heat pump independently supply DHW or SH via a storage tank. In the serial arrangement, solar collectors work as an energy source for the heat pump, directly, or indirectly via a buffer storage. The regenerative uses the solar radiation to warm the main energy source of the heat pump. Lastly, the complex concept can be a combination of the previous configurations (POPI ET AL., 2018). Figure 2.3 illustrates the parallel and series SAHP concepts.

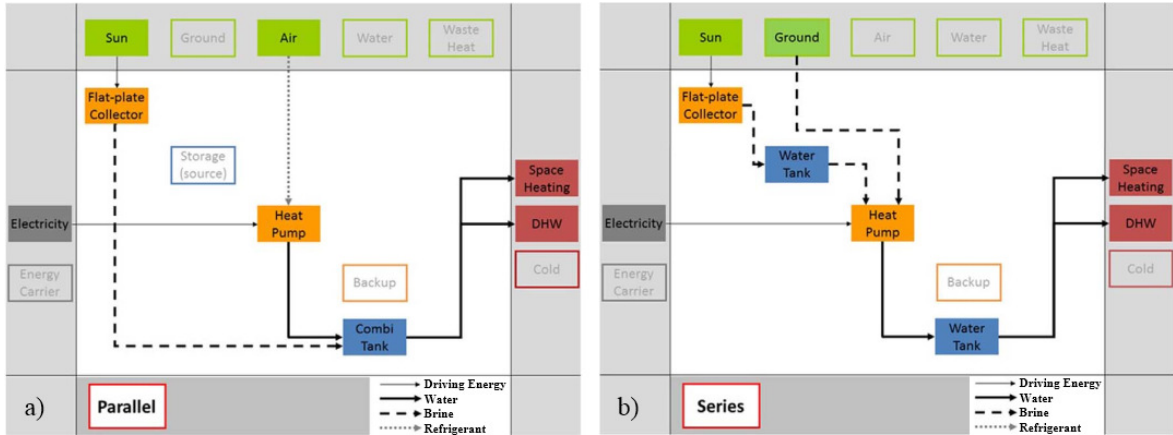
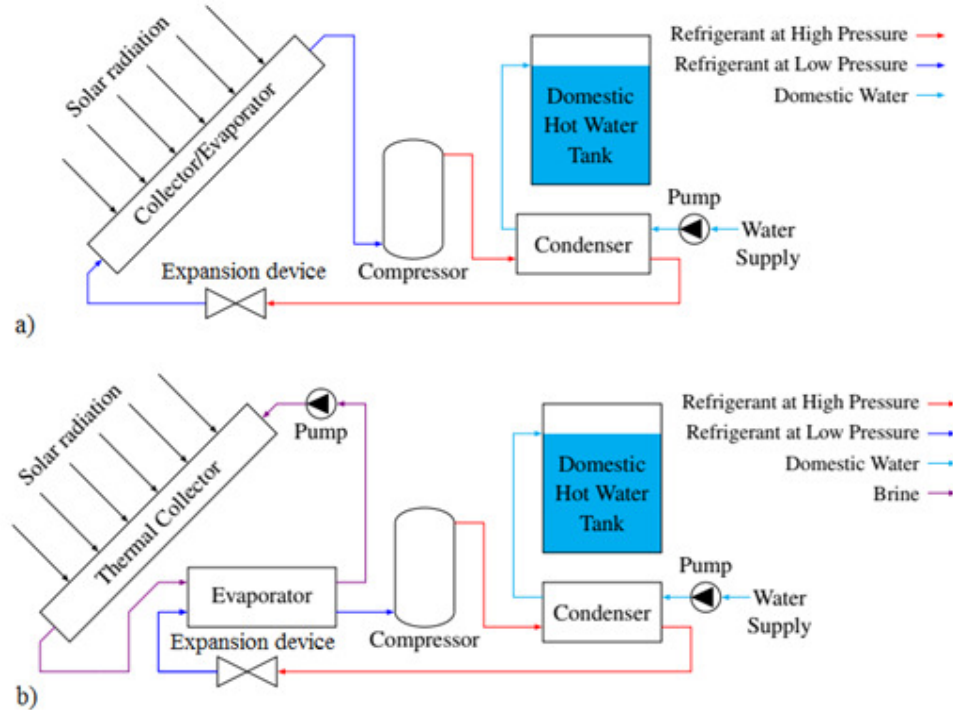


Figure 2.3: Example of SAHP’s: a) parallel concept; b) serial concept  
 Source: Popi et al., 2018.

Other authors simply classify the SAHP in two types: direct and indirect (LEE ET AL., 2018; ZHOU ET AL., 2020). In the direct configuration, the evaporator is integrated to the collector and the refrigerant fluid is directed evaporated by solar radiation. Such systems are called direct-expansion solar-assisted heat pumps (DX-SAHP). Figure 2.4 illustrates arrangements of DX-SAHP, indirect-serial SAHP and indirect-parallel SAHP.



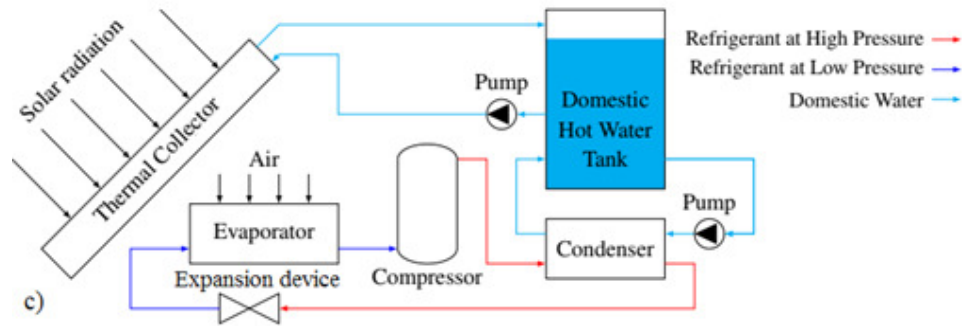


Figure 2.4: Arrangement examples of: a) DX-SAHP; b) indirect-serial SAHP; c) indirect-parallel SAHP

Source: Duarte, 2018.

### 2.3.1 Reviews on DX-SAHP

Kong et al. (2018) experimentally studied a DX-SAHP, running with R134a, for heating water purpose. Their prototype is composed by a variable-frequency rotary-type compressor, a micro-channel condenser, surrounding a 200 L water tank, an electronic expansion valve, and a flat plate evaporator/collector. They analyzed the impact of different parameter, such the solar radiation and ambient temperature, on the heat pump performance. The authors found a 28% improvement in COP when the solar radiation increases from 258 to 634 W/m<sup>2</sup>. Besides, they verified that the evaporating pressure also increased with the solar radiation, but the condensing pressure was not significantly influenced. Regarding the ambient temperature, the behavior was similar, with higher COP and evaporating pressures for higher ambient temperature, while the condensing pressure was not significantly affected.

Paulino et al. (2019) numerically and experimentally studied the evaporator dynamic behavior of a transcritical CO<sub>2</sub> DX-SAHP when it is submitted to solar radiation variations. They developed a distributed model to analyze the dynamic response of the superheat at the evaporator outlet and the corrective effect of the expansion device. The main components of the experimental apparatus are: an evaporator/collector, a 1.75 cm<sup>3</sup> reciprocating compressor, a gas cooler/hot water reservoir and a needle valve. During the test, the ambient temperature, the relative humidity and the inlet water temperature at the gas cooler were, 26°C, 50% and 25.8°C. A PID controller kept the outlet water temperature at 60°C. Initially, the heat pump was exposed to a solar radiation of 767 W/m<sup>2</sup> and, after reaching the steady-state, radiation was reduced to 80 W/m<sup>2</sup>. Finally, the solar radiation increased to 797 W/m<sup>2</sup>, 4% higher than the initial condition. The authors noticed an almost immediate reduction in the evaporating temperature and in the superheat when the solar radiation is reduced. For 80 W/m<sup>2</sup> of solar

radiation, the experimental superheat and evaporating temperature was 4.8°C and 16.2°C, versus 5.0°C and 17.5°C predicted by the mathematical model. Besides, a variation of only 2% in the compressor volumetric efficiency was detected when the solar radiation changed from the high to the low level. One of the authors' conclusion is that an EEV would be more suitable to meet the needs of rapid interventions on the mass flow rate at the evaporator inlet.

Mohamed et al. (2019) theoretically and experimentally studied a direct-expansion solar-assisted multifunctional heat pump used for simultaneous air and water heating. The objective is to decrease the temperature difference between the evaporator/collector and the condenser, enhancing the heating capacity at lower ambient temperatures. The system operates with the refrigerant R407C and the main workbench components are: a variable speed hermetic compressor with 800 W of power at 50 Hz, two condensers in parallel (air and water), a hot water tank (200 L), a thermostatic expansion valve and an evaporator/collector. This last one differs from a traditional evaporator/collector once it incorporates a plate internally mounted in the house loft space to absorb domestic wasted heat. The system can work at space heating only, water heating only or space and water heating. The experiments were carried out indoor and a solar simulator was used to supply the radiation, which varied from 0 to 200 W/m<sup>2</sup>. The experimental results for the COP on space-heating-only mode ranged from 2.8 to 3.9 when the radiation changed from 0 to 200 W/m<sup>2</sup>, considering the inlet and outlet air temperature around 7°C and 25°C, respectively. On space-and-water-heating mode the COP ranged from 2.8 to 3.4. The authors concluded that the proposed system can sufficiently heat water and air during the United Kingdom winter, even under no solar radiation.

Shi et al. (2019a) developed a distributed parameter model to numerically study the innovative idea of integrating a DX-SAHP with a liquefied petroleum gas (LPG) vaporizer. The main purpose is to quantify and understand the performance of the integrated system, considering the variations of gas load and weather conditions. Basically, the DX-SAHP heats water, which is used at the LPG vaporizer. The DX-SAHP uses R417a as the refrigerant and the main components are: a 48.8 cm<sup>3</sup> compressor, a condenser immersed in a 970 kg water tank, a thermostatic expansion valve and an evaporator/collector. The water initial temperature inside the tank is 15°C and the temperature sets to turn the compressor on and off are 45°C and 55°C, respectively. The authors utilized the Beijing typical meteorological year data and the gas load of a community with 3500 residents as part of the inputs to run the simulations. Six operating modes can be selected depending on weather conditions and level of gas load. The better heat

pump performance was achieved during summer, with average monthly COP of 3.37, versus 2.72 during winter. Besides, a winter day with the highest gas load (15<sup>th</sup> February) and the summer day with the lowest gas load (15<sup>th</sup> July) presented minimum and maximum COP of 2.35 and 3.80, respectively.

Rabelo et al. (2019) experimentally studied the influence of the expansion valve opening on the performance of a DX-SAHP, operating in transcritical CO<sub>2</sub> cycle. The experimental apparatus is composed by a hermetic reciprocating compressor, a gas cooler, a needle valve, a flat plate evaporator/collector, an oil separator, and a reservoir. They investigated the heat pump behavior under low and high radiation conditions of 48 and 715 W/m<sup>2</sup>, respectively. The results showed that the rise in solar radiation has little effect on the gas cooler outlet pressure. They also reported an increase of 14% in evaporating pressure, 21% in the gas cooler heat transfer, 10% on CO<sub>2</sub> mass flow rate, and 21% on COP, for high radiation condition. Besides, they concluded that a fixed expansion device could be suitable to keep the system running close to its maximum performance, regardless the level of solar radiation.

Huang et al. (2019) numerically studied the performance of a DX-SAHP for space heating, under frost conditions. The proposed dynamic model was experimentally validated and then the influence of solar irradiation, ambient temperature and relative humidity on frost formation and on system performance were numerically investigated. The main workbench components are: a hermetic rotary compressor, an evaporator/collector a capillary tube and a condenser. The experiments were conducted in a laboratory, and the irradiation was investigated by means of a solar simulator. The refrigerant fluid used on experiments and simulations was not mentioned. For a given operating condition, the COP root mean square difference between predicted and experimental results was 5.06%. Regarding the simulations, for 70% of relative humidity, indoor temperature of 20°C and zero radiation, the authors found that for an ambient (outside) temperature of -1°C, the frost formation is the fastest. Keeping the other conditions constant and varying the irradiance, at 100 W/m<sup>2</sup> the COP was the worst, even compared to null radiation. They argue that the extra heat from solar energy is lower than the decrease of heat released by convection to the ambient, due to the increase in evaporating temperature. With relative humidity above 60% the COP increases monotonically. Overall, the frosting process benefits the heat transfer between evaporator and ambient air, improving the system performance.

Lu et al. (2019) experimentally investigated the performance of a photovoltaic/thermal vapor injection solar heat pump in winter. The main components of the proposed system are: a 41 cm<sup>3</sup> vapor injected scroll compressor, an internal heat exchanger, a condenser immersed in a 620 L water tank, two EEV and the evaporator/PVT modules. The experiments were conducted during 7 winter days, with the water being heated from 17°C to 50°C. The combined thermal and photovoltaic COP ( $COP_{PVT}$ ) was defined considering the summation of the heat released by the condenser with the power generated by the PVT modules, converted in thermal energy by an efficiency factor of 38%. In a day with averages ambient temperature and solar irradiation of 0.11°C and 939.60 W/m<sup>2</sup>, the best COP and  $COP_{PVT}$  were achieved, with values of 3.88 and 4.78, respectively. The experiment duration was the shortest, taking 157 min to heat water from 17°C to 50°C. The worse COP and  $COP_{PVT}$  were 3.27 and 3.45, respectively, in a day with averages ambient temperature and solar irradiation of -1.13°C and 164.03 W/m<sup>2</sup>. The experiment time was 199 min.

Duarte et al. (2019) theoretically analyzed the refrigerant selection to replace the R134a in a DX-SAHP. They developed a mathematical model, experimentally validated, to compare the performance and environmental impact of the DX-SAHP operating with the refrigerants R290, R600a, R744 (CO<sub>2</sub>), R1234yf and R134a. The heat pump is supposed to supply domestic hot water in a temperature of 65°C. The main experimental and model components are: a 200 L hot water tank, a hermetic reciprocating compressor, a thermostatic expansion valve and an immersed or coaxial condenser. The model validation was carried out comparing the predictions and experimental values of COP for both condensers, presenting a mean deviation of 1.6%, less than the 5% experimental uncertainty. Then, the simulations showed that R290 had the best COP in a solar radiation range from 300 to 700 W/m<sup>2</sup>, as well as for ambient temperatures between 10°C and 35°C, besides presenting the lowest total equivalent warming impact.

Fan et al. (2019) presented a theoretical study on a solar assisted ejector-compression heat pump system using the zeotropic mixture R290/R600a for water heating purpose. Besides the common components of a traditional heat pump, i.e. compressor, condenser/gas cooler, expansion device and evaporator, the proposed system also incorporates an ejector, a separator, a solar collector and a subcooler. Based in a set of simplifications and considering a condensing temperature of 60°C, an evaporating temperature of 10°C and the R600a/R290 ratio of 0.6, the authors found a COP and heating improvement of 29% and 31%, respectively, when compared

to a conventional heat pump. It was also shown that the COP initially raise with an increase in the R600/R290 ratio and after reaching a maximum, starts to decrease. The heating capacity is maximum for pure R290 and decrease until pure R600a is reached.

Shi et al. (2019b) presented a literature review and the major developments of DX-SAHP. Regarding the evaporator/collector, copper and aluminum are regarded as the ideal materials. However, despite of copper has the best thermal conductivity, COP improvement of only 0.5% was achieved with a copper made solar collector (1 mm plate thickness), compared with aluminum collector. Besides, the hexagon shape of the evaporator tube cross section area is the optimal geometric structure for a roll-bond panel. About the compressors, the scroll type may be more appropriate than the reciprocating one to enhance the thermal performance of the DX-SAHP. For low water temperature (below 60°C), single stages systems have been the focus of the DX-SAHP researches. But, for higher temperature applications, two-stage systems have significantly better COP. Concerning the thermodynamic optimization, it was shown that the highest exergy loss occurs in the compressor, followed by the collector/evaporator, condenser and expansion valve. However, exergy analyses have been performed in few studies.

## **2.4 Capillary tube**

The expansion device is one of the main components in a heat pump. It connects the outlet of the condenser/gas cooler to the inlet of the evaporator and regulates the refrigerant mass flow rate, while promoting a pressure drop. These devices can be classified in fixed and adjustable, according to its capacity to variate the internal cross section area. Part of the first group are: orifice plates, short orifice tubes, and capillary tubes. The second group, the adjustable, can still be subdivided in automatic and manual. In the first subdivision it can be mentioned the thermostatic expansion valve (TEV), and the electronic expansion valve (EEV), while in the later one, the needle valve is an example. Despite the capacity to adjust the mass flow rate, the adjustable expansion devices are too expensive compared with fixed ones.

In this context, the capillary tube is commonly used in small scale refrigeration or heat pump systems and consists in a segment of tube with constant cross-section area. Generally, its length varies from 1 to 6 m and the inner diameter from 0.5 to 2.0 mm (RASTI AND JEONG, 2018). Some advantages of using it include the low cost, zero maintenance, and lower compressor starting torque, due to the pressure equalization between the condenser and the evaporator during the off-cycle (MELO ET AL., 1999). On the other hand, a major drawback is the low

capacity to adapt to different load conditions. Regarding the geometry, the capillary tube can be straight or coiled, and depending if a heat transfer is desired or not, it can be categorized as adiabatic or diabatic. Despite being a simple component, the flow inside the capillary tube is quite complex, due to the simultaneous pressure drop and refrigerant phase-change.

Different thermodynamic states for the refrigerant fluid can occur at the inlet of the capillary tube, namely: supercritical, transcritical, subcooled liquid, saturated liquid and two-phase fluid. Figure 2.5 shows a representation of the refrigerant flow through a capillary tube in a broadest case of inlet condition (e.g. transcritical CO<sub>2</sub> system). Initially (Point 1), the fluid flows in a supercritical state up to Point 2, where, right after, the temperature is below the critical temperature, but the pressure is still above the critical pressure, reaching the transcritical state. At Point 3 begins the subcooled liquid region, remaining up to Point 4, when the saturation pressure is reached. At this point, the liquid refrigerant should start flashing to vapor. However, the vaporization is delayed and the refrigerant remains as superheated liquid up to somewhere down (Point 5). This non-equilibrium condition, when the refrigerant does not evaporate at the saturation pressure, is called metastability (PRAJAPATI ET AL., 2014). At Point 5, the vaporization takes place, but up to Point 6 the flow is still at non-equilibrium state due to the existence of superheated liquid. Finally, from Point 6 and on, the flow reaches the two-phase thermodynamic equilibrium state up to the outlet of the capillary tube. Besides metastability, the “choked” flow can also occur. By decreasing the outlet pressure, the refrigerant mass flow rate increases up to a limit, remaining constant for further pressure reductions. In this case, there will exist a sharp gradient pressure between the outlet of the capillary tube and the inlet of the evaporator (ZAREH ET AL., 2014).

Once the capillary tube is installed, it is not possible to modify or to regulate it and, therefore, the proper sizing before installation is essential to the system performance. In this sense, many researches, comprising experimental and theoretical studies, have been made to study the refrigerant flow characteristics inside the capillary tubes. Different strategies are used to depict the throttling process, spanning from numerical models to algebraic solutions and dimensionless correlations.



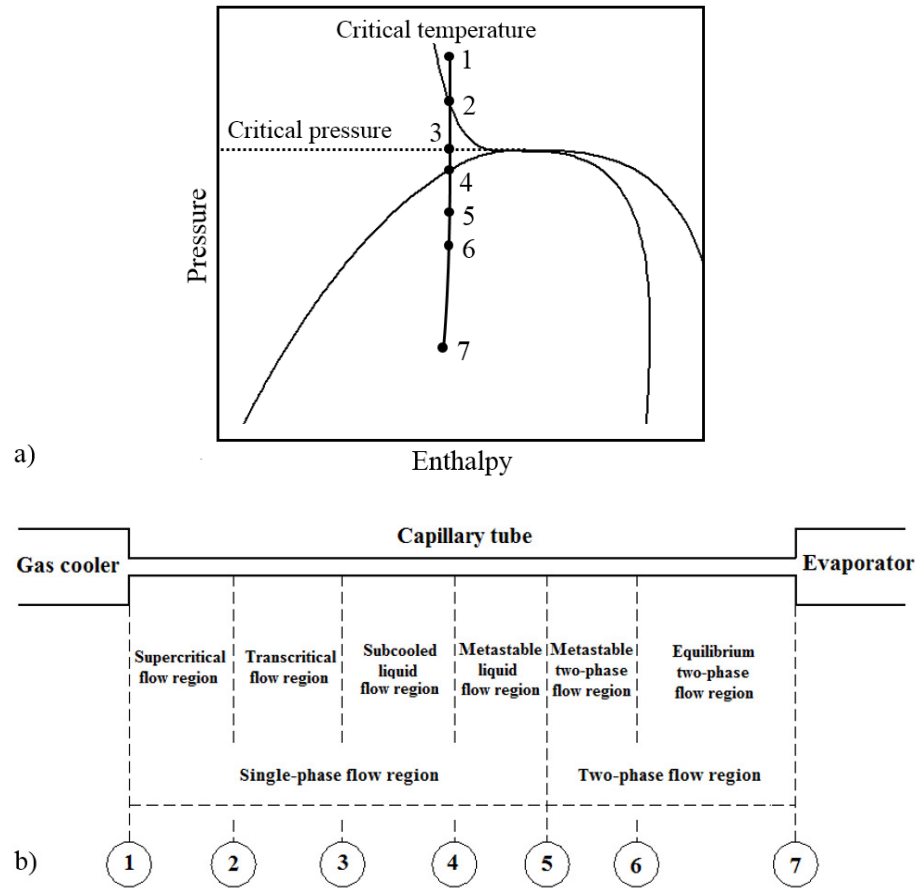


Figure 2.5: Schematic representation of the refrigerant flow through a capillary tube: a) p-h diagram; b) regions over the capillary length.

### 2.4.1 Numerical models

The numerical models are one of the most popular methods used by researchers for analyzing and designing capillary tubes, due to its general mechanism and acceptable precision (YANG AND WANG, 2008). However, they are time-consuming and require some programming skills (CECCHINATO ET AL., 2009). Finite differences or finite volumes methods are the commonly approaches employed to solve the set of mass and energy conservation equations, and momentum equation. These models can be less or more complex, depending if the two-phase are considered as homogeneous (no slip between phases) or separated (different velocities between phases) and if the metastability is regarded or not. The case considering homogeneous flow and neglecting the metastable phenomenon is generally called homogeneous equilibrium model (HEM).

Zareh et al. (2014) numerically analyzed the refrigerant flow through straight and coiled capillary tubes. They proposed a drift flux model neglecting the metastability phenomenon. To

validate the model, numerical simulations and experimental data from the literature, as well as own experiments with R134a, R12, and R22, were used for comparison. A 5.5% maximum deviation was reported between the model and the experimental results, including own and literature data. Under the same conditions and capillary tube length, the mass flow rate through a 40 mm diameter coiled capillary tube is 11% less than a straight one. For the same mass flow rate, the helical length is reduced about 14% compared to the straight length.

Wang et al. (2012) numerically studied the flow characteristics of CO<sub>2</sub> through an adiabatic coiled capillary tube in a transcritical system. They developed a separated flow model considering the metastability phenomenon, but also investigated the HEM. To verify the model, comparisons were made with experimental data for CO<sub>2</sub> in straight capillary tubes and R22 in coiled capillary tubes. The model predicted 97% of the CO<sub>2</sub> data within a  $\pm 15\%$  error band. Three different friction factors were tested and, according to them, the M&N modified is the most suitable for CO<sub>2</sub>. Considering the capillary tube inner diameter of 0.64 mm, length of 2.0 m, evaporating temperature of -10°C, capillary tube inlet temperature of 35°C and capillary tube inlet pressure of 8 MPa, the authors found that the refrigerant mass flow rate increased about 7% when the coil diameter changed from 40 mm to 600 mm. This effect is larger with higher capillary tube inlet pressures. Besides, the authors found that the length proportion of the metastable flow region to the total capillary tube length is small, unless the capillary tube inlet pressure is low enough. Therefore, nearly there is no difference in the capillary tube length when the model neglects the metastable flow.

Agrawal and Bhattacharyya (2013) also presented a numerical model to study adiabatic coiled capillary tubes in transcritical CO<sub>2</sub> systems. They developed a HEM and investigated the effect of the coil diameter in the mass flow rate. Again, as no experimental data were available for coiled capillary tubes in transcritical CO<sub>2</sub> systems, the authors adapted and validated the model with experimental data for coiled capillary tubes with R22. The results showed that the reduction on mass flow rate in coiled capillary tubes, compared to straight ones, is more pronounced for CO<sub>2</sub> than for R22, due to the higher frictional pressure drop.

Jadhav and Agrawal (2019) numerically compared straight and spiral adiabatic capillary tubes in transcritical CO<sub>2</sub> cycle and in subcritical R22 cycle. They proposed a HEM and validated it with experimental data collected in the literature for straight capillary tubes with carbon dioxide and R22, while for spiral capillary tubes only data for R22 was available, but the validation was

extended to CO<sub>2</sub>. The results confirmed the mass flow rate reduction for the spiral capillary tubes, when compared to the straight one, due to the additional pressure drop caused by the secondary flow.

#### 2.4.2 Algebraic solutions

Once the numerical models are complex and a total algebraic and explicit description for the flow through the capillary tube is not possible, approximate analytical solutions were developed. They are able to balance the generality of numerical models with the simplicity of empirical correlations (CECCHINATO ET AL., 2009). The HEM is, generally, adopted. However, it could lead to an underestimated mass flow rate prediction (ZHANG AND DING, 2004). This occurs because neglecting the flash delay, the phase-change will start earlier and, then, the two-phase region will become larger, increasing the pressure drop. According to Li et al. (1990), larger capillary tube diameters lead to lower under pressures of vaporization. Besides, larger refrigerant mass flow rates lead to larger under pressures of vaporization.

This approach was first introduced by Yilmaz and Ünal (1996), whose equation for straight capillary tubes is valid for all refrigerants. Their solution for the capillary tube length can be seen in Eq. 2.8 and 2.9.

$$L_{tp} = \frac{2d}{f} \left( \ln \left( \frac{p_{out}/p_r}{k + (1-k)p_{out}/p_r} \right) - \frac{1}{\frac{v_r G^2}{p_r} (1-k)} \left\{ \frac{p_{out}}{p_r} - 1 - \frac{k}{1-k} \ln[k + (1-k)p_{out}/p_r] \right\} \right) \quad (2.8)$$

$$k = 2.62 * 10^5 (p_r^{-0.75}) \quad (2.9)$$

where  $L$  is the capillary tube length,  $d$  is the capillary inner diameter,  $f$  is the friction factor,  $p$  is pressure,  $v$  is the specific volume,  $G$  is the mass flux; the subscript  $r$  stands for the reference point – calculated at the flash point,  $tp$  is two-phase, and  $out$  is capillary tube outlet. The parameter  $k$  is related to the specific volume. They compared the predictions with experimental mass flow rate data for R12, R22, R114, R134a, R600a, and found a maximum deviation of +19.17% for R134a.

Hermes et al. (2009) developed an algebraic equation to solve the transcritical CO<sub>2</sub> flow through adiabatic straight capillary tubes. They adapted the methodology presented by Yilmaz and Ünal to account for the properties variation in the supercritical region. Their solution is shown in Eq. 2.10.

$$G = \sqrt{\frac{f_{tp} \left[ \frac{p_{in} - p_r}{t} + \frac{u}{t^2} \ln \left( \frac{v_r p_r}{v_{in} p_{in}} \right) \right] + f_{sp} \left[ \frac{p_r - p_{out}}{a} + \frac{b}{a^2} \ln \left( \frac{v_{out} p_{out}}{v_r p_r} \right) \right]}{\frac{f_{sp} f_{tp} L}{2d} + f_{tp} \ln \left( \frac{v_r}{v_{in}} \right) + f_{sp} \ln \left( \frac{v_{out}}{v_r} \right)}} \quad (2.10)$$

where the subscripts *sp* and *in* means single-phase and capillary tube inlet, respectively. The parameters *a*, *b*, *t* and *u* are related to the specific volume and they will be presented in Section 3.1. The authors validated the proposed solution with experimental data and found 94% of the predicted mass flow rates within a ±10% error band.

Later, Hermes et al. (2010) developed a generic semi-empirical algebraic equation, derived from the approximate analytical solution and considering some simplifications introduced by Yilmaz and Ünal (1996). Their solution includes one parameter ( $\Phi$ ) that can be calculated based on the friction factor or can be experimentally adjusted. The proposed equation is seen in Eq. 2.11.

$$\dot{m} = \Phi \sqrt{\frac{d^5}{L} \left[ \frac{p_{in} - p_r}{v_r} + \frac{p_r - p_{out}}{a} + \frac{b}{a^2} \ln \left( \frac{a p_{out} + b}{a p_r + b} \right) \right]} \quad (2.11)$$

where  $\dot{m}$  is the mass flow rate. They compared the predictions with experimental mass flow rates for R134a and R600a, and found 89.1% of data within a ±10% error band.

### 2.4.3 Dimensionless correlations

The dimensionless correlations can be derived from a combination of a physical and experimental background (semi-empirical) or from a totally experimental (empirical) method and in its majority are developed using the dimensional analyses described by the Buckingham-Pi-Theorem. To form the correlations, the dimensionless groups are combined and can be fitted to the experimental data by two principal means: multiple regression (power-law) or artificial neural networks (ANN). Tables 2.4 and 2.5 present some correlations for the mass flow rate prediction in adiabatic straight and adiabatic coiled capillary tubes, respectively. Table 2.6

presents the dimensionless parameters groups used in Eq. 2.12 to 2.22, where  $D$  is the coil diameter of the capillary tube,  $\rho$  is density,  $\mu$  is the dynamic viscosity,  $\varepsilon$  is the capillary tube roughness,  $\sigma$  is the surface tension,  $x$  is the quality,  $T$  is temperature,  $\Delta T'$  is the subcooling,  $h$  is enthalpy,  $c_p$  is the specific heat at constant pressure and the subscripts are:  $f$  for saturated liquid,  $g$  for saturated vapor,  $cond$  for condensing and  $crit$  for critical. The other parameters are the same as previously mentioned. The recommended ranges for utilization or the experimental parameters ranges used to derive the correlations, as well as the variables not listed in Table 2.6 and presented in Tables 2.4 and 2.5 can be seen in the respective original papers.

Table 2.4: Correlations for mass flow rate prediction in adiabatic straight capillary tubes.

Author	Equation	Refrigerant	Eq. number
Melo et al. (1999)	$\pi_1 = 0.195\pi_2^{0.448}\pi_3^{-0.528}\pi_4^{0.164}$	R12, R134a, R600a	(2.12)
Yang and Wang (2008)	$\pi_1 = 4257.9\pi_2^{0.7338}\pi_3^{-0.2220}\pi_4^{0.4671}\pi_5^{0.1226}\pi_6^{1.5956}\pi_7^{0.7061}$	R12, R22, R134a, R290, R600a, R410A, R407C, R404A	(2.13)
Da Silva et al. (2009)	$\tilde{m} = 11.47 + 0.14\tilde{p}_e - 0.09\tilde{T}_e - 0.10\tilde{L} + \tilde{D}[0.35 + 0.01(0.25\tilde{D} + 0.22\tilde{p}_e - 0.10\tilde{T}_e - 0.15\tilde{L})]$	CO2	(2.14)
Yang and Zhang (2009)	$\pi_1 = \sum_{j=1}^3 \frac{w_{1,j}}{1 + \exp[-(\sum_{i=1}^4 u_{j,i} \pi_{i+1} + b_{1,j})]} + b_{2,1}$	R12, R22, R134a, R404A, R407C, R410A, R600a, CO2	(2.15)
Vins and Vacek (2009)	$\bar{\pi}_8 = -\frac{3.8314}{1 + e^{-n_1}} + \frac{0.7616}{1 + e^{-n_2}} + 2.3454$	R218	(2.16)
Yang and Zhang (2014)	$\pi_1 = \frac{1 - 3.6622463\pi_2^{-1.4311445}}{-12.377615 - 4.4141877\pi_4\pi_5^{-0.2874146}\pi_3^{-0.0662179}}$	R12, R22, R134a, R407C, R410A, R600a, CO2	(2.17)
Rasti and Jeong (2018)	$\pi_8 = 150.26\pi_1^{-0.5708}\pi_2^{-1.4636}\pi_4^{1.953}\pi_5^{0.6436}\pi_6^{1.4181}$	R22, R134a, R600a	(2.18)
Rocha et al. (2019)	$\pi_1 = \pi_2^{-0.4152}\pi_3^{0.0961}\pi_4^{-0.5450}\pi_5^{0.1601}$	CO2	(2.19)

Table 2.5: Correlations for mass flow rate prediction in adiabatic coiled capillary tubes.

Author	Equation	Refrigerant	Eq. number
Dubba and Kumar (2018b)	$\pi_1 = 0.124\pi_2^{2.33}\pi_3^{0.55}\pi_5^{-0.16}\pi_6^{0.148}\pi_7^{0.16}$	R600a	(2.20)
Gill and Jagdev (2018)	$\pi_5 = 0.07029\pi_1^{0.0675}\pi_2^{0.5072}\pi_3^{-0.0165}\pi_4^{-0.2879}$	R134a/LPG	(2.21)
Deodhar et al. (2015)	$\pi_8 = 1.313 \times 10^{-3} \pi_1^{-0.087}\pi_2^{0.188}\pi_3^{-0.412}\pi_4^{-0.834}\pi_5^{0.199}\pi_6^{-0.368}\pi_7^{0.992}\pi_9^{0.0578}$	R134a	(2.22)

Table 2.6: Dimensionless Pi groups used in the correlations.

Authors	Melo et al. (1999)	Yang and Wang (2008)	Yang and Zhang (2009, 2014) Rocha et al. (2019)	Vins and Vacek (2009)	Rasti and Jeong (2018)	Dubba and Kumar (2018b)	Gill and Jagdev (2018)	Deodhar et al. (2015)
Eq. number	(2.12)	(2.13)	(2.15), (2.17), (2.19)	(2.16)	(2.18)	(2.20)	(2.21)	(2.22)
$\pi_1$	$\frac{\dot{m}}{d\mu_f}$	$\frac{1.273\dot{m}}{d^2\sqrt{p_{in}\rho_{in}}}$	$\frac{1.273\dot{m}}{d^2\sqrt{p_{in}\rho_{in}}}$	$\frac{p_{in} - p_r}{p_{crit}}$	$\frac{L}{d}$	$\frac{\dot{m}}{L\mu_f}$	$\frac{d^2\rho_f^2c_p\Delta T'}{\mu_f^2}$	$\frac{p_{in} - p_r}{p_{crit}}$
$\pi_2$	$\frac{d^2\rho_f p_r}{\mu_f^2}$	$\frac{p_{in}}{p_r}$	$\frac{p_r}{p_{in}}$	$\frac{T_{in} - T_{cond}}{T_{crit}}$	$\frac{d^2h_{fg}}{v_f^2\mu_f^2}$	$\frac{d}{L}$	$\frac{d^2\rho_f p_{in}}{\mu_f^2}$	$\frac{\Delta T'}{T_{crit}}$
$\pi_3$	$\frac{L}{d}$	$\frac{\rho_f}{\rho_g}$	$\frac{\rho_g}{\rho_f}$	$\frac{L}{d}$	$\frac{d\sigma}{v_f\mu_f^2}$	$\frac{L^2\rho p_{in}}{\mu_f^2}$	$\frac{D}{d}$	$\frac{L}{d}$
$\pi_4$	$\frac{d^2\rho_f^2c_p\Delta T'}{\mu_f^2}$	$\frac{d}{L}$	$\frac{L}{d}$	$\frac{\rho_f}{\rho_g}$	$\frac{d^2p_{in}}{v_f\mu_f^2}$	$\frac{\varepsilon}{L}$	$\frac{L}{d}$	$\frac{\rho_f}{\rho_g}$
$\pi_5$	$\frac{\varepsilon}{d}$	$\frac{d\sqrt{p_{in}\rho_{in}}}{\mu_{in}}$	$\frac{d\sqrt{p_{in}\rho_{in}}}{\mu_{in}}$	$\frac{\mu_f - \mu_g}{\mu_g}$	$1 + \frac{(h_{in} - h_f)}{h_{fg}}$	$\frac{L^2h\rho^2}{\mu_f^2}$	$\frac{\dot{m}}{d\mu_f}$	$\frac{\mu_f - \mu_g}{\mu_g}$
$\pi_6$	-	$1 - x_{in}$	-	$\frac{\sigma}{p_{in}d}$	$\frac{v_g}{v_f}$	$\frac{L^2\rho^2c_p\Delta T'}{\mu_f^2}$	-	$\frac{\sigma}{p_{in}d}$
$\pi_7$	-	$1 + \frac{\Delta T'}{T_{cond}}$	-	$\frac{\rho_f(h_g - h_f)}{p_r}$	$\frac{\mu_f - \mu_g}{\mu_g}$	$\frac{d}{L}$	-	$\frac{\rho_f(h_g - h_f)}{p_r}$
$\pi_8$	-	-	-	$\frac{\dot{m}}{d^2\sqrt{p_{in}\rho_f}}$	$\frac{\dot{m}}{d\mu_f}$	-	-	$\frac{\dot{m}}{d^2\sqrt{p_{in}\rho_f}}$
$\pi_9$	-	-	-	-	-	-	-	$\frac{0.7452 D}{d}$

#### 2.4.4 Experimental studies

Da Silva et al. (2009) experimentally and numerically studied adiabatic capillary tubes in a transcritical CO<sub>2</sub> refrigeration cycle. A theoretical model was developed, based on mass and energy conservation equations, and momentum equation, considering a homogeneous one-dimensional flow, and neglecting the metastable flow. The equipment was designed to operate with pressures up to 13 MPa and the main components are: two 1.75 cm<sup>3</sup> reciprocating compressors, a gas cooler, a straight and horizontal capillary tube and a thermostatic bath. Based on the factorial design, the authors proposed an empirical dimensionless correlation, Eq. 2.14, together with the operational conditions and the capillary characteristics. The results confirmed that the internal diameter is the factor of major impact on the mass flow rate. The empirical correlation and the theoretical model predicted 97% and 95% of the data points, respectively, within a  $\pm 10\%$  error band.

Zhao et al. (2014) proposed a stepped capillary tube to replace the capillary tube assembly used in residential heat pump systems that operate at heating and cooling modes. The main claim of their work is to reduce the cost of the expansion device by eliminating the check-valve used in the capillary tube assembly. Once the heat thermal load of the heating mode is usually smaller than that of the cooling mode, a specific mass flow rate is supplied by these throttling devices in each operating mode. The authors developed a model able to predict the mass flow rate and the length of a stepped capillary tube, considering one-dimensional homogeneous adiabatic flow and neglecting the metastable flow. The model was experimentally validated and the maximum mass flow rate deviation between the predicted and the experimental results was 5.24%. Finally, they verified the performance of a residential heat pump system using the original capillary tube assembly and using the proposed stepped capillary tube, after the replacement. The working fluid was the R22 and the mass flow rate at cooling and heating modes were 85.8 kg/h and 60.7 kg/h, respectively. The authors concluded that the system with the stepped capillary tube achieved the same performance as using the capillary tube assembly. Besides, the total cost of the stepped capillary tube was less than half cost of the original capillary tube assembly.

Schenk and Oellrich (2014) experimentally studied the refrigerant flow of R600a through adiabatic capillary tubes. The main aim of their work was to extend the published database for the isobutane with lower mass flow rates and check the validity of existing correlations. The main workbench components are: a 9 cm<sup>3</sup> hermetic variable velocity compressor, a condenser



with an electric heater to regulate the inlet air temperature, a sub cooler, an electric pre-heater, a capillary tube and an evaporator equipped with an electric heater. The experiments were planning based on the Two-level Factorial Design method. The mass flow rate ranged from 0.65 kg/h to 2.0 kg/h. The outlet pressure of the capillary tube was not considered in the design of experiments, once the mass flow rate does not change below a certain outlet pressure, indicating the occurrence of choked flow. In all the tests, the outlet pressure was kept below the critical pressure for the choked flow occurrence. Their experimental data and that published by Melo et al. (1999), for R600a, were compared with the results given by the equation of Hermes et al. (2010). They found a 94% of agreement within an error band of 10%, including both datasets.

Dubba and Kumar (2018a) experimentally investigated the refrigerant flow of R600a through diabatic capillary tubes, with sub-cooled conditions. The capillary tubes were designed to exchange heat with the compressor suction line, in a concentric configuration. Straight and coiled shapes were tested. The experimental apparatus is mainly composed by an open type compressor, a condenser, a sub-cooler, a pre-heater, a needle-valve, a capillary tube and an evaporator (thermostatic bath). The capillary diameters and lengths for all capillary tubes varied from 1.12 mm to 1.52 mm and from 2.8 m to 4.6 m, respectively. The coil diameters for the helical capillary tubes were 60 mm and 80 mm. The results indicated an increase in the mass flow rate with the increase in the degree of subcooling. With the same diameters and lengths, lower mass flow rate was achieved for the coiled capillary tube compared with the straight capillary tube. Lastly, they proposed a semi empirical correlation to predict the mass flow rate for straight and coiled diabatic capillary tubes. This correlation predicted 94% of the experimental data within a  $\pm 20\%$  error band.

In a similar work, Dubba and Kumar (2018b) experimentally investigated the flow of R600a through adiabatic capillary tubes. The equipment is the same as presented in Dubba and Kumar (2018a), except for the capillary tube. However, the capillary dimensions (diameter and length) are the same and the coil diameters are 40 mm, 60mm and 80mm. As already presented, the mass flow rate is lower in coiled than in straight capillary tubes, due to the existence of secondary flow. They proposed a semi empirical correlation, Eq. 2.20, to predict the mass flow rate for straight and coiled adiabatic capillary tubes. This correlation predicted 98% of the experimental data within a  $\pm 20\%$  error band.

Bengtsson and Berguel (2016) experimentally evaluated the possibility of using a capillary tube, as an alternative to automatic expansion devices, in a heat pump dishwasher during the transient heating period. The experimental setup is based on a conventional dishwasher, and the R600a heat pump system comprises a 7.2 cm<sup>3</sup> compressor, an evaporator immersed in a 7 liters water tank, the capillary tube and a concentric tubes condenser. Five capillaries, with lengths of 0.25, 0.39, 0.68, 1.46 and 1.96 m were used, having all of them the same inner diameter of 0.9 mm. In all the experiments, the dishwasher was heated for 60 minutes with a starting temperature of 22°C. The results indicated that it is possible to use the capillary tube during the transient heating process, once there was a slightly change in electricity consumption by using different capillary tube lengths. The authors argue that adopting a variable expansion device will probably not decrease the electricity consumption significantly.

Gill and Jagdev (2018) applied the ANN technique to predict the mass flow rate of R134a/LPG through straight and coiled adiabatic capillary tubes and also proposed a dimensionless correlation, Eq. 2.21. To check the models, a set of 144 experiments were carried out. The main workbench components are: a hermetic reciprocating compressor, an evaporator immersed in an ethylene glycol bath, a condenser, the capillary tubes, a sub-cooler and a pre-heater. The capillary tubes dimensions are: diameter of 1.12 mm, length of 3.1 m, 4.1 m, 5.1 m and 6.1 m, and coiled diameter of 60 mm, 90 mm, 120 mm. The authors statistically analyzed the dimensionless correlation and the ANN predictions, compared with the experimental results. For the dimensionless correlation and ANN model, the absolute fraction of variance was 0.961 and 0.988, the root mean square error was 0.489 kg/h and 0.275 kg/h and the absolute percentage error was 4.75% and 2.31%, respectively. The authors concluded that the dimensionless correlation showed good agreement with the experimental data. However, the ANN model predicted the mass flow rate more accurately.

## **2.5 Surface roughness and pressure drop**

The effect of surface roughness on pressure drop was identified as an important aspect in the nineteenth century by Henry Darcy, who introduced the concept of relative roughness (TAYLOR ET AL., 2006). However, the first work to quantify the effect of surface roughness on pressure drop and on the friction factor was presented by Nikuradse (1933). In his work, tubes with different diameters were roughened by coating the internal surface with a layer of sand grains of uniform and known size. The absolute surface roughness was considered equal to the sand grains diameter (DEL COL ET AL., 2013) and most of the subsequent friction factor

studies incorporated this concept. Since actual pipes do not have such a regular surface as the sand grains, it is important to understand how to estimate the surface roughness and which roughness parameter to choose among those given by the roughness measurement techniques. Briefly, the  $R_a$  is the arithmetic average distance from the absolute profile line to the mean line,  $R_q$  is the distance from the root mean square profile line to the mean line,  $R_p$  is the distance from the mean line to the highest peak, and  $R_z$  is the average distance from five highest peaks to the five lowest valleys. Some deeper studies do not recommend the  $R_a$  parameter, although it is commonly used.

Hrnjak and Tu (2007) studied the frictional pressure drop of R134a in rectangular microchannels, with different hydraulic diameters and aspect ratios, in the laminar and turbulent regimes. They reported that the  $R_a$  parameter may not be the best choice to characterize the surface roughness of microchannels.

Young et al. (2009) proposed a new equation to estimate the surface roughness ( $\varepsilon$ ) (Eq. 2.23), function of two variables: the  $R_p$  parameter, and a new one, called  $FdRa$ . To verify the proposed parameter, samples with different surface roughness were collected, and the values of  $R_a$  and  $\varepsilon_{Fp}$  were compared with previous experimental data of fluid flow. The authors concluded that the  $R_a$  parameter is not adequate to characterize surfaces for fluid flow applications, being the  $\varepsilon_{Fp}$  more representative.

$$\varepsilon = R_p + FdRa \quad (2.23)$$

Zhou and Yao (2011) studied the effect of surface roughness on laminar flow. They compared existing models with experimental data for microchannels, collected from the literature. The results showed that when the  $R_p$  parameter is used instead of  $R_a$ , the models achieved a better agreement.

Farshad et al. (2001) analyzed the surface roughness of internally coated pipes and the pressure drop due to the fluid flow. According to them, at relatively high velocities, the surface roughness becomes an important factor that affects the turbulence. Besides, they concluded that the parameter  $R_z$  is a good choice in turbulent flow.

Adams et al. (2012) experimentally studied the effect of surface roughness on fluid flow. They proposed three different correlations, function of  $R_a$ ,  $R_q$  and  $R_z$  roughness parameters, to better

estimate the roughness value, called sand-grain roughness. These correlations are seen in Eq. 2.24, 2.25 and 2.26. The authors argue that the direct measurement of a surface roughness may not be suitable for fluid flow applications. The results showed that for relatively small roughness ( $R_z$  between 1.5 and 2.5  $\mu\text{m}$ ) the corrected  $R_z$  value is the best choice among the three proposed correlations. For  $R_z$  between 4 and 5  $\mu\text{m}$ , the experimental roughness fell between the corrected  $R_a$  and  $R_z$ , while for  $R_z$  bigger than 15  $\mu\text{m}$ , the corrected  $R_a$  performed better.

$$\varepsilon = 5.863R_a \quad (2.24)$$

$$\varepsilon = 3.100R_q \quad (2.25)$$

$$\varepsilon = 0.978R_z \quad (2.26)$$

## 2.6 Concluding remarks from review

Many expressions to design a capillary tube are available in the reviewed papers. However, to the best of the author's knowledge, none of them, including dimensionless correlations and algebraic equations, was proposed to analyze a coiled capillary tube operating in a transcritical  $\text{CO}_2$  system. This motivates the development of an algebraic solution for adiabatic coiled capillary tubes, presented in section 3.1. Besides, no experimental study with focus on adiabatic coiled capillary tubes in transcritical  $\text{CO}_2$  systems were found in the open literature, reinforcing the innovative nature of this work. Regarding the surface roughness, it seems not to exist a consensus in which parameter is the most suitable for fluid flow applications. Some correlations have been published to try to estimate the sand grain roughness. One of these correlations could be a possible choice to be used with the algebraic solution proposed in this work. However, it involves a non-standardized parameter, making it difficult to be directly applied. This motivated the proposition of a correlation to estimate the surface roughness, presented in section 3.2.

The authors, in its majority, recommend and use automatic expansion valves (TEV and EEV) in SAHP. Among all the DX-SAHP reviewed papers, only Huang et al. (2019) mentioned the use of a capillary tube as the expansion device. Nevertheless, they did not focus on its influence over the system performance and give none information about the capillary tube and the refrigerant fluid used. Then, based on one of the conclusions from the work of Rabelo et al. (2019), that capillary tubes could be a reasonable choice for a DX-SAHP, this work will explore the use of a capillary tube in a DX-SAHP, operating in a transcritical  $\text{CO}_2$  cycle. This choice

could help to reduce costs and making the DX-SAHP more popular, since capillary tubes are less expensive than EEV.

### 3 METHODOLOGY

#### 3.1 Capillary tube algebraic solution

Algebraic equations and dimensionless correlations for straight capillary tubes operating in a transcritical CO<sub>2</sub> systems are available. However, the straight shape is not practical for commercial applications due to the long space required in the facility. Then, coiled capillary tubes are preferred. Once no equations or correlations for coiled capillary tubes in transcritical CO<sub>2</sub> systems were found in the open literature, to the best of the author's knowledge, an algebraic solution, based on the HEM, will be developed in this section.

The flow of refrigerants inside capillary tubes are governed by mass and energy conservation equations, and momentum equation, as seen in Eq. 3.1 to 3.3, respectively.

$$\frac{\partial \rho}{\partial t} + \nabla \cdot \rho \vec{V} \quad (3.1)$$

$$\rho \frac{\partial e}{\partial t} + p(\nabla \cdot \vec{V}) = \nabla \cdot (\lambda \nabla T) + \varphi \quad (3.2)$$

$$\rho g - \nabla p + \nabla \cdot \tau_{ij} = \rho \frac{D\vec{V}}{Dt} \quad (3.3)$$

where  $\rho$  is density,  $\vec{V}$  is the velocity vector,  $e$  is internal energy,  $p$  is pressure,  $\lambda$  is the thermal conductivity,  $T$  is temperature,  $\varphi$  is the viscous-dissipation function,  $g$  is gravity and  $\tau_{ij}$  is the viscous-stress tensor. Since an analytic and explicit description of the total throttling process is not possible (Schenk and Oellrich, 2014), the present solution assumes the following assumptions:

- one dimensional steady-state flow;
- homogeneous two-phase flow;
- metastability phenomenon neglected;
- isenthalpic throttling process;
- constant cross-section area and uniform surface roughness of the capillary tube;
- flow of pure refrigerant, i.e. absence of water, compressor oil and other impurities;

-pressure drop at the entrance and exit of the capillary tube neglected.

With such considerations, the mass and energy conservation equations can be simplified to Eq. 3.3 and 3.4, respectively. The momentum equation, as presented by Yilmaz and Ünal (1996), is shown by Eq. 3.5a.

$$\frac{dG}{dL} = 0 \quad (3.3)$$

$$\frac{dh}{dL} = 0 \quad (3.4)$$

$$-\frac{dp}{dL} = G^2 \frac{dv}{dL} + \frac{fvG^2}{2d} \quad (3.5a)$$

where  $L$  is the capillary tube length,  $h$  is specific enthalpy,  $d$  is the capillary inner diameter,  $f$  is Darcy's friction factor,  $v$  is the specific volume and  $G$  is the mass flux. Rewriting Eq. 3.5a for the differential length instead of the pressure drop, Eq. 3.5b is found:

$$dL = \frac{-2d}{fvG^2} \left( 1 + G^2 \frac{dv}{dp} \right) dp \quad (3.5b)$$

To solve Eq. 3.5a or 3.5b, it is necessary a function between  $v$  and  $p$ . The relation presented by Yilmaz and Ünal (1996) for the two-phase region in an isenthalpic process will be adopted, as seen in Eq. 3.6. Besides, the definition proposed by Hermes et al. (2009) will be followed, according to Eq. 3.7 to 3.9.

$$v = v_r \left[ 1 + k_{tp} \left( \frac{p_r}{p} - 1 \right) \right] \quad (3.6)$$

$$v = a + \frac{b}{p} \quad (3.7)$$

$$a = v_r(1 - k_{tp}) \quad (3.8)$$

$$b = v_r p_r k_{tp} \quad (3.9)$$

where the subscripts  $r$  stands for the flash point and  $tp$  stands for two-phase region. Replacing Eq. 3.9 and 3.8 onto Eq. 3.7 leads to Eq. 3.6. The parameter  $k$  is dependent on the refrigerant properties at the flash point and two different sources will be evaluated in the present algebraic solution. The first is the  $k_{tp}$  proposed by Hermes et al. (2009), seen in Eq. 3.10. The second is

that of Bhattacharyya et al. (2010), Eq. 3.11a, who also proposed a  $j$  factor in the two-phase specific volume, to account for the possibility of the throttling process to occur at the right side of the critical point (see Fig. 3.1b). This factor must be multiplied by  $k_{tp}$  in Eq. 3.8 and 3.9, and is seen in Eq. 3.11b.

$$k_{tp} = 148,000p_r^{-0.71} \quad (3.10)$$

$$k_{tp} = 2.134e^{-\left(\frac{p_r-63.16}{17.55}\right)^2} - 0.3444e^{-\left(\frac{p_r-74.38}{3.667}\right)^2} + 0.08306e^{-\left(\frac{p_r-69.99}{3.155}\right)^2} \quad (3.11a)$$

$$j = \frac{v_{out} - v_r}{v_r k_{tp} \left(\frac{p_r}{p_{out}} - 1\right)} \quad (3.11b)$$

For the single-phase region, assuming to be far from the critical point, Yilmaz and Ünal (1996) considered the specific volume constant. However, this cannot be applied for transcritical CO<sub>2</sub> flow due to the significant variation of the thermophysical properties in the supercritical region. Then, the specific volume definition proposed by Yilmaz and Ünal (1996) for the two-phase region will be extended to the single-phase region, Eq. 3.12 to 3.14, as introduced by Hermes et al. (2009) and also considered by Bhattacharyya et al. (2010). The parameters  $k_{sp}$  given by the first and the second authors can be seen in Eq. 3.15 and 3.16, respectively.

$$v = t + \frac{u}{p} \quad (3.12)$$

$$t = v_r(1 - k_{sp}) \quad (3.13)$$

$$u = v_r p_r k_{sp} \quad (3.14)$$

$$k_{sp} = [390.5 - 24.56 \ln(p_r)]^{-1} \quad (3.15)$$

$$k_{sp} = 3.335e^{-\left(\frac{p_r-84.78}{6.874}\right)^2} - 0.02763e^{-\left(\frac{p_r-73.21}{1.779}\right)^2} + 0.001205e^{-\left(\frac{p_r-71.9}{0.3564}\right)^2} + 0.2712e^{-\left(\frac{p_r-74.13}{15.42}\right)^2} \quad (3.16)$$

where the subscript  $sp$  stands for the single-phase region. The pressure unit in Eq. 3.16 and 3.11a is bar, while in Eq. 3.15 and 3.10 is Pa. Since the specific volume is already defined in terms of pressure, Eq. 3.5b can be integrated to give the capillary tube length. This will be done in two integrating limits over the isenthalpic expansion: one for the two-phase region and other for the single-phase region, as seen in Figure 3.1.



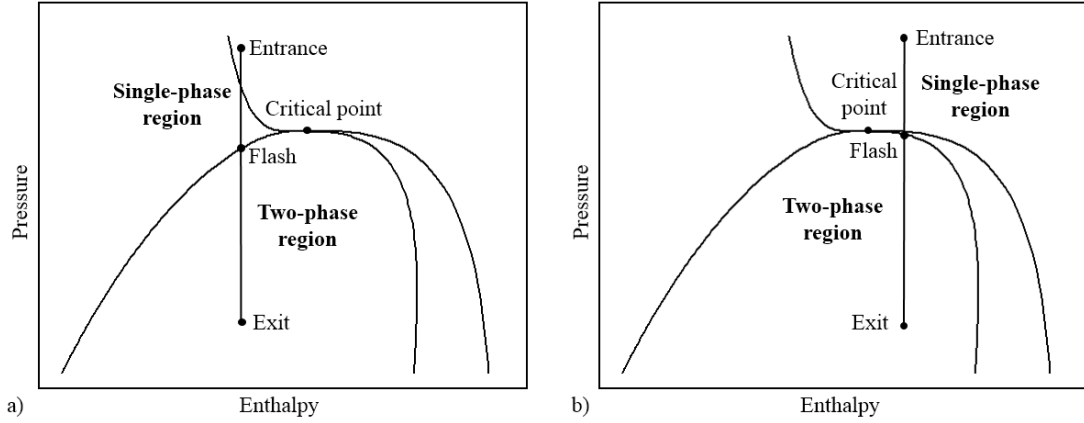


Figure 3.1: ph diagram with the integrating limits: a) left of the critical point; b) right of the critical point.

Substituting Eq.3.7 and its derivative into Eq. 3.5b, integrating from the flash point up to the exit point, and rearranging, the capillary tube length for the two-phase region is given by Eq. 3.17.

$$L_{tp} = \frac{2d}{f_{tp}G^2} \left[ \frac{p_r - p_{out}}{a} + \frac{b}{a^2} \ln \left( \frac{ap_{out} + b}{ap_r + b} \right) - G^2 \ln \left( \frac{v_{out}}{v_r} \right) \right] \quad (3.17)$$

where the subscript *out* stands for the outlet point of the capillary tube. For the single-phase region, Eq.3.12 and its derivative are substituted into Eq. 3.5b and integrated from the inlet point up to the flash point. After rearranging, the single-phase length is given by Eq. 3.18.

$$L_{sp} = \frac{2d}{f_{sp}G^2} \left[ \frac{p_{in} - p_r}{t} + \frac{u}{t^2} \ln \left( \frac{tp_r + u}{tp_{in} + u} \right) - G^2 \ln \left( \frac{v_r}{v_{in}} \right) \right] \quad (3.18)$$

where the subscript *in* stands for the inlet point of the capillary tube. Finally, the total capillary tube length is given by Eq. 3.19.

$$L = L_{tp} + L_{sp} \quad (3.19)$$

At this point, the friction factor must be specified. Here lays the fundamental difference in straight and coiled capillary tube solutions, once the same friction factor cannot be applied for both cases. However, to evaluate the coiled friction factor, the straight one must be previously calculated. In the present solution, Churchill's (1977) friction factor for straight capillary tubes, Eq. 3.20a-c, were adopted for the single and two-phase regions, except in one case, that will be pointed out.

$$f_s = 8 \left[ \left( \frac{8}{Re} \right)^{12} + \frac{1}{(A+B)^{3/2}} \right]^{1/12} \quad (3.20a)$$

$$A = \left[ 2.457 \ln \left( \frac{1}{\left( \frac{7}{Re} \right)^{0.9} + \frac{0.27\epsilon}{d}} \right) \right]^{16} \quad (3.20b)$$

$$B = \left( \frac{37530}{Re} \right)^{16} \quad (3.20c)$$

where  $Re$  is the Reynolds number, given by Eq. 3.21,  $\epsilon$  is capillary tube surface roughness and the subscript  $s$  stands for straight capillary tube.

$$Re = \frac{Gd}{\mu} = \frac{4\dot{m}}{\pi d \mu} \quad (3.21)$$

where  $\mu$  is the dynamic viscosity and  $\dot{m}$  is the mass flow rate. For the single-phase region,  $\mu$  is the average of the inlet and flash point viscosities, Eq. 3.22, while for the two-phase region,  $\mu$  is calculate by Eq. 3.23 (YILMAZ AND ÜNAL, 1996).

$$\mu_{sp} = \frac{\mu_{in} + \mu_r}{2} \quad (3.22)$$

$$\mu_{tp} = \frac{8}{7} \mu_r \left[ \frac{1 - (p_{out}/p_r)^{7/8}}{1 - (p_{out}/p_r)} \right] \quad (3.23)$$

Three friction factors for coiled capillary tubes will be presented and investigated. The same friction factor will be applied for the single and two-phase regions. The first is the Schmidt friction factor, as cited by Chingulpitak and Wongwises (2010) and presented by Eq. 3.24a-b.

$$\frac{f_c}{f_s} = 1 + 0.14 Re^{x'} \quad (3.24a)$$

$$x' = \left[ \frac{1 - 0.0644}{(D-d)^{0.312}} \right] / \left( \frac{D}{d} \right)^{0.97} \quad (3.24b)$$

where  $D$  is the coil diameter of the capillary tube and the subscript  $c$  stands for coiled capillary tube. The second friction factor is that presented by Mori and Nakayama (1967) (M&N), seen is Eq. 3.25a-c.

$$f_c \sqrt{\frac{D}{d}} = \frac{\theta}{\left[ \text{Re} \left( \frac{d}{D} \right)^{m/2} \right]^{\frac{1}{m+1}}} \left\{ 1 + \frac{\psi}{\left[ \text{Re} \left( \frac{d}{D} \right)^{m/2} \right]^{\frac{1}{m+1}}} \right\} \quad (3.25a)$$

$$\log(\theta) = \frac{1}{m+1} \left\langle \frac{1}{4} \{-3\log(2m+1) + (16m-7)\log(2m-1) - (8m-3)[\log(m) + \log(4m-1)] + \log(6m-1) + 9\log(2)\} + m\log(\alpha) \right\rangle \quad (3.25b)$$

$$\log(\psi) = \frac{1}{m+1} \left\langle \frac{1}{4} \{3m\log(2m+1) - (15m+4)\log(m) + (19m-4)\log(2m-1) - (7m-4)\log(4m-1) - m\log(6m-1) - 9m\log(2)\} + m\log(\alpha) \right\rangle \quad (3.25c)$$

where  $m$  and  $\alpha$  are the coefficients of Blasius' correlation, Eq. 3.26a, for a straight tube.

$$f_s = \alpha \text{Re}^{-1/m} \quad (3.26a)$$

According to Mori and Nakayama (1967),  $m$  and  $\alpha$  assume the values as presented in Eq. 3.26b and 3.26c.

$$\text{If } \text{Re} < 100,000: \alpha = 0.316 \text{ and } m = 4 \quad (3.26b)$$

$$\text{If } \text{Re} > 100,000: \alpha = 0.184 \text{ and } m = 5 \quad (3.26c)$$

For the M&N correlation, the coiled friction factor incorporates the Blasius' friction factor for straight tubes. One implication is that the tube roughness is not considered in this solution. To account for this matter, a M&N modified friction factor, called C- M&N, will also be evaluated, as introduced in Zhou and Zhang (2006). This modification consists in the following 3 steps:

1 – To calculate  $f_s$  according to Churchill's correlation, Eq. 3.20;

2 – To introduce  $f_s$  from step 1 and the value of  $m$  (4 or 5 according to  $Re$ ) in Blasius' correlation, Eq. 3.26. Then, calculate  $\alpha$ ;

3 – With the calculated  $\alpha$  and the corresponding  $m$ , to calculate the coiled friction factor by M&N correlation, Eq. 3.25.

### 3.2 Capillary tube sizing and assembling

To size the adiabatic coiled capillary tubes, Eq. 3.19 was used. It was chosen the  $k$  parameters provided by Bhattacharyya et al. (2010), Eq.3.11a and 3.16, without the  $j$  factor. Besides, the C- M&N friction factor was adopted, assuming a surface roughness of 1.5  $\mu\text{m}$ . Regarding the operational conditions, the works of Ruas (2019) and Paulino (2019) was used as reference. The capillary tube inlet and outlet pressures, the refrigerant temperature at the gas cooler outlet and the refrigerant mass flow rate were taken for high and low solar radiation conditions. Then, two capillary tubes with different diameters and lengths were sized to a same “medium” solar radiation condition.

Once transcritical CO<sub>2</sub> systems present an optimal operating point and the high pressure is one of the most important aspects to design a capillary tube, the optimal high pressure was investigated. Tab. 3.1 presents the optimal pressures calculated according to Eq. 2.1 to 2.7 (Tab. 2.3).

Table 3.1: Optimal pressures presented by different correlations.

Source	T evap [°C]	T gc out [°C]	P opt [bar]
Cecchinato and Corradi (2011)	-	30	88.33
Kauf (1999)	-	30	85.54
Qi et al. (2013)	-	30	75.51
Song et al. (2017)	-	30	73.67
Chen and Gu (2005)	-	30	73.60
Liao et al. (2000)	6.27	30	73.44
Yang et al. (2015)	6.27	30	73.15

From Table 3.1, it can be seen two ranges for the optimal pressure: one of 85-88 bar and other of 73-75 bar. The selected operational conditions of Ruas (2019) and Paulino (2019) matches the 85-88 bar. The evaporating temperature of 6.27°C corresponds to the evaporating pressure of 41 bar. Table 3.2 summarizes the operational conditions and the corresponding capillary tube dimensions.

Table 3.2: Capillary tube dimensions and corresponding operational conditions.

Number	Nominal d [in]	Nominal d [mm]	L [mm]	P in [bar]	T in [°C]	P out [bar]	$\dot{m}$ [kg/h]
1	0.042	1.07	2966	85	30	41	26.30
4*	0.036	0.91	1339	85	30	41	26.30

\*capillary tubes 2, 3, and 5 were used for sample preparation and to be spare parts. They were not used in the experiments.

The mass flow rate corresponding to the “medium” solar radiation condition would be 26.00 kg/h. However, the required length for the capillary tube number 1 would be 3035 mm, above the 3000 mm length that is commercially available. Besides, it is still necessary to use part of this length to make some samples. Therefore, 26.30 kg/h of mass flow rate was chosen to design both tubes.

### 3.2.1 Geometric characterization

Several authors (MELO ET AL., 1999; DA SILVA ET AL., 2009; AGRAWAL ET AL., 2011; SCHENK AND OELLRICH, 2014) strictly recommend to verify the capillary tube dimensions, especially the inside diameter and the roughness, before installing it. As mentioned by Hermes et al. (2010), a 5% variation in the capillary tube diameter leads to an error up to 12.5% in the mass flow rate. In this sense, the capillary dimensions were checked previous to be installed at the workbench.

Five capillary tubes were bought in rolls with 3 meters length, three of them with inner nominal diameter of 1.07 mm (0.042”) and two with inner nominal diameter of 0.91 mm (0.036”). To avoid tube deformation and burr formation during the cut process, two techniques were tested to select the better: the cut by a thin saw blade and the cut by electrical discharge machining (EDM). The cross-section area of the capillary tube after the cut test can be seen in Fig. 3.2.

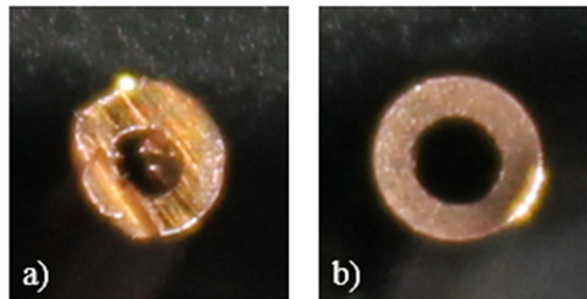


Figure 3.2: Cross section area after the cut test: a) with thin saw blade; b) with EDM machine.

As can be seen, the saw blade deformed the tube and generated burr, on the contrary of the achieved with the EDM. Then, this last method was selected to cut all the samples and the capillary tubes. Briefly, the EDM process cuts an object submerged in an electrolytic bath by passing an electric current, through an electrode, vaporizing the contact region. An electrolytic copper electrode was used with a current of 2 amperes. The approximate for a cut was 5 min. Despite the relatively large time necessary to cut with the EDM, the use of other processes would require many steps to deliver a good quality sample, such the embedding and sanding

processes. The EDM machine used is manufactured by ENGEMAQ, model EDM200NC, serie L, and is seen in Fig. 3.3. All the cut process was carried out at the Laboratório de Usinagem/UFGM.



Figure 3.3: EDM machine used to cut the capillary tubes.

### 3.2.1.1 Inner diameter measurements

The inner diameter measurements were carried out at the LABMETRO/UFGM, by means of the optical microscopy technique. The equipment used (Figure 3.4) is manufactured by Mitutoyo, code number 176-811A, with a resolution of 0.001 mm. For illustration, Figure 3.5 shows a sample amplified 30 times. The diameter was measured in different positions and then, the average was taken.

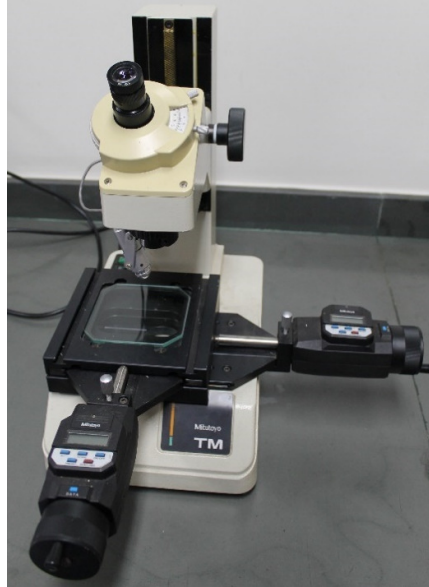


Figure 3.4: Microscope used for the inner diameter measurements.

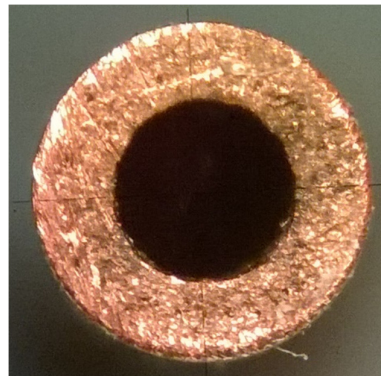


Figure 3.5: Sample 1D1 amplified 30 times.

### 3.2.1.2 Internal surface roughness measurements

For the internal surface roughness measurements, the samples were embedded and carefully sanded to remove as much as possible the copper walls of the capillary tube, without damaging the internal surface. Two different methods were used in these measurements: stylus (contact) profilometry and optical profilometry. The first measurement technique was realized at the Instrumented Hardness and Profilometry laboratory/UFMG. The equipment used (Fig. 3.6) is manufactured by Hommelwerke, model T8000, with a resolution of 0.1  $\mu\text{m}$ .

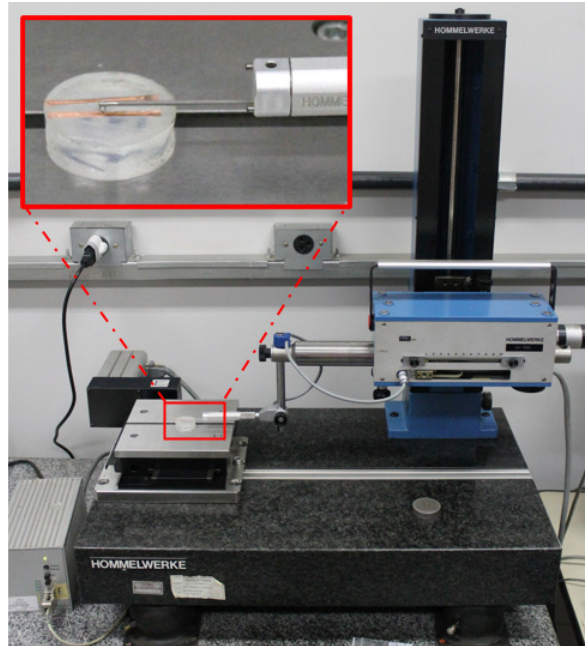


Figure 3.6: Stylus profilometer.

The probes TKU300/TS1 and 230475-KES/906D were used in all measurements. Briefly, in this technique, a rectangular area is divided in parallel lines in the length way, and the topography is obtained by passing the probe along these lines. As higher is the amount of lines, as higher will be the topography resolution. The measurement spacing in the length way is 1  $\mu\text{m}$ . Three lengths in each sample, selected close to the tube centerline, were considered to give the roughness parameters values.

The measurements by optical profilometry were realized at the LCPnano/UFG laboratory. The equipment used (Fig. 3.7) is manufactured by Zygo, model NewView 7300, with a resolution of 0.001  $\mu\text{m}$ . This equipment uses the method of interferometry, in which a light beam is emitted and split in two, travelling different lengths. Then, these beams are reunited, forming interference fringes, that are used to determine the distance between the surface in examination and the light receptor.



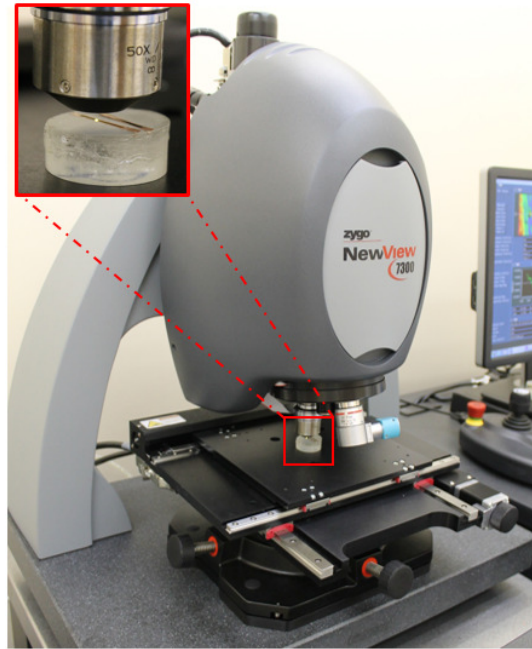


Figure 3.7: Optical profilometer.

With the measurements taken, it is important to decide which roughness parameter to use. Based on the results of Adams et al. (2012), and Young et al. (2009), and considering the measured values, a good choice would give a roughness between the corrected Ra and Rz. Eq. 2.23 could be a good candidate. However, this indicator involves a non-standardized parameter, making it difficult to be direct applied. Then, Eq. 2.23 was simplified to give Rp as the only variable. To do this, the  $\epsilon_{Fp}$  values presented in Yong et al. (2009) was divided by the Rp values and this result was averaged to give the multiplier factor of Rp. Table 3.3 resumes this process. The final relation to estimate the relative roughness ( $\epsilon$ ) is seen is Eq. 3.27.

Table 3.3: Roughness values for the new  $\epsilon_{Fp}$  definition

Material	Rp [ $\mu\text{m}$ ]	$\epsilon_{Fp}$ [ $\mu\text{m}$ ]	$\epsilon_{Fp}/R_p$ [ $\mu\text{m}$ ]
Copper	0.817	1.042	1.275
Copper	1.030	1.343	1.304
Copper	0.665	0.896	1.347
Aluminum	0.792	0.998	1.260
Aluminum	0.849	1.118	1.317
Aluminum	1.908	2.121	1.112
Stainless	0.774	1.065	1.376
Stainless	0.999	1.327	1.328
Stainless	3.210	4.269	1.330
Silicon	0.337	0.337	1.000
Nickel	0.118	0.147	1.246

Nickel	0.182	0.243	1.335
Nickel	0.449	0.577	1.285
Nickel	0.548	0.766	1.398
Nickel	1.159	1.766	1.524
Nickel	1.211	1.635	1.350
Nickel	1.697	2.484	1.464
Nickel	2.577	3.634	1.410
Nickel	1.770	2.419	1.367
Nickel	5.293	6.847	1.294
Nickel	3.668	5.048	1.376
<b>Average</b>			1.319

Source: adapted from Young et al. (2009).

$$\varepsilon = 1.319R_p \quad (3.27)$$

If only the data of copper, which is the most common material for capillary tubes, were used, the average would be 1.309. This value differs less than 1% to the global average, indicating that Eq. 3.27 can be a good estimate for copper capillary tubes.

### 3.2.1.3 Length and coil diameter measurements

To minimize the capillary tube deformation, they were not straightened to have the length measured. Instead, indirect measurements were carried out. Two different procedures were employed for capillary 4 and both results were compared, showing good agreement. For capillary tube 1, procedure 1 did no work, therefore, procedure 2 was used.

1- Passing a nylon fishing line inside the capillary tube rolls and, then, measuring the line length;

2-Measuring the coil diameter and, then, applying Eq. 3.28.

$$L = n' \sqrt{S^2 + (\pi D)^2} \quad (3.28)$$

where  $n'$  is the number of turns,  $S$  is the coil pitch, and  $D$  is the coil diameter. The coil diameter was measured by a calibrated analog caliper, manufactured by Mitutoyo. The capillary tube outer diameter was discounted to give the mean coil diameter.

### 3.2.2 Final dimensions and assembling

The coil diameter, the inner diameter, the length and the inner surface roughness for all the capillary tubes, as well as the associated uncertainties, are listed in Tab. 3.4. The inner diameter and the surface roughness will be assumed constant throughout the capillary tube length. More details about these measurements and the uncertainty analysis can be found in Appendix A.

Table 3.4: Final dimensions of the capillary tubes with the respective uncertainties.

Tube	D [mm]		d [mm]		L [mm]		$\varepsilon$ [ $\mu\text{m}$ ]	
	Value [mm]	U [mm]	Value [mm]	U [mm]	Value [mm]	U [mm]	Value [ $\mu\text{m}$ ]	U [ $\mu\text{m}$ ]
1	28.5	1.0	1.075	0.011	2973	21	2.96	1.45
4	75	0.5	0.911	0.016	1340	6	3.04	0.95

The capillary tubes were bought in rolls with 3 m length and diameter of approximately 120 mm (Figure 3.8a). They were cut and coiled around PVC tubes to achieve the final coil diameter (Figure 3.8b). Next, the capillary tubes extremities were inserted in a copper tube, with external and internal diameters of 6.35 mm and 3.17 mm, respectively. In one side, nuts were attached at the copper tube and at the other, the capillary tube was brazed (Figure 3.8c). To reduce the heat exchange between the capillary tube and the surroundings, it was placed centered inside a PVC tube case, forming a gap between them (Figure 3.8d). The case was, then, covered by the insulation blanket Vidoflex Wincell with 19 mm of thickness (Figure 3.8e). Finally, the capillary tube was integrated into the workbench (Figure 3.8f).

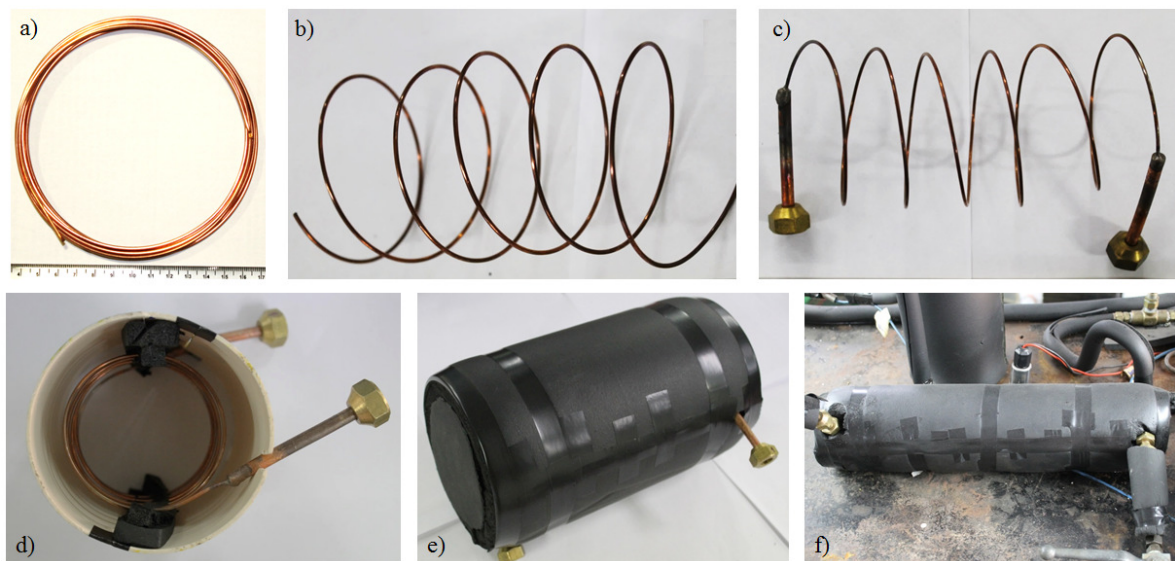


Figure 3.8: Sequence of the capillary tube assembling.

The minimum required thickness to support the hoop stress due to the internal pressure has been checked according to ASME B31.5 (ASME, 2013). To reduce the displacement that would tend to open the capillary tube helix, and to limit the axial stress, two strips of the insulation material were placed at opposite sides, between the capillary tube helix and the PVC tube (Figure 3.8d)).

### **3.3 Experimental characterization**

#### **3.3.1 Design of experiments**

According to Montgomery (2013), the basic principles of experimental designs are: randomization, replication and blocking. The first means that both, the allocation of material and the order of tests, should be performed randomly. It is necessary because the statistical methods require that the observations be distributed random variables. The second, replication, is important because it allows to estimate the experimental error and helps to get an estimation of the average response regarding an input variable. However, a distinction must be made between replication, which is redo the experiment, and repeated measurements, which is measure again in the same trial run. Lastly, the blocking allows to reduce or to eliminate the variability transmitted by input factors that are not the focus. A block generally represents a set of experiments grouped in relatively homogeneous conditions and, although the noise can be reduced, some of the randomness is lost.

In this work, it was considered that all tests are part of a single block. Then, the experiment conditions should present low variability, as will be presented in section 3.4. Were adopted 2 replicates of each test. The planning of the test sequence was partially randomized, due to the unstable solar radiation condition and difficulty of changing the capillary tube for each specific experiment.

Considering yet the principles of the factorial design, since they make the most efficient use of the experimental data (MONTGOMERY, 2013), a full factorial design was selected. In this technique, the experiments are defined based on a combination of factors - variables that can be controlled, in different levels - values of each variable. This design also allows to identify if interactions between variables exists. The factors and levels chosen are seen in Tab. 3.5. It was decided to use a fan in low solar radiation conditions, on the underside of the collector plate, to investigate the possibility to reduce the drawbacks of DX-SAHP (e.g lower heating capacity and COP), compared to an ASHP, when subjected to low solar radiation.

Table 3.5: Factors and levels.

Factors		Levels	
Capillary tube	1	-	4
Operational condition	High solar radiation (HSR)	Low solar radiation (LSR)	Low solar radiation with fan (LSR+fan)

Apart from the design of experiments described above, additional runs were performed to increase the number of points to validate the capillary tube algebraic solution. These tests were done by the combination and variation of the capillary tube, refrigerant mass (CO<sub>2</sub> inventory) on system, and use of the fan, always in low radiation condition. For a given capillary tube and CO<sub>2</sub> inventory, three different fan speeds were used to generate the data. Subsequently, the CO<sub>2</sub> inventory was slightly reduced and the data were collected for the three fan speeds. This process occurred approximately 5 times for each capillary tube. All tests, the factorial and additional ones, were performed from November 18<sup>th</sup> to December 19<sup>th</sup>, 2019.

### 3.3.2 Workbench description

The CO<sub>2</sub> DX-SAHP is installed at the laboratory of *Grupo de Refrigeração e Aquecimento-UFMG (GREA)*. It was designed to supply DHW for a residence with 4 people (DE OLIVEIRA, 2013). An overview of the equipment can be seen in Fig. 3.9.

Figure 3.9: Overview of the CO<sub>2</sub> DX-SAHP.

Recent works (PAULINO, 2019; RUAS, 2019) were realized in this workbench, but for the present study, some modifications were needed to incorporate the capillary tube, used for the first time. The before and after modifications can be seen in Figure 3.10.

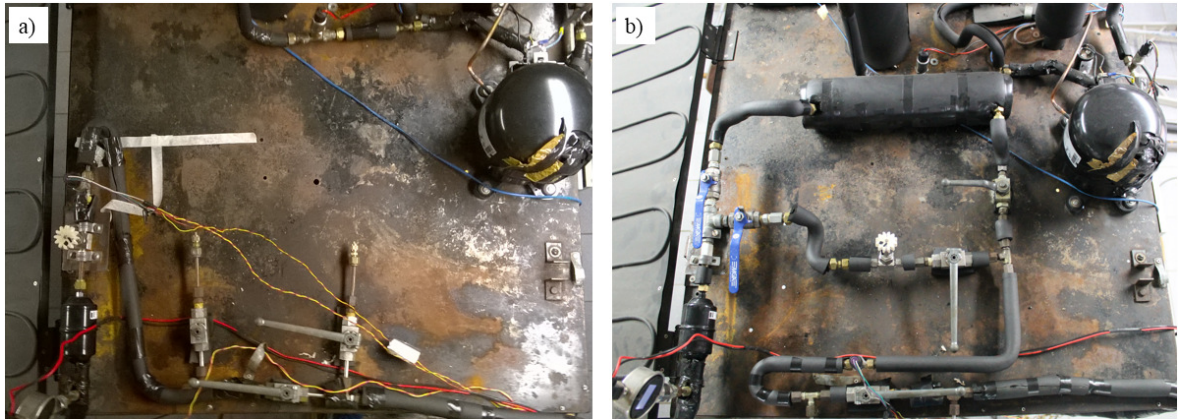


Figure 3.10: Top view of the workbench: a) before modifications; b) after modifications.

The DX-SAHP consists in a vapor compression machine operating in a transcritical CO<sub>2</sub> cycle, comprised by the following components: compressor, oil separator, gas cooler, needle valve and capillary tube in parallel, dryer filter, evaporator/collector, liquid separator, water pump with an embedded system to adjust the flow rate, measurement and data acquisition system.

### 3.3.2.1 Compressor

The compressor (Figure 3.11) is hermetic, reciprocating, manufactured by SANDEN, model SRCaDB. The displacement is 1.75 cm<sup>3</sup>, voltage of 110-127 V and nominal frequency of 60Hz.



Figure 3.11: Compressor.

### 3.3.2.2 Oil separator

The oil separator (Figure 3.12) is hermetic, manufactured by TEMPRITE, model 131, with maximum allowable pressure of 160 bar.



Figure 3.12: Oil separator.

### 3.3.2.3 Gas cooler

The gas cooler is a concentric tubes heat exchanger made of copper, flowing in counterflow, with the refrigerant fluid in the inner tube and water at the outer annulus. Due to the large length (24.3 m), it was helically coiled around the water reservoir and, then, this set was thermally insulated by a polyurethane foam, covered by an aluminum sheet. A picture of the gas cooler, and a schematic representation can be seen in Figure 3.13, while the main parameters is seen in Tab. 3.6.

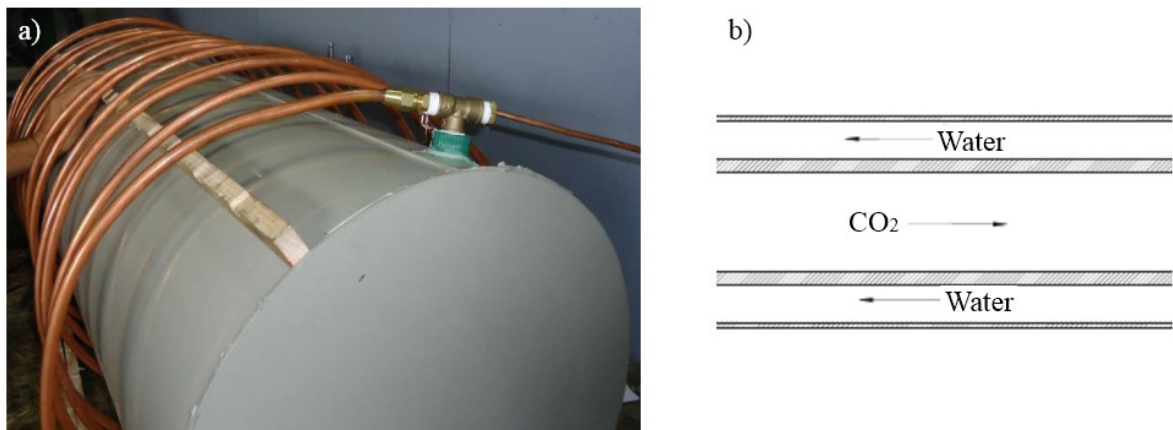


Figure 3.13: Gas cooler: Picture of the coil heat exchanger; b) schematic representation  
Source: adapted from De FARIA, 2013; De Olivera, 2013.

Table 3.6: Main parameters of the gas cooler

Internal tube inner diameter (CO <sub>2</sub> )	4.66 mm
Internal tube outer diameter (CO <sub>2</sub> )	6.34 mm
External tube inner diameter (water)	10.52 mm
External tube outer diameter (water)	12.5 mm
Gas cooler length	24.3 m

Source: adapted from Ruas (2019).

### 3.3.2.4 Expansion devices

The capillary tube was already described previously. The needle valve (Figure 3.14) is manufactured by SWAGELOK, model SS-31RSA, with an orifice diameter of 1.6 mm.



Figure 3.14: Needle valve.

### 3.3.2.5 Dryer filter

The dryer filter (Figure 3.15) is hermetic, manufactured by Danfoss, type DML, with 100% of molecular sieves in core.



Figure 3.15: Dryer filter.

### 3.3.2.6 Evaporator/collector

The evaporator/collector consists in a serpentine of copper tube attached to a copper plate, painted in black ink. A picture of this component can be seen in Figure 3.16, while the main parameters is seen in Tab. 3.7.



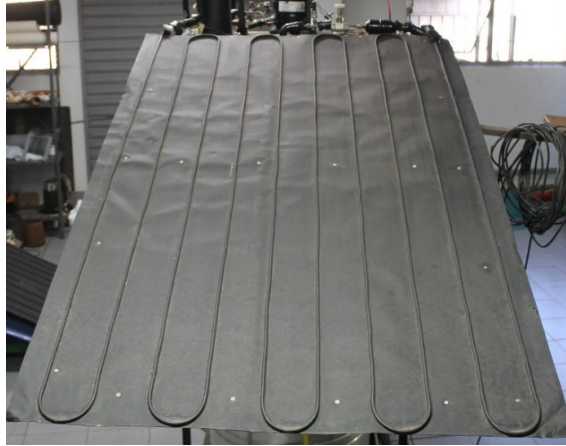


Figure 3.16: Evaporator/collector.

Table 3.7: Main parameters of the evaporator/collector

Tube inner diameter (CO <sub>2</sub> )	4.66 mm
Tube outer diameter (CO <sub>2</sub> )	6.34 mm
Tube length	16.3 m
Plate thickness	1 mm
Plate area	1.57 m <sup>2</sup>

Source: adapted from Ruas (2019).

### 3.3.2.7 Liquid separator

The liquid separator (Figure 3.17) is installed upstream the compressor, and is, basically, a cylinder with diameter of 90 mm, and high of 215 mm.



Figure 3.17: Liquid separator.

### 3.3.2.8 Water pump

The water pump (Figure 3.18) is manufactured by SHURflo, model 100-000-21, with an open flow of 1 gpm (227 L/h), and voltage of 12 V. The pump motor was subjected to a pulse width

modulation signal, generated by a proportional integral derivative controller, to vary the water flow rate. This embedded system was designed by Paulino (2019).



Figure 3.18: Water pump.

### 3.3.2.9 Measurement and data acquisition system

#### 3.3.2.9.1 Pressure measurement

Four pressure meters were used in the DX-SAHP. Two of them are pressure transducers manufactured by Fueltech, model PS1500PSI (Figure 3.19a), one is a pressure transducer manufactured by Novus, serie 520 (Figure 3.19b), and the other is a pressure gauge manufactured by Zurich, model PHD.IL (Figure 3.19c). The main specifications of these meters are seen in Tab. 3.8.

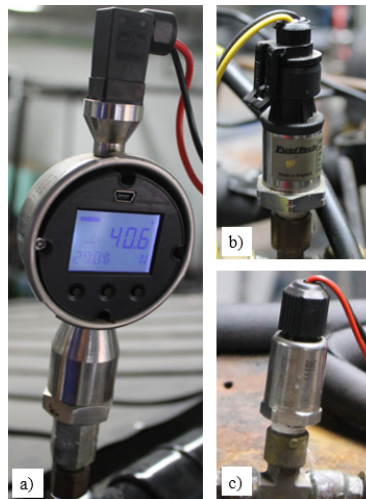


Figure 3.19: Pressure meters.

Table 3.8: Pressure meters main specifications.

<b>Fueltech transducer</b>		<b>Novus transducer</b>		<b>Zurich manometer</b>	
Pressure range	0-102 bar	Pressure range	0-60 bar	Pressure range	0-150 bar
Output (DC)	0.5-4.5 V	Output (DC)	4-20 mA	Output (DC)	4-20 mA
Input (DC)	5 V	Input (DC)	7-33 V	Input (DC)	10-45 V
Accuracy	$\pm 0.51$ bar	Accuracy	$\pm 0.18$ bar	Accuracy	$\pm 0.5$ bar

All of them have been verified before the beginning of the experiments. Details about this procedure can be found in Appendix B.1. Regarding the Novus transducer, since the output is amperes, it was necessary to use a 200 ohms resistor, with 5% of accuracy, to convert the signal to voltage in the range of 0.8-4 V, able to be read by the data acquisition board.

### 3.3.2.9.2 Temperature meters

All the temperature meters are T-type thermocouples, manufactured by ECIL, with sheath diameter of 1.5 mm, and uncertainty of  $\pm 0.5^{\circ}\text{C}$ . They are attached to the external copper tubes walls and properly insulated.

### 3.3.2.9.3 Solar radiation meter

The solar radiation was measured by a pyranometer (Figure 3.20), manufactured by Eppley, model 8-48. The main specifications are seen in Tab. 3.9.



Figure 3.20: Pyranometer.

Table 3.9: Main pyranometer specifications.

Analog output	0-10 mV
Maximum uncertainty	5% (of reading)
Constant	0.00000935 V/W/m <sup>2</sup>
95% response time	30 s

Due to the difficulty to verify the validity of the presented values for solar radiation, the constant given by the manufacturer was assumed true, disregarding possible changes since it was first used. This could lead to an error if the constant has changed a little. However, as the solar radiation will not be used as an input for any calculations, it is only a reference value, this do not represent a major issue.

### 3.3.2.9.4 Wattmeter

A wattmeter, manufactured by ABB, model ETP-30 (Figure 3.21), was used to measure the electrical power supplied to the compressor. The main specifications are seen in Tab. 3.10. Since the output is amperes, it was necessary to use a 220 ohms resistor, with 5% of accuracy, to convert the signal to voltage. The response curve Voltage vs Power was obtained using reference light bulbs. This procedure can be seen in Appendix B.2. The electrical power uncertainty, including all uncertainty sources, was estimated in 5% of the reading.



Figure 3.21: Wattmeter.

Table 3.10: Main wattmeter specifications.

Power range	0-1039.23 W
Output (DC)	4-20 mA
Maximum uncertainty	$\pm 2.6$ w (0.25%)

### 3.3.2.9.5 Water flow rate meter

The water flow rate was measured by timing the necessary time for water to fill a certain volume. It was used a graduated beaker, with uncertainty of 2 mL, and a chronometer, with uncertainty of the whole operation estimated in 1 second. The average of at least three measurements were considered to give each water flow rate.

### 3.3.2.9.6 Refrigerant mass flow rate

Since a refrigerant mass flow rate meter was not available, this variable was estimated by an energy balance at the gas cooler, as seen in Eq. 3.29.

$$\dot{m}_w c_p (T_{W2} - T_{W1}) = \dot{m} (h_3 - h_2) \quad (3.29)$$

where  $\dot{m}_w$  is the water mass flow rate,  $c_p$  is the water specific heat, calculated at the average inlet and outlet water temperature,  $T_{W1}$  and  $T_{W2}$  are the water temperature at the inlet and outlet of the gas cooler, respectively,  $\dot{m}$  is the refrigerant mass flow rate,  $h_3$  and  $h_2$  are the refrigerant specific enthalpies at the outlet and inlet of the gas cooler. It was considered that all the heat released by the refrigerant fluid is completely absorbed by the water, that is, 100% of gas cooler thermal performance.

### **3.3.2.9.7 Acquisition System**

The voltage signals generated by the pressure transducers, the pyranometer, and the wattmeter were sent to a National Instruments board, model USB-6211, while the thermocouples signals were sent to a National Instruments board, model USB-9213. Both boards were connected to a computer, where a Labview interface program, developed by Ruas (2019), displayed the data and exported them to an excel file.

## **3.4 Experimental procedure**

To avoid great changes in weather conditions that could impact the results, the high solar radiation experiments were performed between 11:00 am and 1:00 pm, due to the more stable solar radiation. In this case, the evaporator/collector was inclined in an angle of 30° with the horizontal, pointed to the geographic north. The low solar radiation experiments were conducted indoors. The water temperature at the gas cooler outlet was kept constant at 61°C, adjusting the flow rate by means of a controller, which control algorithm was developed by Paulino (2019). This temperature was set to minimize the risk of Legionellosis bacteria formation in the water (RABELO ET AL., 2019)

A schematic representation of the workbench, including the instruments, is seen in Figure 3.22. All measured variables were collected when the system reached the steady-state regime, about 30 minutes after turning the DX-SAHP on. The list of measured variables and the respective nomenclature are seen in Tab. 3.11, while the list of calculated variables is seen in Tab. 3.12.

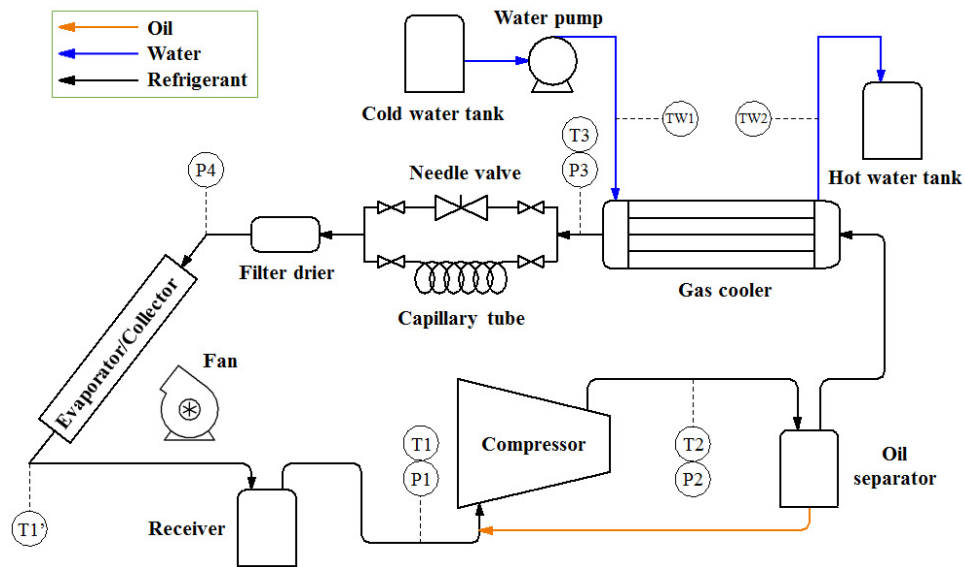


Figure 3.22: Schematic representation of the workbench.

Table 3.11 Measured variables.

Variable	Nomenclature	Unit	Instrument
Pressure at the compressor inlet	P1	bar	Novus transducer
Pressure at the compressor outlet	P2	bar	Fueltech transducer
Pressure at the expansion device inlet	P3	bar	Fueltech transducer
Pressure at the expansion device outlet	P4	bar	Zurich pressure gauge
Temperature at the compressor inlet	T1	°C	T type thermocouple
Temperature at the gas cooler inlet	T2	°C	T type thermocouple
Temperature at the gas cooler outlet	T3	°C	T type thermocouple
Temperature at the evaporator/collector outlet	T1'	°C	T type thermocouple
Temperature of the inlet water	TW1	°C	T type thermocouple
Temperature of the outlet water	TW2	°C	T type thermocouple
Ambient temperature	TA	°C	T type thermocouple
Water volumetric flow rate	V	m <sup>3</sup> /h	beaker and chronometer
Solar radiation	Rad	W/m <sup>2</sup>	Pyranometer
Electrical power	$\dot{W}$	W	Wattmeter

Table 3.12 Calculated variables.

Variable	Nomenclature	Unit
Heating Capacity	$\dot{Q}_h$	W
Superheat degree	$\Delta T$	°C
COP	COP	-
Refrigerant mass flow rate	$\dot{m}$	kg/h

In Tab. 3.12, the  $\dot{Q}_h$ , the  $\Delta T$ , and the COP are calculated by Eq. 3.30, 3.31 and 3.32, respectively. The compressor electrical power and the fan electrical power, when is the case, are considered in COP calculations.

$$\dot{Q}_h = \dot{m}_w c_p (T_{W2} - T_{W1}) \quad (3.30)$$

$$\Delta T = T_1 - T(P_4) \quad (3.31)$$

$$\text{COP} = \frac{\dot{Q}_h}{\dot{W}} \quad (3.32)$$

where in Eq. 3.31,  $T(P_4)$  is the saturation temperature at pressure  $P_4$ . The sequence of the experimental procedure is according to the following steps:

- 1- To inspect the workbench for abnormalities and to check the valves position;
- 2- To turn on the data acquisition system and to initiate the Labview interface program;
- 3- To turn on the water pump and to assure the complete filling of the condenser tube;
- 4- To turn on the compressor and to monitor the measured variables;
- 5- To verify if steady-state was achieved;
- 6- To measure the water flow rate;
- 7- To store the pressure displayed by the manometer together with other measured variables;
- 8- To open the valve to allow the oil to return to the compressor, every 30 min. Close the valve;
- 9- To turn the compressor off;
- 10- To turn off the water pump;
- 11- To turn the data acquisition off and to close the interface program.

All pressures given by the measurement system are gauge pressures. To convert to absolute pressures, data for atmospheric pressure were used. This information is collected by a meteorological station, placed about 1.7 km distance from GREA laboratory (Figure 3.23), and stored hourly at INMET website (INMET, 2019). The altitude difference is about 50 meters. To avoid confusion, the results section will only refer to absolute pressures.



Figure 3.23: Experiments location and meteorological station location.

### 3.5 Uncertainty analysis

#### 3.5.1 Direct measurements

In a measuring process different factors that lead to doubts in results can exist, i.e. different uncertainty sources can be present. Each of them contributes with two terms: systematic and random. The first is expressed by the bias ( $Td$ ), which is the difference between the average of indications ( $MI$ ) and the true value ( $VVC$ ), Eq. 3.33 (ALBERTAZZI, 2008).

$$Td = MI - VVC \quad (3.33)$$

The second term is expressed by the standard uncertainty. Two ways are commonly used to quantify it: statistical procedures (type A) and non-statistical procedures (type B). In type A, the standard uncertainty ( $u'$ ) can be evaluated by the sample standard deviation ( $s$ ), Eq. 3.34.

$$u' = s = \sqrt{\frac{\sum_{i=1}^n (I_i - MI)^2}{n - 1}} \quad (3.34)$$

where ( $I_i$ ) is the  $i$ -th indication and ( $n$ ) is the number of sample data. The degrees of freedom ( $\nu$ ) involved in standard uncertainty determination can be calculated by  $n$  independent measurements, according to Eq. 3.35.



$$v = n - 1 \quad (3.35)$$

In non-statistical procedures, the standard uncertainty will depend on the probability distribution. For rectangular distribution,  $s$  is calculated by Eq. 3.36, where  $a'$  is the expected interval for the indications occurrence.

$$u' = \frac{a'}{\sqrt{3}} \quad (3.36)$$

Having all the components of each uncertainty source, the combined bias ( $Td_c$ ), the combined uncertainty ( $u'_c$ ) and the effective degrees of freedom ( $v_{ef}$ ) can be estimated by Eq. 3.37, 3.38, and 3.39, respectively, when statistical independence between the data exists.

$$Td_c = \sum_{i=1}^n Td_i \quad (3.37)$$

$$u'_c = \sqrt{\sum_{i=1}^n (u'_i)^2} \quad (3.38)$$

$$\frac{u_c^4}{v_{ef}^4} = \sum_{i=1}^n \frac{(u'_i)^4}{(v_i)^4} \quad (3.39)$$

where  $Td_i$  is the  $i$ -th bias,  $u'_i$  is the  $i$ -th standard uncertainty and  $v_i$  is the  $i$ -th degree of freedom associated to the  $i$ -th standard uncertainty. Finally, the expanded uncertainty ( $U$ ) can be calculated by Eq. 3.40.

$$U = k_{95} \cdot u_c \quad (3.40)$$

where  $k_{95}$  is the Student's  $t$  coefficient, with a coverage of 95.45%.

### 3.5.2 Indirect measurements

The combined uncertainty of a quantity ( $u(G)$ ) obtained indirectly by the combination of other quantities non-correlated can be estimated by Eq. 3.41 (JCGM, 2008).

$$u^2(G) = \sum_{i=1}^N \left( \frac{\partial f}{\partial G_i} u(G_i) \right)^2 \quad (3.41)$$

where  $u(G)$  is the combined uncertainty,  $u(G_i)$  is the standard uncertainty of the  $i$ -th variable,  $\frac{\partial f}{\partial G_i}$  is the partial derivative of the function that relates all quantities, and  $N$  is the number of variables.

### 3.6 Validation of the capillary tube algebraic solution

To validate the capillary tube algebraic solution, the experimental refrigerant mass flow rate will be used for comparison. Then, Eq. 3.19 should be given in an appropriate form to predict the CO<sub>2</sub> mass flow rate. Substituting Eq. 3.17 and 3.18 into Eq. 3.19 and isolating the mass flux,  $G$ , Eq. 3.42 is found. This equation differs from Eq. 2.10 due to the terms inside the natural logarithms in the numerator.

$$\dot{m} = \frac{\pi d^2}{4} \sqrt{\frac{f_{tp} \left[ \frac{p_{in} - p_r}{t} + \frac{u}{t^2} \ln \left( \frac{tp_r + u}{tp_{in} + u} \right) \right] + f_{sp} \left[ \frac{p_r - p_{out}}{a} + \frac{b}{a^2} \ln \left( \frac{ap_{out} + b}{ap_r + b} \right) \right]}{\frac{f_{tp} f_{sp} L}{2d} + f_{tp} \ln \left( \frac{v_r}{v_{in}} \right) + f_{sp} \ln \left( \frac{v_{out}}{v_r} \right)}} \quad (3.42)$$

It should be mentioned that the mass flow rate is not an explicit variable, once the friction factor is function of Reynolds number. However, no more than 3 iterations are sufficient to achieve a relative error of 0.5%. At the fourth iteration, a convergence of about 0.01% is achieved. Despite the large amount of equations involved, the proposed capillary tube algebraic solution can be easily implemented in a spreadsheet, without the necessity of developing any especial algorithm.

The experimental data obtained in low radiation tests, with and without the fan, were used for comparison. In all this points, the solar radiation did not exceed 10 W/m<sup>2</sup>. The differences between the predicted and the experimental mass flow rates will be analyzed by the average deviation (AD), the absolute average deviation (AAD) and root mean square (RMS), calculated by Eq. 3.43, 3.44 and 3.45, respectively.

$$AD = 100\% \left( \frac{1}{n} \sum_n \frac{\dot{m}_{predicted} - \dot{m}_{measured}}{\dot{m}_{measured}} \right) \quad (3.43)$$

$$AAD = 100\% \left( \frac{1}{n} \sum_n \left| \frac{\dot{m}_{predicted} - \dot{m}_{measured}}{\dot{m}_{measured}} \right| \right) \quad (3.44)$$

$$\text{RMS}=100\% \sqrt{\frac{1}{n-1} \sum_n \left( \frac{\dot{m}_{\text{predicted}} - \dot{m}_{\text{measured}}}{\dot{m}_{\text{measured}}} - \text{AD} \right)^2} \quad (3.45)$$

## 4 RESULTS AND DISCUSSIONS

### 4.1 Experimental results and heat pump behavior

According to the factorial design, 12 experiments were carried out to investigate the operational conditions and the capillary tube effects on the heat pump behavior. To calculate the variables, including the thermophysical properties, the Engineering Equation Solver (EES) was used. The main measured variables, the heating capacity, the superheat degree, the COP, and the refrigerant mass flow rate can be seen in Tab. 4.1, while the respective uncertainties are seen in Tab. 4.2. For reference, the CO<sub>2</sub> inventory for experiments with the capillary tube 1 was 766 g.

Table 4.1 Results of the factorial design.

Test	Condition	Cap. Tube	P1 [bar]	P2 [bar]	TW1 [°C]	TW2 [°C]	TA [°C]	Rad [W/m <sup>2</sup> ]	$\dot{m}$ [kg/h]	Qh [W]	$\Delta T$ [K]	COP
A1	HSR	1	49.9	86.7	28.2	61.5	29.1	1020	28.89	1912	31.0	3.14
A2	HSR	1	49.6	86.9	28.9	61.1	29.3	955	28.61	1848	27.8	2.97
B1	LSR+fan	1	42.5	84.7	25.1	61.5	26.5	8	25.09	1468	7.2	2.22
B2	LSR+fan	1	43.9	85.5	26.3	61.1	27.3	7	24.21	1426	8.6	2.05
C1	LSR	1	39.5	83.1	25.3	60.9	25.4	4	21.59	1225	4.5	2.13
C2	LSR	1	40.5	84.0	26.2	61.0	27.1	6	22.69	1279	4.6	2.31
A3	HSR	4	52.5	88.9	28.9	61.0	30.6	960	32.93	1985	29.8	3.20
A4	HSR	4	53.0	89.0	29.3	61.0	33.5	942	28.06	1983	33.7	3.16
B3	LSR+fan	4	43.7	86.3	26.2	61.1	27.8	6	25.18	1440	5.7	2.10
B4	LSR+fan	4	43.0	86.3	26.6	61.0	27.7	6	25.08	1400	4.7	2.16
C3	LSR	4	40.3	83.6	26.0	61.2	26.7	8	21.96	1222	4.3	2.25
C4	LSR	4	39.9	83.4	26.7	61.0	28.1	6	21.55	1168	4.4	2.08

Table 4.2 Uncertainties of the measured variables.

Test	U( $\dot{m}$ ) [kg/h]	U( $\dot{Q}_h$ ) [W]	U( $\Delta T$ ) [K]	U(COP)
A1	1.09	69	0.7	0.19
A2	1.10	68	0.7	0.18
B1	0.81	43	0.7	0.13
B2	0.81	43	0.7	0.12
C1	0.70	33	0.7	0.12
C2	0.76	37	0.7	0.13
A3	1.44	76	0.7	0.20
A4	1.15	80	0.7	0.20
B3	0.83	43	0.7	0.12
B4	0.84	42	0.7	0.13
C3	0.73	33	0.7	0.13
C4	0.80	32	0.7	0.12

As already expected, the raise in solar radiation caused an augment on the heating capacity, on COP, on the refrigerant mass flow rate, and on the superheat degree, as discussed by Rabelo et al. (2019). These augments were of 57.9%, 42.3%, 35%, and from 4.4 K to 30.6 K, on average, respectively. The minimum and maximum COP were 2.05 and 3.20, respectively, with an average COP for high solar radiation experiments of 3.12. This value is similar to the maximum COP presented by Rabelo et al. (2019) and, as discussed by the authors, the DX-SAHP could operate near to the optimum high pressure using a capillary tube. Concerning the superheat degree, most of the compressor manufacturers recommend to maintain a maximum superheat degree of 20 K to 30 K, due to the degradation of the lubricant oil. Then, a continuous operation in a high level of solar radiation, around 1000 W/m<sup>2</sup>, added to high ambient temperatures, could compromise the compressor integrity. A possible alternative would be the use of two capillary tubes configured in parallel, one for lower radiation, and other for higher radiation. However, for regions with maximum radiation below the levels analyzed in these experiments, the use of a single capillary tube could be a satisfactory choice. Another possibility would be the use of a static heat exchanger, placed between the evaporator exit and the compressor inlet. This component could be as simple as a copper tube externally finned. For high solar radiation, the refrigerant would be cooled up to the compressor, reducing the superheat degree, while for low solar radiation, the refrigerant could be slightly heated, increasing the superheat.

The addition of a fan in low radiation conditions also improved the heating capacity in 17.2%, raised the mass flow rate in 13.4% and the superheat from 4.4 to 6.6 K, on average. Regarding the COP, the conclusions were not obvious, since the increase in thermal energy inputted to the evaporator/collector was balanced with the extra electrical power consumed by the fan. The fan was not turned on during the high radiation experiments, since most of the collector plate area experienced temperatures above the ambient, which could lead to a heat rejection from the collector, reducing its thermal performance. As also expected, the solar radiation, or the heat gain from convection, increased the evaporating pressure (P1). However, the gas cooler pressure (P2) also showed an increase with the raise in energy inputted to the evaporator. This variation is more significative than that reported by Rabelo et al. (2019) and Kong et al. (2018). Figure 4.1 illustrates the evaporating pressure and gas cooler pressure responses with the solar radiation variation, in two different experiments.

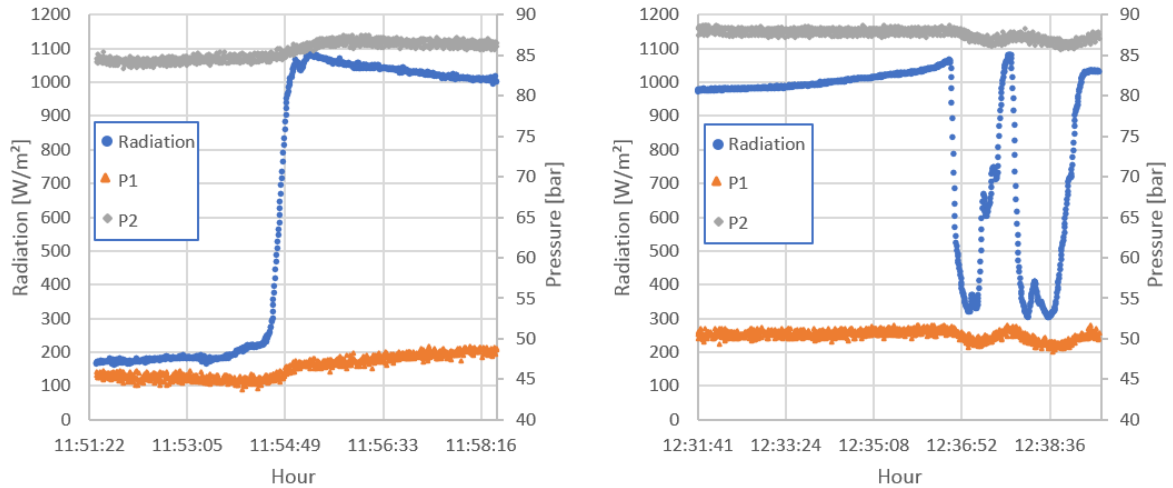


Figure 4.1: Variation of evaporating and gas cooler pressures with solar radiation, for two different experiments.

As can be seen in Figure 4.1, both pressures have similar behavior regarding the solar radiation variation. In the left image, the peak in solar radiation around the hour 11:54 caused a raise in both pressures, with approximate variation from 85 to 87 bar and 45 to 49 bar, for P1 and P2, respectively. In the right image, at about 12:36 the pressures started to lower, followed by an increase, a further decrease, and a final increase, always in accordance with the solar radiation trend. The approximate maximum variation was from 87.5 to 86 bar and from 51 to 48 bar, for P1 and P2, respectively. Nevertheless, the alteration intensity seems to be more pronounced for the evaporating pressure. Most of the comments drawn in the above paragraphs can also be visualized in a pressure versus enthalpy diagram, for experiments A1, B1, and C1, represented in Figure 4.2.

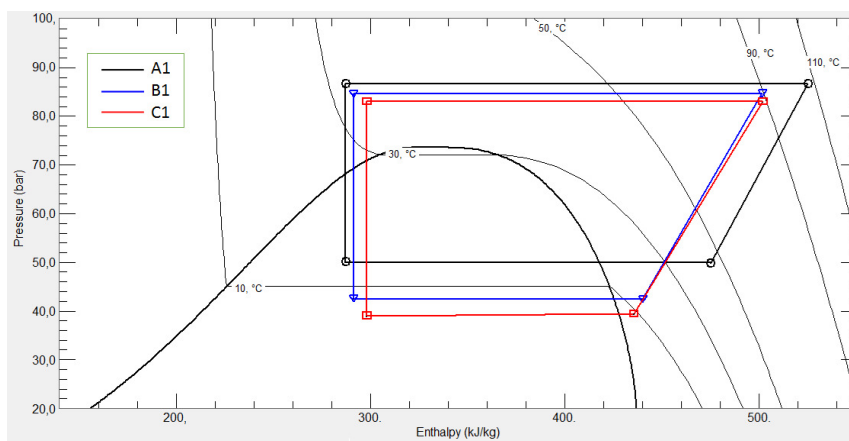


Figure 4.2: Ph diagram of experiments A1, B1, and C1.

To further investigate the results presented in Tab. 4.1 and to substantiate the findings statistically, an Analysis of Variance (ANOVA) was performed, with a confidence level of 95%. The main effects plots are seen in Figure 4.3.

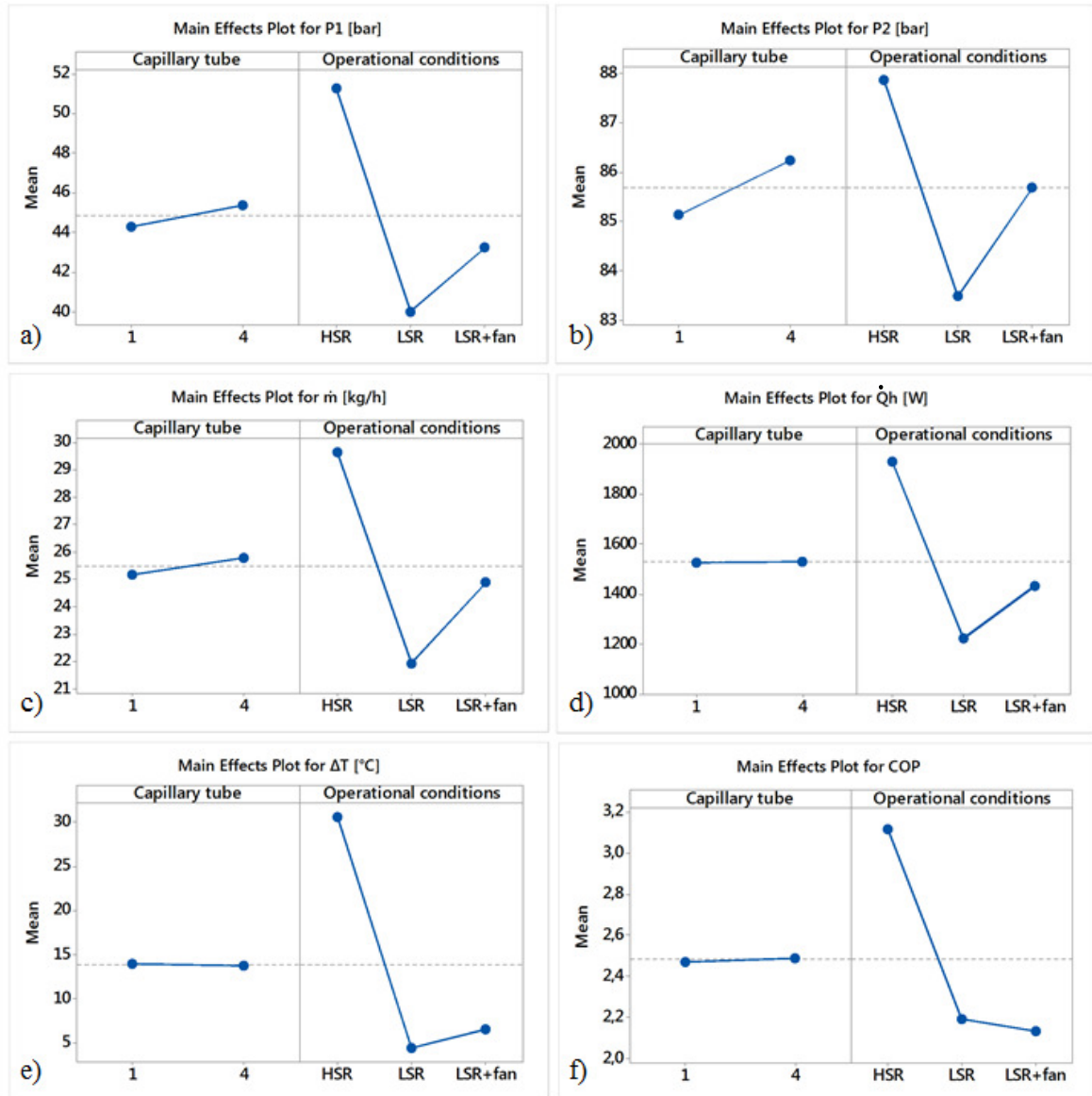


Figure 4.3: Main effects plots for: a) evaporating pressure; b) gas cooler pressure; c) refrigerant mass flow rate; d) heating capacity; e) superheat degree; f) COP.

Regarding the capillary tube factor, there was no difference for means of COP, superheat, and heating capacity, when the system operates with capillary tubes 1 or 4. For the mass flow rate and the evaporating pressure, there was a slightly augment, while for the gas cooler pressure, the increase was a little higher. This could be related to some difference of CO<sub>2</sub> mass on system, once these three parameters are directly proportional to the inventory. However, the ANOVA

indicated that there was no difference in none of these means when the capillary tube changed as can be seen in Figure 4.4a-c, for  $\dot{m}$ , P1, and P2, respectively.

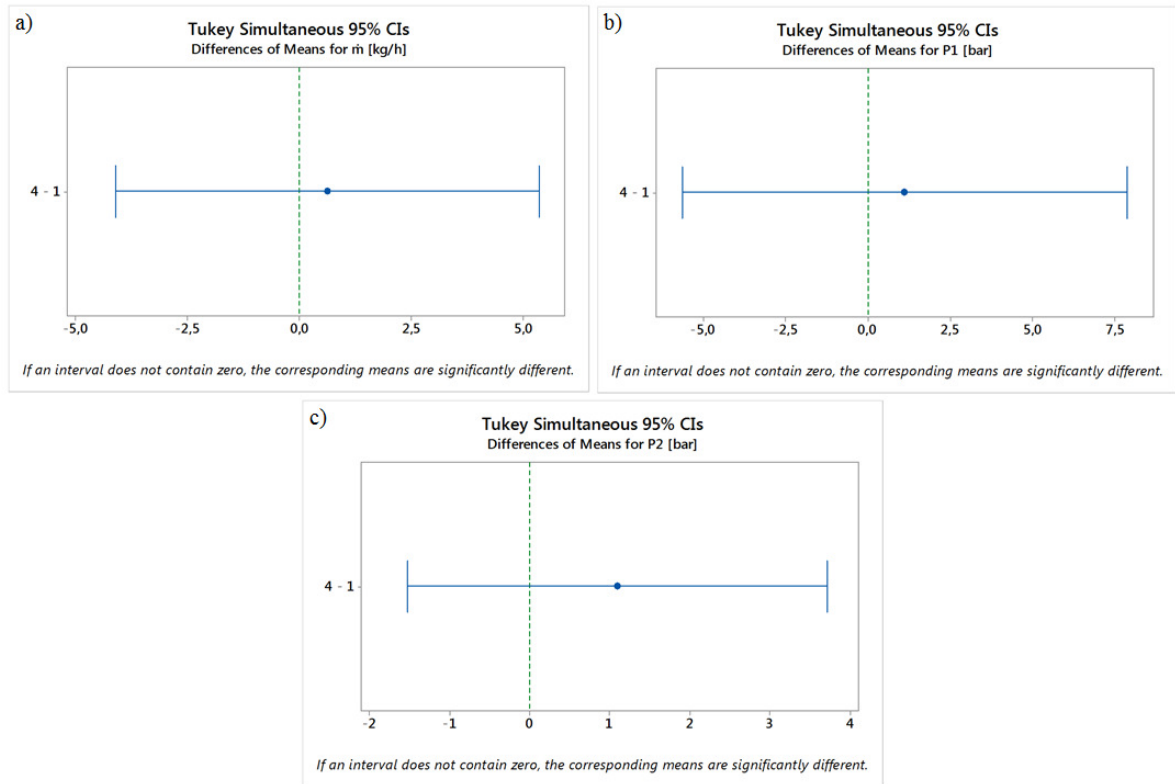


Figure 4.4: Comparison between capillary tubes levels: a) refrigerant mass flow rate; b) evaporating pressure; c) gas cooler pressure.

The greatest changes occurred when the operational conditions changed. All variables presented notorious differences, except the  $\Delta T$  and the COP when changing from LSR to LSR+fan. The ANOVA confirmed no difference in these two cases as can be seen in Figure 4.5a-b. Therefore, the addition of a fan improved the heating capacity without penalty the performance. Then, the hybrid DX-SAHP/ASHP proved to be advantageous in low solar radiation conditions. On the other hand, the fan represents an extra component, raising the investment cost.

To statistically support the conclusion that the gas cooler pressure is also affected by the solar radiation, the comparison result is shown in Figure 4.5c. In all cases in which ANOVA was used, Tukey's test was adopted, data normality could be assumed, and no outlier point, using Grubbs' test, were indicated.



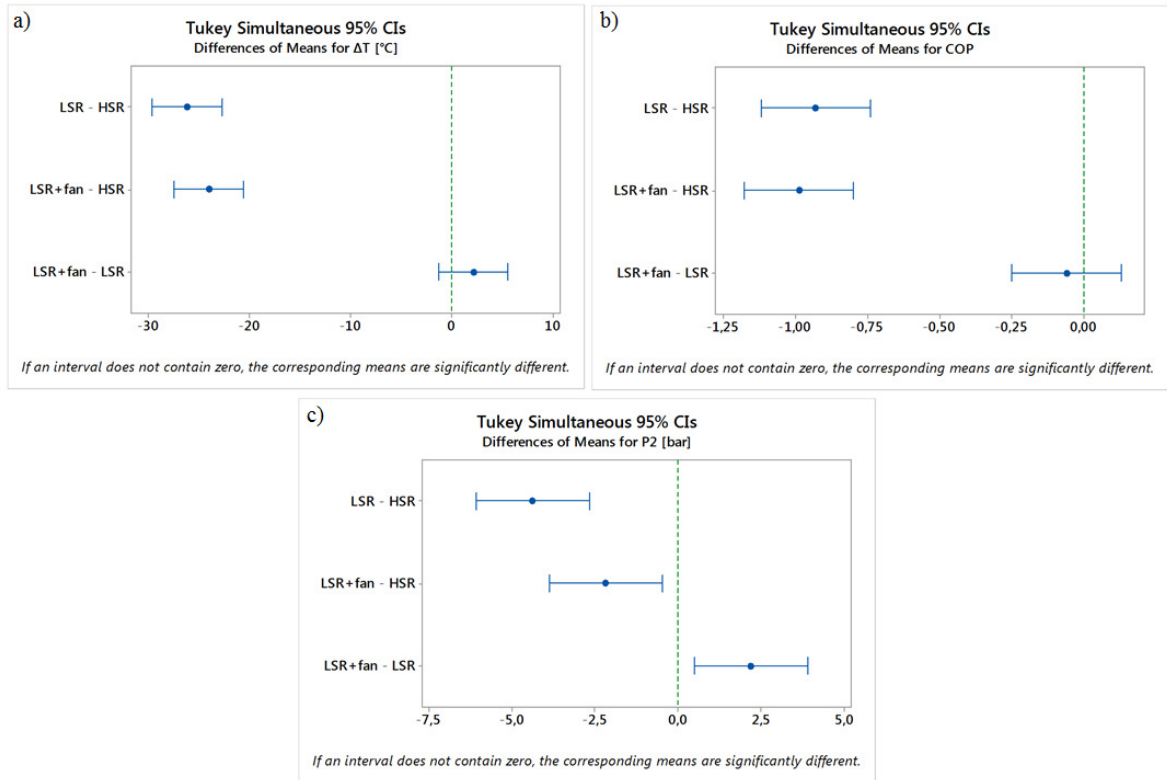


Figure 4.5: Comparison between operational conditions levels: a) superheat degree; b) COP; c) gas cooler pressure.

## 4.2 Results of the capillary tube algebraic solution validation

The results for the experimental mass flow rates and the main measured variables are seen in Tab. 4.3. The refrigerant mass flow rates ranged from 17.97 kg/h to 26.46 kg/h. All experimental data fell in the left side of the critical point, as presented in Figure 3.1a.

Table 4.3 Experimental results for refrigerant mass flow rates.

Point number	L [m]	d [mm]	D [mm]	$\epsilon$ [ $\mu\text{m}$ ]	P <sub>in</sub> [Mpa]	T <sub>in</sub> [°C]	P <sub>out</sub> [Mpa]	$\dot{m}$ [kg/h]	U( $\dot{m}$ ) [kg/h]
1	2.973	1.075	28.5	2.96	8.400	33.59	3.932	22.75	0.81
2	2.973	1.075	28.5	2.96	8.408	33.51	3.942	22.91	0.74
3	2.973	1.075	28.5	2.96	8.380	33.29	3.900	21.76	0.70
4	2.973	1.075	28.5	2.96	8.348	33.23	3.927	22.23	0.72
5	2.973	1.075	28.5	2.96	8.466	32.35	4.257	25.09	0.81
6	2.973	1.075	28.5	2.96	8.232	33.05	3.882	21.96	0.73
7	2.973	1.075	28.5	2.96	8.546	32.19	4.312	25.29	0.81
8	2.973	1.075	28.5	2.96	8.595	32.40	4.272	23.51	0.76
9	2.973	1.075	28.5	2.96	8.307	33.08	3.902	21.59	0.70
10	2.973	1.075	28.5	2.96	8.695	32.69	4.402	26.46	0.92
11	2.973	1.075	28.5	2.96	8.396	33.49	4.032	22.69	0.76
12	2.973	1.075	28.5	2.96	8.543	32.82	4.372	24.21	0.81
13	2.973	1.075	28.5	2.96	8.553	32.86	4.372	24.93	0.82

14	2.973	1.075	28.5	2.96	8.369	33.40	3.982	21.36	0.70
15	2.973	1.075	28.5	2.96	8.388	32.84	4.257	23.66	0.79
16	2.973	1.075	28.5	2.96	8.404	32.67	4.302	23.91	0.79
17	2.973	1.075	28.5	2.96	8.191	33.15	3.922	20.53	0.70
18	2.973	1.075	28.5	2.96	8.191	33.11	4.077	21.55	0.74
19	2.973	1.075	28.5	2.96	8.224	33.07	4.142	22.24	0.78
20	2.973	1.075	28.5	2.96	7.972	32.80	3.832	19.41	0.73
21	2.973	1.075	28.5	2.96	8.000	33.00	3.942	20.48	0.78
22	2.973	1.075	28.5	2.96	8.037	32.95	4.002	20.82	0.76
23	2.973	1.075	28.5	2.96	8.043	32.93	3.892	19.58	0.71
24	2.973	1.075	28.5	2.96	8.021	32.55	3.822	18.49	0.63
25	2.973	1.075	28.5	2.96	7.956	32.45	3.927	19.26	0.67
26	2.973	1.075	28.5	2.96	7.920	32.41	3.817	18.63	0.67
27	2.973	1.075	28.5	2.96	7.937	32.55	3.917	19.46	0.71
28	2.973	1.075	28.5	2.96	7.882	32.43	3.872	18.87	0.71
29	2.973	1.075	28.5	2.96	7.842	32.18	3.782	17.97	0.66
30	1.34	0.911	75	3.04	8.179	32.76	3.927	21.17	0.69
31	1.34	0.911	75	3.04	8.335	32.52	3.922	20.71	0.63
32	1.34	0.911	75	3.04	8.564	32.05	4.262	24.06	0.76
33	1.34	0.911	75	3.04	8.519	32.10	4.312	24.37	0.78
34	1.34	0.911	75	3.04	8.289	33.04	3.952	21.83	0.70
35	1.34	0.911	75	3.04	8.506	31.94	4.352	25.52	0.81
36	1.34	0.911	75	3.04	8.531	31.82	4.387	25.25	0.80
37	1.34	0.911	75	3.04	8.896	31.89	4.372	25.91	0.81
38	1.34	0.911	75	3.04	8.461	33.02	3.987	21.72	0.67
39	1.34	0.911	75	3.04	8.692	31.88	4.402	25.96	0.82
40	1.34	0.911	75	3.04	8.736	31.69	4.392	26.28	0.83
41	1.34	0.911	75	3.04	8.505	33.10	4.022	22.47	0.72
42	1.34	0.911	75	3.04	8.924	31.62	4.447	26.23	0.82
43	1.34	0.911	75	3.04	8.367	33.55	3.977	21.96	0.73
44	1.34	0.911	75	3.04	8.318	33.83	3.942	21.59	0.76
45	1.34	0.911	75	3.04	8.623	32.88	4.337	25.18	0.83
46	1.34	0.911	75	3.04	8.343	34.25	3.947	21.55	0.80
47	1.34	0.911	75	3.04	8.624	33.46	4.281	24.72	0.83
48	1.34	0.911	75	3.04	8.618	33.35	4.281	25.08	0.84
49	1.34	0.911	75	3.04	8.522	33.43	4.267	23.67	0.77
50	1.34	0.911	75	3.04	8.419	33.98	4.017	22.01	0.78
51	1.34	0.911	75	3.04	8.527	33.64	4.267	23.17	0.77
52	1.34	0.911	75	3.04	8.392	33.66	4.202	22.92	0.78
53	1.34	0.911	75	3.04	8.319	33.94	4.007	21.72	0.77
54	1.34	0.911	75	3.04	8.376	33.74	4.187	22.24	0.79
55	1.34	0.911	75	3.04	8.031	33.00	4.012	19.69	0.72
56	1.34	0.911	75	3.04	8.151	33.54	4.137	20.92	0.79
57	1.34	0.911	75	3.04	8.208	33.69	4.172	20.88	0.78
58	1.34	0.911	75	3.04	8.010	33.09	3.942	19.29	0.75
59	1.34	0.911	75	3.04	8.060	33.22	4.022	20.00	0.78
60	1.34	0.911	75	3.04	8.075	32.95	4.062	20.11	0.73

To verify the performance of the proposed algebraic solution, the thermophysical properties needed in Eq. 3.42 were calculated using REFPROP 8.0. A total of nine combinations were tested, varying the k factors and the friction factor, as seen in Table 4.4.

Table 4.4 Combinations of k and friction factors.

Combination	k factors		Friction factor	
	1	Hermes et al. (2009)	Eq. 3.10, 3.15	Schmidt
2	Hermes et al. (2009)	Eq. 3.10, 3.15	C- M&N	-
3	Hermes et al. (2009)	Eq. 3.10, 3.15	M&N	Eq. 3.25
4	Bhattacharyya et al. (2010) with j factor	Eq. 3.11a-b and 3.16	Schmidt	Eq. 3.24
5	Bhattacharyya et al. (2010) with j factor	Eq. 3.11a-b and 3.16	C- M&N	-
6	Bhattacharyya et al. (2010) with j factor	Eq. 3.11a-b and 3.16	M&N	Eq. 3.25
7	Bhattacharyya et al. (2010) without j factor	Eq. 3.11a, 3.16	Schmidt	Eq. 3.24
8	Bhattacharyya et al. (2010) without j factor	Eq. 3.11a, 3.16	C- M&N	-
9	Bhattacharyya et al. (2010) without j factor	Eq. 3.11a, 3.16	M&N	Eq. 3.25

The predicted mass flow rates using the algebraic solution were compared to the experimental mass flow rates, and the AD, the ADD, and the RMS calculated are shown in Tab. 4.5.

Table 4.5 AD, ADD and RMS of the proposed algebraic solution, expressed in percent.

Combination	1	2	3	4	5	6	7	8	9
AD	-3.3	-0.1	25.3	-3.2	0.0	25.5	-1.6	1.7	27.8
AAD	5.5	4.4	25.3	5.4	4.4	25.5	5.2	5.3	27.8
RMS	5.5	5.6	6.5	5.6	5.6	6.6	6.3	6.4	7.6

As it can be seen from Tab. 4.5, the M&N friction factor presented poor results, regardless the k factor used, with AD bigger than 25%, being not recommended for this algebraic solution. Overall, the C- M&N friction factor performed better, with almost no difference between the k factors of Hermes et al. (2009) and Bhattacharyya et al. (2010) with the j factor. This result is in the same trend as that presented by Wang et al. (2012). According to them, the M&N modified friction factor is the most suitable for CO<sub>2</sub>. The Schmidt friction factor, despite being less complex, also presented a good agreement. As expected, most of the AD were negative, except when using M&N friction factor, since the HEM generally leads to an underestimated mass flow rate (ZHANG AND DING, 2004). The deviations of the predicted versus the experimental mass flow rates for all points, in combinations 1, 2, 4, 5, 7, and 8, can be seen in Figure 4.6.

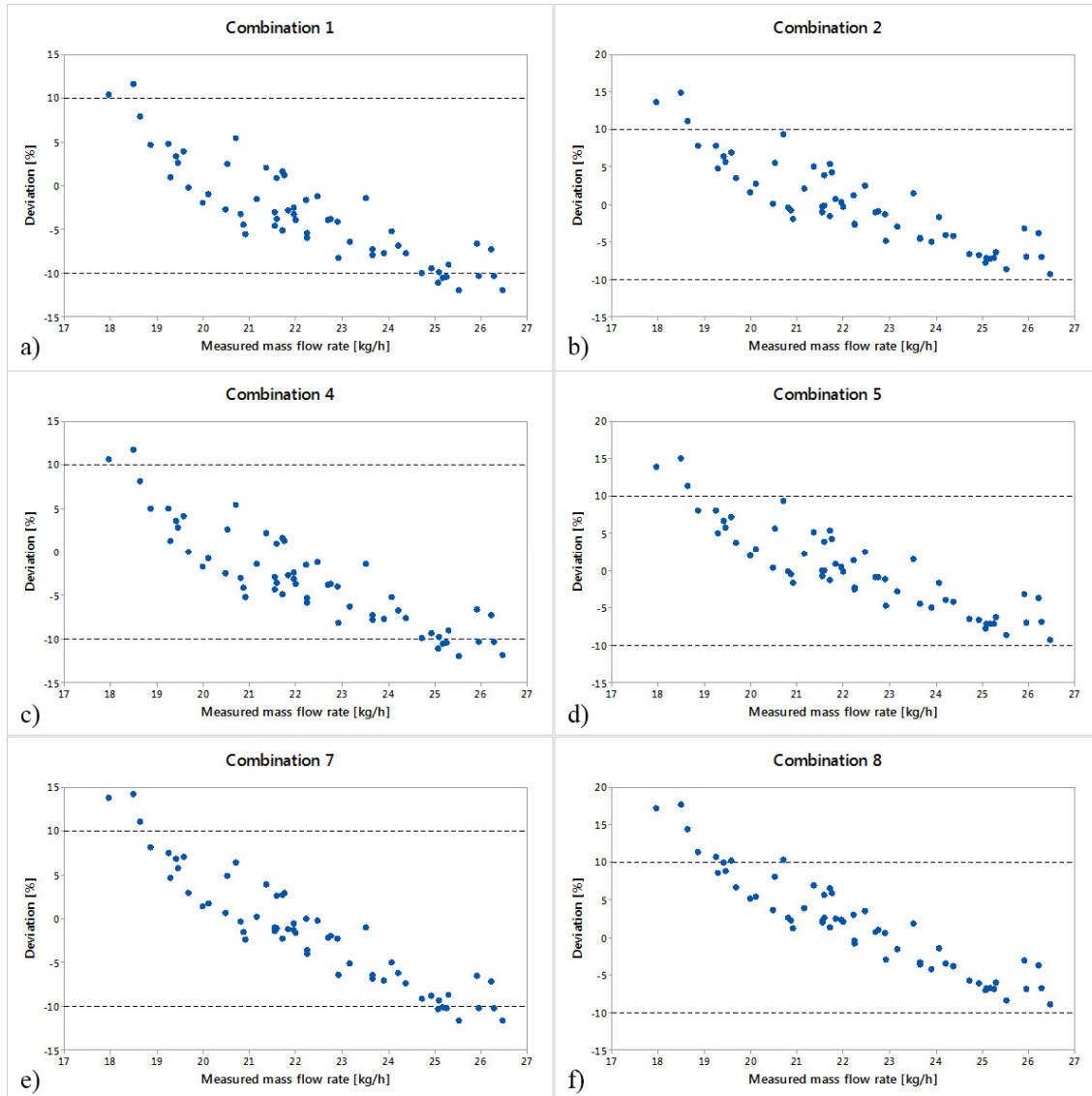


Figure 4.6: Deviations from predicted and measured mass flow rates for combination: a) 1; b) 2; c) 4; d) 5; e) 7; f) 8.

It is noticeable that there is a trend in sense of getting more negative deviations as the mass flow rate increases. According to Li et al. (1990), the larger the mass flow rate, the larger the under pressure of vaporization. Then, for higher mass flow rates, the metastability effect will be more prominent, justifying the trends in Figure 4.6. A little more detailed investigation also revealed that for capillary tube 1 ( $d = 1.07$  mm) the AD is bigger, or less negative than for capillary tube 4 ( $d = 0.911$  mm), as can be seen in Figure 4.7, for combination 1.

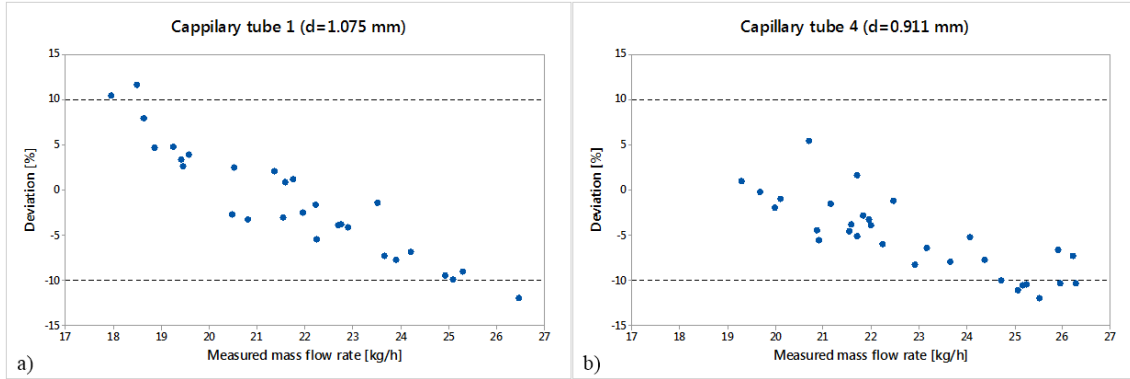


Figure 4.7: Deviations from predicted and measured mass flow for rate combination 1: a) capillary tube 1; b) capillary tube 4.

In this case, the AD for capillary tube 1 is -1.3%, while for capillary tube 4 is -5.2% (global average -3.3%). The other combinations, except for M&N friction factor, followed the same trend. This fact is also in agreement with the conclusions of Li et al. (1990). The percentage of data points within error bands of 10%, 12%, and 15% for all combinations is seen in Tab. 4.6.

Table 4.6 Percentual of data points within error bands of 10%, 12%, and 15%.

Error band	Combination								
	1	2	3	4	5	6	7	8	9
10%	85	95	0	85	95	0	83.3	88	0
12%	100	96.6	1.6	100	97	0	96.6	95	0
15%	100	100	3.3	100	98	3.3	100	97	1.6

As it can be seen, the proposed algebraic solution, using the C- M&N friction factor and Hermes et al. (2009) k factor, presented an agreement of 95% within a 10% error band, and 100% in a 15% error band. These metrics are in accordance with many numerical models, equations, and correlations for capillary tubes. For instance: the model of Da Silva et al. (2009) found 95% of data within a 10% error band for CO<sub>2</sub>. The equation of Hermes et al. (2010) predicted 89.1% of data within a 10% error band, for R600a and R134a. The correlation of Dubba and Kumar (2018b) found 98% of data within a 20% error band, for R600a. Therefore, it can be concluded that the proposed algebraic solution presented a good performance to study adiabatic coiled capillary tubes operating in transcritical CO<sub>2</sub> cycle.

## 5 CONCLUSIONS

In this work, the behavior of a CO<sub>2</sub> DX-SAHP, used to supply domestic hot water, and operating with a capillary tube was investigated. To design the capillary tube, an algebraic solution based on the homogeneous equilibrium model was developed. Then, the tube was assembled onto the workbench and tests were carried out according to a factorial design, with 2 different capillary tubes and 3 different operating conditions, namely: high solar radiation, low solar radiation, and low solar radiation with fan. Additional tests were also performed varying the CO<sub>2</sub> inventory and the use of the fan, to enlarge the experimental points to validate the algebraic solution. The comments drawn below are separated according to the following subjects: the heat pump response, and the adiabatic coiled capillary tube algebraic solution.

The results regarding the heat pump behavior indicated an average improvement of 57.9% and 42.3% on the heating capacity and on COP, respectively, when the solar radiation goes from 6 to 969 W/m<sup>2</sup>. In the same case, the mass flow rate raised 35%, the superheat degree went from 4.4 to 30.6 K, and the evaporating pressure changed from 40.0 to 51.2 bar. The gas cooler pressure also showed an increase, from 83.5 to 87.9 bar, being this variation more significative than that reported in other works. When changing from LSR to LSR+fan, an improvement of 17.2% on heating capacity was found, with no penalty to COP. Then, the addition of a fan demonstrated to be advantageous in low solar radiation conditions. The other variables showed the same trend as in LSR to HSR alteration. Regarding the possibility to use the capillary tube as the expansion device in a DX-SAHP, it was found that minor modifications need to be done to limit the raise of the superheat degree, assuring a safe operation to the compressor. There was no difference on the heat pump behavior when the capillary tube was changed, once they were sized to a same condition. Overall, the capillary tube demonstrated to be suitable for usage in a DX-SAHP.

The mass flow rates predicted by the algebraic solution, Eq. 3.42, were compared with the experimental data. For one of the possible combinations, the percentual of points predicted in a  $\pm 10\%$  and  $\pm 15\%$  error bands were 95% and 100%, respectively. The AD and the AAD were -0.1% and 4.4%, respectively. Overall, the C-M&N friction factor demonstrated to be the best for the proposed solution, but the Schmidt friction factor also presented a satisfactory level of performance. As expected for HEM, the AD was majority negative, being this effect more prominent for higher mass flow rates. Besides, the AD was more negative for the smallest capillary tube diameter.

The objectives proposed in this work were satisfactorily achieved, opening doors for possible cost reductions and making the DX-SAHP more attractive to be commercialized. Also, the proposed algebraic solution was found to be a good and less complex tool, compared to numerical models, for designing adiabatic coiled capillary tubes, operating in transcritical CO<sub>2</sub> cycle.

## 6 REFERENCES

- Adams, T., Grant, C., Watson, H., 2012. A Simple Algorithm to Relate Measured Surface Roughness to Equivalent Sand-grain Roughness. *Int. J. Mech. Eng. Mechatronics* 1. <https://doi.org/10.11159/ijmem.2012.008>
- Agrawal, N., Bhattacharyya, S., 2013. Study of helically coiled adiabatic capillary tubes for transcritical CO<sub>2</sub> expansion. *Int. J. Low-Carbon Technol.* 8, 245–252. <https://doi.org/10.1093/ijlct/cts047>
- Agrawal, N., Bhattacharyya, S., 2011. Experimental investigations on adiabatic capillary tube in a transcritical CO<sub>2</sub> heat pump system for simultaneous water cooling and heating. *Int. J. Refrig.* 34, 476–483. <https://doi.org/10.1016/j.ijrefrig.2010.09.014>
- Albertazzi, A., Sousa, A.R. de, 2008. *Fundamentos de Metrologia Científica e Industrial*, 1st ed. Manole.
- ASHRAE, 2013. *2013 ASHRAE Handbook - Fundamentals (SI Edition)*.
- ASME, 2013. *Refrigeration Piping and Heat Transfer Components: ASME Code for Pressure Piping, B31. THE AMERICAN SOCIETY OF MECHANICAL ENGINEERS.*
- Bengtsson, P., Berghel, J., 2016. Study of using a capillary tube in a heat pump dishwasher with transient heating. *Int. J. Refrig.* 67, 1–9. <https://doi.org/10.1016/j.ijrefrig.2016.04.006>
- Bhattacharyya, S., Agrawal, N., Burnwal, S., 2010. Flow rate prediction for an adiabatic capillary tube in a transcritical CO<sub>2</sub> system: An analytic approach. *Int. J. Low-Carbon Technol.* 5, 245–249. <https://doi.org/10.1093/ijlct/ctq030>
- Cecchinato, L., Corradi, M., 2011. Transcritical carbon dioxide small commercial cooling applications analysis. *Int. J. Refrig.* 34, 50–62. <https://doi.org/10.1016/j.ijrefrig.2010.09.019>
- Cecchinato, L., Corradi, M., Fornasieri, E., Schiochet, G., Zilio, C., 2009. Assessment on the use of common correlations to predict the mass-flow rate of carbon dioxide through capillary tubes in transcritical cycles. *Int. J. Refrig.* 32, 1041–1048.



<https://doi.org/10.1016/j.ijrefrig.2008.10.003>

- Cecchinato, L., Corradi, M., Minetto, S., 2010. A critical approach to the determination of optimal heat rejection pressure in transcritical systems. *Appl. Therm. Eng.* 30, 1812–1823. <https://doi.org/10.1016/j.applthermaleng.2010.04.015>
- Chen, Y., Gu, J., 2005. The optimum high pressure for CO<sub>2</sub> transcritical refrigeration systems with internal heat exchangers. *Int. J. Refrig.* 28, 1238–1249. <https://doi.org/10.1016/j.ijrefrig.2005.08.009>
- Chingulpitak, S., Wongwises, S., 2010. Two-phase flow model of refrigerants flowing through helically coiled capillary tubes. *Appl. Therm. Eng.* 30, 1927–1936. <https://doi.org/10.1016/j.applthermaleng.2010.04.026>
- Churchill, S.W., 1977. Friction-factor equation spans all fluid-flow regimes. *Chem. Eng. (New York)* 84, 91–92.
- da Silva, D.L., Hermes, C.J.L., Melo, C., Gonçalves, J.M., Weber, G.C., 2009. A study of transcritical carbon dioxide flow through adiabatic capillary tubes. *Int. J. Refrig.* 32, 978–987. <https://doi.org/10.1016/j.ijrefrig.2008.10.010>
- Danfoss, 2008. *Transcritical Refrigeration Systems with Carbon Dioxide (CO<sub>2</sub>): How to design and operate a small-capacity (< 10 kW) transcritical CO<sub>2</sub> system.*
- de Faria, R.N., 2013. Projeto e construção de uma bomba de calor a CO<sub>2</sub> operando em ciclo transcítico e modelagem dinâmica do conjunto evaporador solar-válvula de expansão. PhD Thesis.
- de Oliveira, R.N., 2013. Modelo dinâmico e estudo experimental para um resfriador de uma bomba de calor operando com CO<sub>2</sub> para aquecimento de água residencial. PhD Thesis.
- Del Col, D., Bisetto, A., Bortolato, M., Torresin, D., Rossetto, L., 2013. Experiments and updated model for two phase frictional pressure drop inside minichannels. *Int. J. Heat Mass Transf.* 67, 326–337. <https://doi.org/10.1016/j.ijheatmasstransfer.2013.07.093>
- Deodhar, S.D., Kothadia, H.B., Iyer, K.N., Prabhu, S. V., 2015. Experimental and numerical

- studies of choked flow through adiabatic and diabatic capillary tubes. *Appl. Therm. Eng.* 90, 879–894. <https://doi.org/10.1016/j.applthermaleng.2015.07.073>
- DUARTE, W.M., 2018. Numeric model of a direct expansion solar assisted heat pump water heater operating with low gwp refrigerants (R1234yf, R600a and R744) for replacement of R134a. PhD Thesis.
- Duarte, W.M., Paulino, T.F., Pabon, J.J.G., Sawalha, S., Machado, L., 2019. Refrigerants selection for a direct expansion solar assisted heat pump for domestic hot water. *Sol. Energy* 184, 527–538. <https://doi.org/10.1016/j.solener.2019.04.027>
- Dubba, S.K., Kumar, R., 2018a. Experimental investigation on flow of R-600a inside a diabatic helically coiled capillary tube: Concentric configuration. *Int. J. Refrig.* 86, 186–195. <https://doi.org/10.1016/j.ijrefrig.2017.10.035>
- Dubba, S.K., Kumar, R., 2018b. Adiabatic flow characteristics of R-600a inside a helically coiled capillary tube. *Appl. Therm. Eng.* 132, 500–507. <https://doi.org/10.1016/j.applthermaleng.2017.12.116>
- EHPA, 2019a. Large scale heat pumps in Europe: 16 examples of realized and successful projects. *Eur. Heat Pump Assoc.*
- EHPA, 2019b. Large scale heat pumps in Europe: Real examples of heat pump applications in several industrial sectors. *Eur. Heat Pump Assoc.*
- Fan, C., Yan, G., Yu, J., 2019. Thermodynamic analysis of a modified solar assisted ejector-compression heat pump cycle with zeotropic mixture R290/R600a. *Appl. Therm. Eng.* 150, 42–49. <https://doi.org/10.1016/j.applthermaleng.2019.01.011>
- Farshad, F., Rieke, H., Garber, J., 2001. New developments in surface roughness measurements, characterization, and modeling fluid flow in pipe. *J. Pet. Sci. Eng.* 29, 139–150. [https://doi.org/10.1016/S0920-4105\(01\)00096-1](https://doi.org/10.1016/S0920-4105(01)00096-1)
- Gill, J., Singh, J., 2018. Use of artificial neural network approach for depicting mass flow rate of R134a /LPG refrigerant through straight and helical coiled adiabatic capillary tubes of vapor compression refrigeration system. *Int. J. Refrig.* 86, 228–238.

<https://doi.org/10.1016/j.ijrefrig.2017.11.001>

Hadorn, J.C., 2012. IEA solar and heat pump systems Solar heating and cooling Task 44 & heat pump programme Annex 38. *Energy Procedia* 30, 125–133.

<https://doi.org/10.1016/j.egypro.2012.11.016>

Hermes, C.J.L., da Silva, D.L., Melo, C., Gonçalves, J.M., Weber, G.C., 2009. Algebraic solution of transcritical carbon dioxide flow through adiabatic capillary tubes. *Int. J. Refrig.* 32, 973–977. <https://doi.org/10.1016/j.ijrefrig.2008.10.006>

Hermes, C.J.L., Melo, C., Knabben, F.T., 2010. Algebraic solution of capillary tube flows. Part I: Adiabatic capillary tubes. *Appl. Therm. Eng.* 30, 449–457.

<https://doi.org/10.1016/j.applthermaleng.2009.10.005>

Hrnjak, P., Tu, X., 2007. Single phase pressure drop in microchannels. *Int. J. Heat Fluid Flow* 28, 2–14. <https://doi.org/10.1016/j.ijheatfluidflow.2006.05.005>

Huang, W., Zhang, T., Ji, J., Xu, N., 2019. Numerical study and experimental validation of a direct-expansion solar-assisted heat pump for space heating under frosting conditions. *Energy Build.* 185, 224–238. <https://doi.org/10.1016/j.enbuild.2018.12.033>

IEA, 2013 *Transitions to Sustainable Buildings: Strategies and Opportunities to 2050*. International Energy Agency.

INMET, 2019. National Institute of Meteorology: Automatic Station - Pampulha. Available on: <[http://www.inmet.gov.br/sonabra/pg\\_dspDadosCodigo\\_sim.php?QTUyMQ==](http://www.inmet.gov.br/sonabra/pg_dspDadosCodigo_sim.php?QTUyMQ==)> Visited on: Dec. 20, 2019.

IRENA, 2019. *Global energy transformation: A roadmap to 2050*. International Renewable Energy Agency.

Jadhav, P., Agrawal, N., 2019. A comparative study in the straight and a spiral adiabatic capillary tube. *Int. J. Ambient Energy* 40, 693–698.

<https://doi.org/10.1080/01430750.2017.1422146>

JCGM, 2008. *Evaluation of measurement data — Guide to the expression of uncertainty in*

- measurement. Int. Organ. Stand. Geneva ISBN 50, 134.  
<https://doi.org/10.1373/clinchem.2003.030528>
- Johra, H., Filonenko, K., Heiselberg, P., Veje, C., Dall'Olio, S., Engelbrecht, K., Bahl, C., 2019. Integration of a magnetocaloric heat pump in an energy flexible residential building. *Renew. Energy* 136, 115–126. <https://doi.org/10.1016/j.renene.2018.12.102>
- Kauf, F., 1999. Determination of the optimum high pressure for transcritical CO<sub>2</sub>-refrigeration cycles. *Int. J. Therm. Sci.* 38, 325–330. [https://doi.org/10.1016/S1290-0729\(99\)80098-2](https://doi.org/10.1016/S1290-0729(99)80098-2)
- Kong, X., Sun, P., Dong, S., Jiang, K., Li, Y., 2018. Experimental performance analysis of a direct-expansion solar-assisted heat pump water heater with R134a in summer. *Int. J. Refrig.* 91, 12–19. <https://doi.org/10.1016/j.ijrefrig.2018.04.021>
- Lee, S.J., Shon, B.H., Jung, C.W., Kang, Y.T., 2018. A novel type solar assisted heat pump using a low GWP refrigerant (R-1233zd(E)) with the flexible solar collector. *Energy* 149, 386–396. <https://doi.org/10.1016/j.energy.2018.02.018>
- Liao, S.M., Zhao, T.S., Jakobsen, A., 2000. Correlation of optimal heat rejection pressures in transcritical carbon dioxide cycles. *Appl. Therm. Eng.* 20, 831–841.  
[https://doi.org/10.1016/S1359-4311\(99\)00070-8](https://doi.org/10.1016/S1359-4311(99)00070-8)
- Lorentzen, G., 1994. Revival of carbon dioxide as a refrigerant. *Int. J. Refrig.* 17, 292–301.  
[https://doi.org/10.1016/0140-7007\(94\)90059-0](https://doi.org/10.1016/0140-7007(94)90059-0)
- Lu, S., Liang, R., Zhang, J., Zhou, C., 2019. Performance improvement of solar photovoltaic/thermal heat pump system in winter by employing vapor injection cycle. *Appl. Therm. Eng.* 155, 135–146. <https://doi.org/10.1016/j.applthermaleng.2019.03.038>
- Madsen, K.B., Poulsen, C.S., Wiesenfarth, M., 2005. Study of capillary tubes in a transcritical CO<sub>2</sub> refrigeration system. *Int. J. Refrig.* 28, 1212–1218.  
<https://doi.org/10.1016/j.ijrefrig.2005.09.009>
- Melo, C., Ferreira, R.T.S., Neto, C.B., Gonçalves, J.M., Mezavila, M.M., 1999. Experimental analysis of adiabatic capillary tubes. *Appl. Therm. Eng.* 19, 669–684.

[https://doi.org/10.1016/S1359-4311\(98\)00062-3](https://doi.org/10.1016/S1359-4311(98)00062-3)

Mohamed, E., Riffat, S., Omer, S., Zeinelabdien, R., 2019. A comprehensive investigation of using mutual air and water heating in multi-functional DX-SAMHP for moderate cold climate. *Renew. Energy* 130, 582–600. <https://doi.org/10.1016/j.renene.2018.06.075>

Montgomery, D.C., 2013. *Design and Analysis of Experiments*, 8th ed. John Wiley & Sons.

Mori, Y., Nakayama, W., 1967. Study of forced convective heat transfer in curved pipes (2nd report, turbulent region). *Int. J. Heat Mass Transf.* 10, 37–59.  
[https://doi.org/10.1016/0017-9310\(67\)90182-2](https://doi.org/10.1016/0017-9310(67)90182-2)

Nikuradse, J., 1950. Laws of Flow in Rough Pipes. *J. Appl. Phys.* 3, 399.  
<https://doi.org/10.1063/1.1715007>

Paulino, T. de F., 2019. Experimental and theoretical study of the dynamic response of a small size CO<sub>2</sub> direct expansion solar assisted heat pump. PhD Thesis.

Paulino, T. de F., de Oliveira, R.N., Maia, A.A.T., Palm, B., Machado, L., 2019. Modeling and experimental analysis of the solar radiation in a CO<sub>2</sub> direct-expansion solar-assisted heat pump. *Appl. Therm. Eng.* 148, 160–172.  
<https://doi.org/10.1016/j.applthermaleng.2018.11.045>

Poppi, S., Sommerfeldt, N., Bales, C., Madani, H., Lundqvist, P., 2018. Techno-economic review of solar heat pump systems for residential heating applications. *Renew. Sustain. Energy Rev.* 81, 22–32. <https://doi.org/10.1016/j.rser.2017.07.041>

Prajapati, Y., Khan, M.K., Pathak, M., 2014. Two-Phase VOF model for the refrigerant flow through adiabatic capillary tube, in: *ASHRAE Transactions*. pp. 60–67.

Qi, P.C., He, Y.L., Wang, X.L., Meng, X.Z., 2013. Experimental investigation of the optimal heat rejection pressure for a transcritical CO<sub>2</sub> heat pump water heater. *Appl. Therm. Eng.* 56, 120–125. <https://doi.org/10.1016/j.applthermaleng.2013.03.045>

Rabelo, S.N., Paulino, T.F., Duarte, W.M., Maia, A.A.T., Machado, L., 2019. Experimental analysis of the influence of the expansion valve opening on the performance of the small

- size CO<sub>2</sub> solar assisted heat pump. *Sol. Energy* 190, 255–263.  
<https://doi.org/10.1016/j.solener.2019.08.013>
- Rasti, M., Jeong, J.H., 2018. A generalized continuous empirical correlation for predicting refrigerant mass flow rates through adiabatic capillary tubes. *Appl. Therm. Eng.* 139, 47–60. <https://doi.org/10.1016/j.applthermaleng.2018.04.111>
- Rocha, T.T.M., Campos, F., Schettino Faria, V., de Freitas Paulino, T., Nunes, R., 2019. Assessment of Different Methods for Predicting the Mass Flow Rate Through Adiabatic Capillary Tubes, in: 25th International Congress of Mechanical Engineering - COBEM 2019. <https://doi.org/10.26678/abcm.cobem2019.cob2019-0783>
- Ruas, S.N.R., 2019. Estudo experimental sobre o desempenho de uma bomba de calor a CO<sub>2</sub> assistida por energia solar de expansão direta para aquecimento de água para uso residencial. PhD Thesis.
- Rui-Yang Li, Sui Lin, Zu-Yao Chen, Zhi-Hang Chen, 1990. Metastable flow of R12 through capillary tubes. *Int. J. Refrig.* 13, 181–186. [https://doi.org/10.1016/0140-7007\(90\)90073-6](https://doi.org/10.1016/0140-7007(90)90073-6)
- Schenk, M., Oellrich, L.R., 2014. Experimental investigation of the refrigerant flow of isobutane (R600a) through adiabatic capillary tubes. *Int. J. Refrig.* 38, 275–280.  
<https://doi.org/10.1016/j.ijrefrig.2013.08.024>
- Shi, G.H., Aye, L., Dai, R., Du, X.J., Wang, J.J., 2019a. Dynamic modelling and performance evaluation of a direct-expansion solar-assisted heat pump for LPG vaporisation applications. *Appl. Therm. Eng.* 149, 757–771.  
<https://doi.org/10.1016/j.applthermaleng.2018.12.101>
- Shi, G.H., Aye, L., Li, D., Du, X.J., 2019b. Recent advances in direct expansion solar assisted heat pump systems: A review. *Renew. Sustain. Energy Rev.* 109, 349–366.  
<https://doi.org/10.1016/j.rser.2019.04.044>
- Song, Y., Wang, J., Cao, F., Shu, P., Wang, X., 2017. Investigation on the adaptivity of the transcritical CO<sub>2</sub> refrigeration system with a capillary. *Int. J. Refrig.* 79, 183–195.  
<https://doi.org/10.1016/j.ijrefrig.2017.04.013>

- Taylor, J.B., Carrano, A.L., Kandlikar, S.G., 2006. Characterization of the effect of surface roughness and texture on fluid flow-past, present, and future. *Int. J. Therm. Sci.* 45, 962–968. <https://doi.org/10.1016/j.ijthermalsci.2006.01.004>
- Vinš, V., Vacek, V., 2009. Mass flow rate correlation for two-phase flow of R218 through a capillary tube. *Appl. Therm. Eng.* 29, 2816–2823. <https://doi.org/10.1016/j.applthermaleng.2009.02.001>
- Wang, D., Lu, Y., Tao, L., 2018. Optimal combination of capillary tube geometry and refrigerant charge on a small CO<sub>2</sub> water-source heat pump water heater. *Int. J. Refrig.* 88, 626–636. <https://doi.org/10.1016/j.ijrefrig.2018.03.009>
- Wang, J., Cao, F., Wang, Z., Zhao, Y., Li, L., 2012. Numerical simulation of coiled adiabatic capillary tubes in CO<sub>2</sub> transcritical systems with separated flow model including metastable flow. *Int. J. Refrig.* 35, 2188–2198. <https://doi.org/10.1016/j.ijrefrig.2012.07.012>
- Wang, X., Xia, L., Bales, C., Zhang, X., Copertaro, B., Pan, S., Wu, J., 2020b. A systematic review of recent air source heat pump (ASHP) systems assisted by solar thermal, photovoltaic and photovoltaic/thermal sources. *Renew. Energy* 146, 2472–2487. <https://doi.org/10.1016/j.renene.2019.08.096>
- Wang, Z., Wang, F., Li, G., Song, M., Ma, Z., Ren, H., Li, K., 2020a. Experimental investigation on thermal characteristics of transcritical CO<sub>2</sub> heat pump unit combined with thermal energy storage for residential heating. *Appl. Therm. Eng.* 165, 114505. <https://doi.org/10.1016/j.applthermaleng.2019.114505>
- Yang, L., Li, H., Cai, S.W., Shao, L.L., Zhang, C.L., 2015. Minimizing COP loss from optimal high pressure correlation for transcritical CO<sub>2</sub> cycle. *Appl. Therm. Eng.* 89, 656–662. <https://doi.org/10.1016/j.applthermaleng.2015.06.023>
- Yang, L., Wang, W., 2008. A generalized correlation for the characteristics of adiabatic capillary tubes. *Int. J. Refrig.* 31, 197–203. <https://doi.org/10.1016/j.ijrefrig.2007.06.012>
- Yang, L., Zhang, C.L., 2014. A generalized dimensionless local power-law correlation for refrigerant flow through adiabatic capillary tubes and short tube orifices. *Int. J. Refrig.*

- 46, 69–76. <https://doi.org/10.1016/j.ijrefrig.2014.06.011>
- Yang, L., Zhang, C.L., 2009. Modified neural network correlation of refrigerant mass flow rates through adiabatic capillary and short tubes: Extension to CO<sub>2</sub> transcritical flow. *Int. J. Refrig.* 32, 1293–1301. <https://doi.org/10.1016/j.ijrefrig.2009.03.005>
- Yilmaz, T., Ünal, S., 1996. General equation for the design of capillary tubes. *J. Fluids Eng. Trans. ASME* 118, 150–154. <https://doi.org/10.1115/1.2817493>
- Young, P.L., Brackbill, T.P., Kandlikar, S.G., 2009. Comparison of roughness parameters for various microchannel surfaces in single-phase flow applications. *Heat Transf. Eng.* 30, 78–90. <https://doi.org/10.1080/01457630802293464>
- Zareh, M., Shokouhmand, H., Salimpour, M.R., Taeibi, M., 2014. Numerical simulation and experimental analysis of refrigerants flow through adiabatic helical capillary tube. *Int. J. Refrig.* 38, 299–309. <https://doi.org/10.1016/j.ijrefrig.2013.07.028>
- Zhang, C., Ding, G., 2004. Approximate analytic solution of adiabatic capillary tube. *Int. J. Refrig.* 27, 17–24. [https://doi.org/10.1016/S0140-7007\(03\)00117-8](https://doi.org/10.1016/S0140-7007(03)00117-8)
- Zhao, D., Ding, G., Xu, Y., Zou, S., 2014. Development of a stepped capillary tube as a low cost throttling device for a residential heat pump system. *Int. J. Refrig.* 42, 36–47. <https://doi.org/10.1016/j.ijrefrig.2014.02.011>
- Zhou, G., Yao, S.C., 2011. Effect of surface roughness on laminar liquid flow in micro-channels. *Appl. Therm. Eng.* 31, 228–234. <https://doi.org/10.1016/j.applthermaleng.2010.09.002>
- Zhou, G., Zhang, Y., 2006. Numerical and experimental investigations on the performance of coiled adiabatic capillary tubes. *Appl. Therm. Eng.* 26, 1106–1114. <https://doi.org/10.1016/j.applthermaleng.2005.11.003>
- Zhou, J., Zhao, X., Yuan, Y., Li, J., Yu, M., Fan, Y., 2020. Operational performance of a novel heat pump coupled with mini-channel PV/T and thermal panel in low solar radiation. *Energy Built Environ.* 1, 50–59. <https://doi.org/10.1016/j.enbenv.2019.08.001>



## APPENDIX A – GEOMETRIC CHARACTERIZATION OF THE CAPILLARY TUBES

Two types of samples were prepared: one for inner diameter measurement (D), with approximately 10 mm length, and other for internal surface roughness measurement (R), with approximately 50 mm length. An identification code composed by 3 digits was adopted, according to Tab. A.1. The position and quantity of samples prepared for each tube is seen in Fig. A.1.

Table A.1: Code for sample identification.

First digit	Second digit	Third digit
Capillary tube roll	Type of measurement	replicate
1, 2, 3, 4, 5	D, R	1, 2

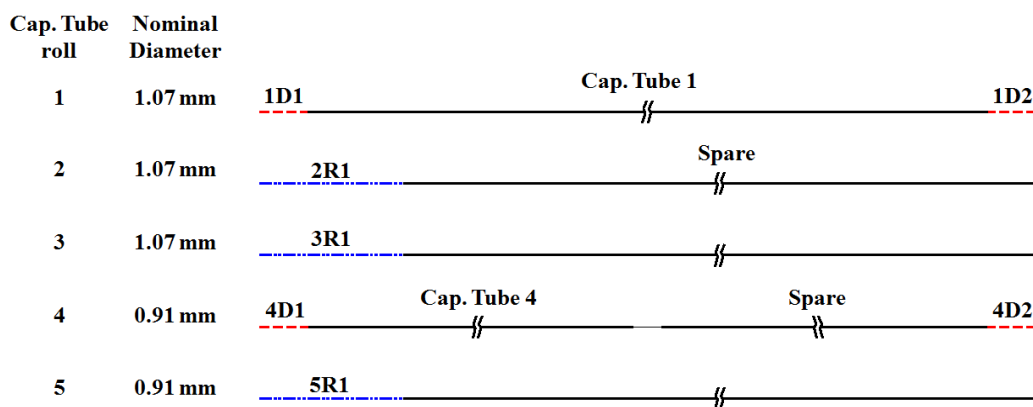


Figure A.1: Schematic representation of the samples cut from capillary tube rolls.

### A.1 Inner diameter measurements

The measurement results for the samples of capillary tubes 1 and 4 are seen in Tables A.2 and A.3 respectively. The final averages for the capillary tubes are seen in Table A.4.

Table A.2: Inner diameter measurements of samples 1D1 and 1D2.

Position [°]	CAPILLARY TUBE 1 - Sample 1D1					CAPILLARY TUBE 1 - Sample 1D2			
	0	90	45	225	random	0	90	45	225
Measure [mm]	1.086	1.079	1.074	1.071	1.074	1.072	1.072	1.073	1.077
	1.078	1.085	1.071	1.070	1.080	1.076	1.076	1.073	1.074
	1.084	1.084	1.067	1.073	1.079	1.068	1.073	1.078	1.078
	1.080	1.076	1.066	1.070	1.078	1.062	1.069	1.078	1.076
	1.082	1.083	1.070	1.076	1.075	1.075	1.074	1.076	1.077
Position average [mm]	1.082	1.081	1.070	1.072	1.077	1.071	1.073	1.076	1.076
Sample average [mm]	1.076				1.074				
u' [mm]	0.006				0.004				

Table A.3: Inner diameter measurements of samples 4D1 and 4D2.

Position [°]	CAPILLARY TUBE 4 - Sample 4D1				CAPILLARY TUBE 4 - Sample 4D2			
	0	90	45	225	0	90	45	225
Measure [mm]	0.911	0.924	0.916	0.907	0.910	0.896	0.909	0.910
	0.907	0.915	0.926	0.914	0.916	0.890	0.908	0.910
	0.909	0.915	0.919	0.911	0.916	0.908	0.907	0.906
	0.908	0.916	0.917	0.926	0.915	0.905	0.906	0.909
	0.905	0.919	0.921	0.916	0.920	0.901	0.903	0.900
Position average [mm]	0.908	0.918	0.920	0.915	0.915	0.900	0.907	0.907
Sample average [mm]	0.915				0.907			
u' [mm]	0.006				0.007			

Table A.4: Inner diameter final measures.

Capillary tube	d [mm]	U [mm]	k95	v
1	1.075	0.011	2.064	44
4	0.911	0.016	2.066	39

## A.2 Internal surface roughness measurement

The internal surface measurements by stylus profilometry are seen in Tab. A.5, together with the respective standard deviations. The uncertainty due to the equipment resolution was considered in the uncertainty balance. However, it was not significant and could be neglected without altering the result. The samples 2R1 and 3R1 have the same specification and were analyzed together.

Table A.5: Roughness parameters values for samples 2R1, 3R1, and 5R1, in Stylus measurement.

Measure	Ra			Rq			Rp			Rz		
	2R1	3R1	5R1	2R1	3R1	5R1	2R1	3R1	5R1	2R1	3R1	5R1
1 [ $\mu\text{m}$ ]	0.600	0.616	0.805	0.740	0.804	0.991	1.950	2.200	2,230	4,240	3,680	4,980
2 [ $\mu\text{m}$ ]	0.682	0.869	0.808	0.826	1.010	0.994	1.930	2.420	2,200	4,210	4,130	4,970
3 [ $\mu\text{m}$ ]	0.622	0.690	0.776	0.759	0.974	1.000	1.970	3.000	2,490	4,240	4,450	4,770
Average [ $\mu\text{m}$ ]	0.680	0.796	0.852	0.995	2.245	2.307	4.158	4.907				
u' [ $\mu\text{m}$ ]	0.100	0.018	0.113	0.005	0.416	0.159	0.257	0.118				
v	5	2	5	2	5	2	5	2				
k95	2.649	4.527	2.649	4.527	2.649	4.527	2.649	4.527	2.649	4.527	2.649	4.527
U [ $\mu\text{m}$ ]	0.264	0.080	0.300	0.021	1.102	0.722	0.681	0.536				

The measurements by optical profilometry are seen in Tab. A.6, together with the respective standard deviations.

Table A.6: Roughness parameters values for samples 2R1, 3R1, and 5R1, in Optical measurement.

Measure	Ra			Rq			Rz		
	2R1	3R1	5R1	2R1	3R1	5R1	2R1	3R1	5R1
1 [ $\mu\text{m}$ ]	0.258	0.320	0.276	0.344	0.476	0.366	3.409	6.443	3.167
2 [ $\mu\text{m}$ ]	0.277	0.295	0.324	0.360	0.378	0.427	4.026	3.310	4.085
3 [ $\mu\text{m}$ ]	0.260	0.273	0.281	0.357	0.353	0.370	3.426	3.009	3.736
4 [ $\mu\text{m}$ ]	0.258			0.393			5.697		
Average [ $\mu\text{m}$ ]	0.277	0.294	0.380	0.388	4.189	3.663			
u' [ $\mu\text{m}$ ]	0.023	0.026	0.045	0.034	1.338	0.463			
v	6	2	6	2	6	2			
k95	2.517	4.527	2.517	4.527	2.517	4.527	2.517	4.527	
U [ $\mu\text{m}$ ]	0.058	0.119	0.114	0.154	3.367	2.098			

Comparing Tables A.5 and A.6, some comments can be made. Firstly, the optical profilometry software did not provide the Rp parameter. Secondly, the Ra and Rq values presented a large difference between the two techniques. Only the Rz parameter was consistent in both measurements. However, the U (Rz) presented by the optical profilometry was almost 85% for samples 2R1 and 3R1, and 57% for sample 5R1. Theoretically, the optical profilometry should present a more accurate result, once the stylus profilometry has a finite tip radius, which makes difficult to reach some valleys.

Since the capillary tubes 1, 2 and 3 are of same specification, the roughness value for the samples 2 and 3 were considered for the capillary tube 1. In a similar way, the roughness of tube 5 was considered for tube 4. The values provided by stylus profilometry were considered.

### A.3 Length measurements

For capillary tubes 4 and 4 spare both procedures, described in section X, were adopted and the results were compared. The larger the line diameter, the larger the tube length uncertainty. Then, a nylon line with diameter of 0.74 mm was used in capillary tube 4. For tube 4 Spare, despite the same characteristics of tube 4, that line did not work. So, a thinner line, with diameter of 0.4 mm was used, leading to a larger length uncertainty. A calibrated tape measure, certificate number 648/19 issued by Senai, manufactured by Fender, with 5 meters length, was used in the line measurements. For capillary tubes 1 and 2, procedure 1 did not work with any line diameter, therefore, procedure 2 was used.

The uncertainty balance for procedure 1 is seen in Tab.A.7, while the average coil diameter and the respective standard deviation for procedure 2 is seen in Table. A.8.

Table A.7: Uncertainty balance for tubes C and D, measured by procedure 1.

CAP. TUBE	DESCRIPTION	SYSTEMATIC EFFECTS		RANDOM EFFECTS			
		Td	raw value	distribution	k95	u'	v
4 (Spare)	Measure	0	2	rectangular	1.73	1.2	$\infty$
	Tape measure calibration	-0.6	0.3	normal	2.23	0.1	10
	Difference in line diameter and inner diameter	0	5.1	rectangular	1.73	2.9	$\infty$
	Combined Td, u e v	-0.6			2.00	3.2	3.1E+06
	Expanded uncertainty					6.3	
	4	Measure	0	2	rectangular	1.73	1.2
	Tape measure calibration	-0.6	0.3	normal	2.23	0.1	10
	Difference in line diameter and inner diameter	0	1.7	rectangular	1.73	1.0	$\infty$
	Combined Td, u e v	-0.6			2.00	1.5	1.6E+05
	Expanded uncertainty					3.0	

Table A.8: Average coil diameter and standard deviation for procedure 2.

Cap. Tube	Average coil diameter [mm]	u' [mm]
1	120.33	0.40
2	126.65	0.41
4 (Spare)	133.16	0.33
4	133.97	0.17

The measurement results, with the associated uncertainties are seen in Tab. A.9.

Table A.9: Capillary tube lengths and associated uncertainties.

Procedure	Cap. Tube	L [mm]	U [mm]	k95	v
2	1	2973	$\pm 21$	2.11	25
2	2 (Spare)	2325	$\pm 16$	2.11	25
2	4 (Spare)	1339	$\pm 8$	2.32	9
2	4	1340	$\pm 5$	2.32	9
1	4 (Spare)	1340	$\pm 6$	2.00	3.1E+06
1	4	1338	$\pm 3$	2.00	1.6E+05

As can be seen in Table A.9, the results showed by procedure 1 and 2 for capillary tubes 4 and 4 Spare are consistent. Despite the larger uncertainty presented by procedure 2, the capillary tube lengths can be used safely.

#### A.4 Coil diameter measurement

A calibrated analog caliper, certified number 628/2019 issued by Senai, resolution of 0.05 mm, manufactured by Mitutoyo was used. The measurement result is seen in Tab. A.10, together with the respective uncertainties.

Table A.10: Capillary tube coil diameters and associated uncertainties.

Cap. Tube	D [mm]	U [mm]	k95	v
1	28.5	$\pm 1,0$	2.212	13
4	75.0	$\pm 0,5$	2.429	7

## APPENDIX B – VERIFICATION OF THE MEASUREMENT INSTRUMENTS

### B1. Verifications of the pressure meters

The pressure meter Zurich PHD.II, 0-150 bar, were verified using a pressure calibrator, hydraulic pump type, manufactured by Zurich, model 800.D, as seen in Figure B.1.



Figure B.1: Pressure calibrator used for verification.

Two different manometers, manufactured by Zurich, with the following specifications were used as reference: model Z-10B-A4, 0-10 bar, ID/3923/02/2015, with calibration of 2018; model Z-10B-A4, 0-300 bar, 05/2008. The pressure values displayed by the Zurich PHD.II meter versus the two reference meters can be seen in Figure B.2.

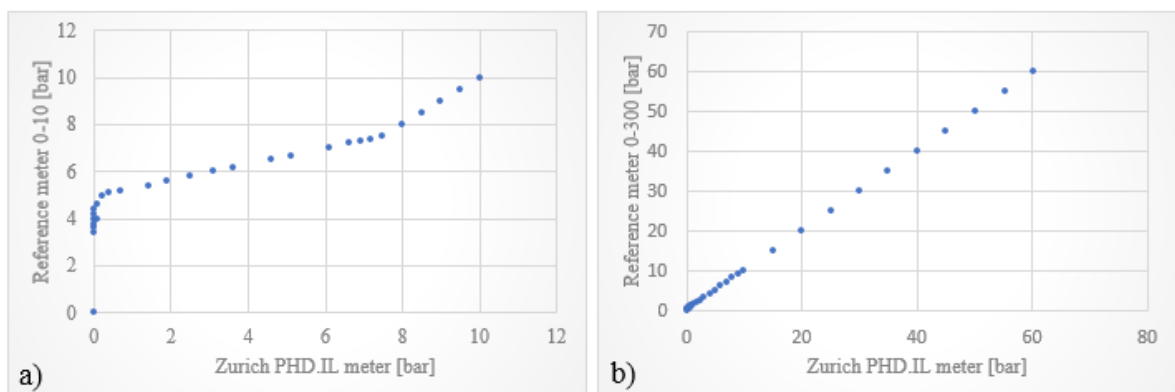


Figure B.2: Displayed values for the Zurich PHD.II meter and the reference meters: a) 0-10 bar meter; b) 0-300 bar meter.

For the 0-10 bar meter (Figure B.2a)), up to 7.5 bar, the displayed pressures were different, with a strong non-linearity near zero. From 7.5 bar on, both meters showed the same values.

Regarding the 0-300 bar meter (Figure 3.2b)), the behavior was completely linear, with maximum difference of 0.2 bar. Since in the range of 7.5 to 10 bar there was no difference compared to both reference meters, the 0-300 one was considered valid, even without a certificate of calibration.

Then, the PHD.IL meter was used as reference to obtain the response curves Voltage versus Pressure for the two Fueltech pressure transducers (P2 and P3) and for the Novus pressure transducer (P1). The pressure was gradually lowered, waiting the system to reach the equilibrium condition before taking a measurement of a point. Besides, all meters are in the same level, therefore, there is no pressure difference among them. The generated curves are valid for the set transducer/data acquisition board, and are seen in Figure B.3.

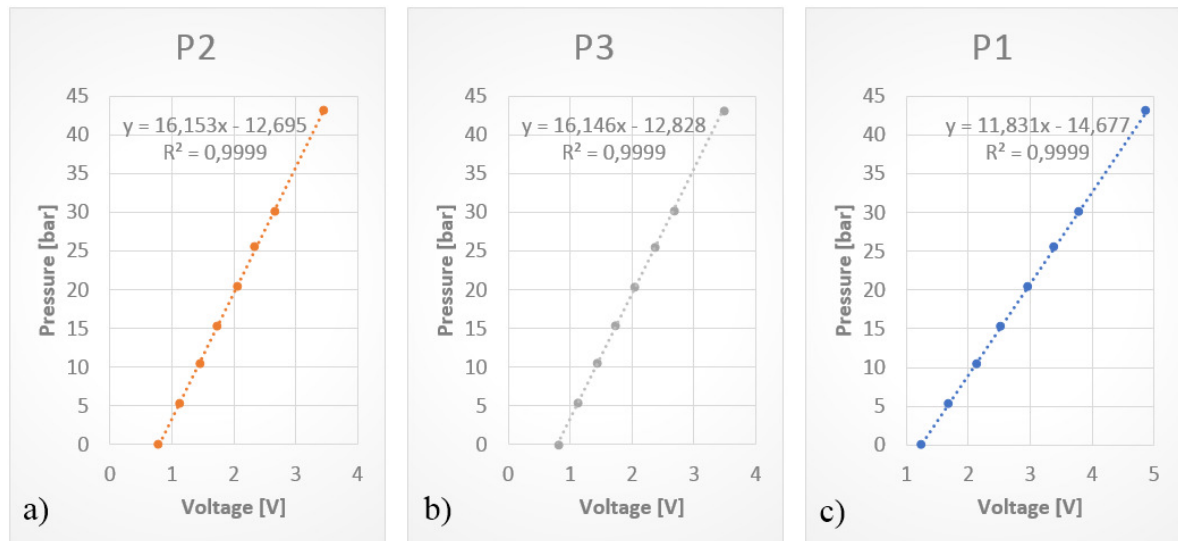


Figure B. 3: Voltage versus Pressure curves for the transducers: a) P2; b) P3; c) P1.

The three curves were fitted by a linear regression, and the equations found were implemented in the Labview interface program. The pressures P2 and P3 are supposed to operate in a range up to about 90 bar, and despite a maximum pressure of 43.1 bar used to obtain the curves, the R<sup>2</sup> equal to 0.999 indicates a good linearity of these sensors.

## B2. Verification of the wattmeter

The response curve Voltage vs Power was obtained using two light bulbs, with nominal power of 100 W each. To verify the actual power, an electrical energy meter with accuracy of 1% (Figure B.4), was used, while timing the measurement to give the power in Watts unit. The electrical power values and the associated uncertainties can be seen in Tab.B.1.



Figure B.4: Electrical energy meter.

Table B.1: Light bulbs power values and associated uncertainties.

Measure	1 light bulb [W]	2 light bulbs [W]
1 [W]	104.93	211.14
2 [W]	106.51	212.1
3 [W]	104.09	208.49
4 [W]	105.27	209.38
Average [W]	105.20	210.28
u'	1.00	1.64
v	3	3
K95	3.307	3.307
U [%]	3.16	2.58

Then, the average values in Tab. B.1 and the signal received by the acquisition board were fitted by a linear regression to give the response curve, as seen in Figure B.5. The final uncertainty for the electrical power measurement, including the uncertainties sources of the wattmeter, the electrical energy meter and the light bulbs was estimated in 5%.

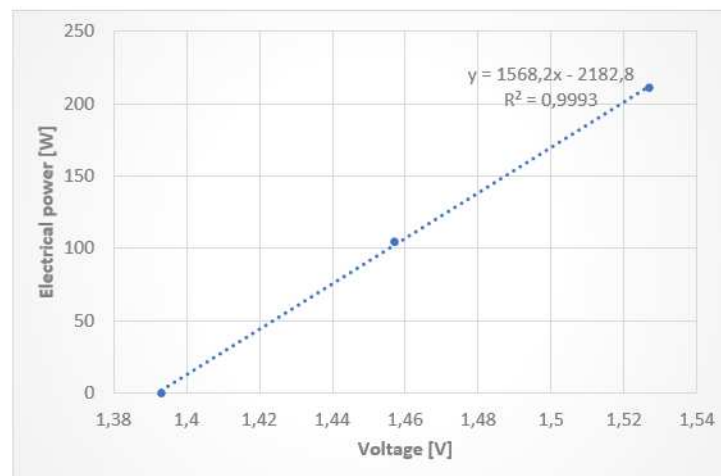


Figure B.5: Voltage versus Pressure curve for the Wattmeter.